ABSTRACT

Title: STUDY ON-CHIP METAL-INSULATOR-SEMICONDUCTOR-METAL INTERCONNECTS WITH THE ALTERNATING-DIRECTION-IMPLICIT FINITE-DIFFERENCE TIME-DOMAIN METHOD

Bo Yang
Master of Science, 2005

Directed By: Professor Neil Goldsman
Department of Electrical and Computer Engineering

The Alternating-Direction-Implicit Finite-Difference Time-Domain method is used to analyze the on-chip Metal-Insulator-Semiconductor-Metal interconnects by solving Maxwell's equations in time domain. This method is efficient in solving problems with fine geometries much smaller than the shortest wavelength of interest. The iteration algorithm is evaluated thoroughly with respects to stability, numerical dispersion, grid size, time-step size etc..

The dielectric quasi-TEM mode, the slow wave mode, and the skin-effect mode of the MISM structure are all analyzed. We find that semiconductors can readily operate from the slow wave mode, to the transition region, to the skin effect mode in state of art technology. This thesis shows that the silicon substrate losses and the metal line losses can be modeled with high resolution. Signal dispersion and attenuation over a wide range of doping densities and operating frequencies is

discussed. Accurate prediction of interconnect losses is critical for high-frequency design with highly constrained timing requirements.

STUDY ON-CHIP METAL-INSULATOR-SEMICONDUCTOR-METAL INTERCONNECTS WITH THE ALTERNATING-DIRECTION-IMPLICIT FINITE-DIFFERENCE TIME-DOMAIN METHOD

By

Bo Yang

Thesis submitted to the Faculty of the Graduate School of the
University of Maryland, College Park, in partial fulfillment
of the requirements for the degree of
Master of Science
2005

Advisory Committee:
Professor Neil Goldsman, Chair
Professor Martin C. Peckerar
Professor Omar M. Ramahi

Dedication

This work is to my family, for supporting my education over the years.

Acknowledgements

I would like to thank my academic advisor, Professor Neil Goldsman, for inviting me to be one of his graduate students. Without his encouragement and support, none of this work would have been possible.

In particular, I would like to thank Dr. Xi Shao. The valuable discussions with him initiated all of the ideas in this thesis. This thesis is an extension of his earlier work.

Discussions with Professor Omar M. Ramahi, Professor Martin C. Peckerar, and Dr. Parvez N. Guzdar provided great insight and inspired several ideas in this thesis.

I am very pleased that Professor Omar M. Ramahi and Professor Martin C. Peckerar agreed to serve on my committee.

I would also like to thank Akin Akturk, Amrit Bandyopadhyay, Siddharth V. Potbhare, and Zeynep Dilli for helpful discussions and comments through this project.

Finally, I would like to thank Latise Parker for editorial comments and language refinement of this thesis.

Table of Contents

List of Figures

Chapter 1: Introduction

1.1 Background

In modern integrated circuit (IC) designs, circuit elements continue to shrink in size while operating frequencies continue to increase. Main processor chips can be as large as 2cm×2cm in size with tens of millions of transistors. Digital clock rates are reaching 4 GHz and are predicted to continue increasing in the near future by the National Technology Roadmap for Semiconductors. Seven wiring layers have been fabricated with 0.3 μm minimum widths [1]. The small cross section of the metal interconnects will introduce line resistances as high as 1000-3000 Ω/cm, even for copper wires that have higher conductivity than aluminum wires. Global interconnections such as clock lines, data buses (32-128 bits wide), and control lines are of the order of 20-50K nets on one chip, and it will reach more than 100K connections in the future [1].

In the high-frequency range, propagation delay (This is the signal traveling time.) is comparable to signal transition times (This is the signal rising and falling time.), and wire length is comparable to wavelength of the signal. Parasitic circuit parameters will directly impact power loss and signal integrity of the circuit as well as degrade the performance of the circuit. Since interconnects play an important role in transporting power and data in the circuit, accurately determining the parasitic circuit parameters and predicting their effect is important in radio frequency (RF) and microwave integrated circuits (IC's) as well as digital IC's.

Extensive experimental, analytical and numerical research in analyzing the characteristics of interconnects began in the late 1960's and include various investigations ranging from off-chip PCB interconnections to on-chip interconnects [2]-[8]. The consensus is on-chip interconnects are faster, denser and more reliable than off-chip ones. These are important factors in the trend of higher integration levels in the IC industry. Thus, this work will focus particularly on on-chip interconnects. Also, the numerical simulation method used in this work is investigated in detail in Chapter three.

In 1967, Guckel analyzed interconnections using a parallel-plate waveguide structure with a two-layer (Si-SiO_2) loading medium while ignoring fringing fields [2]. His work shows at the lowest-frequency interval, the majority current perpendicular to the propagation direction is conduction current, not displacement current. This means propagation resembles diffusion (conductive loss) because of loss in the dielectric layer. In the next frequency range, the phase velocity of the fundamental mode is controlled by the ratio of dielectric to semiconductor thickness. The velocity is very low for a typical interconnection. On the one hand, people can use this characteristic to design the delay line; on the other hand, people are making efforts to reduce the unwanted signal delay as much as possible. In the highest frequency range, the skin effect and the dielectric loss behavior describe the propagation behavior, and a high phase velocity shows up. His work will be briefly reviewed and a discussion of the physical phenomena will occur in Chapter four.

In 1971, Hasegawa published his classical paper defining three fundamental propagation modes (the quasi-TEM mode, the slow-wave mode, and the skin-effect

mode) for the MIS structure [3]. The slow-wave mode was found to propagate within the resistivity-frequency range suited for monolithic circuit technology back at that time. The analytical analysis is similar to Guckel's work [2] and it still ignores the fringing effect. However, in his measurements of test structures, the effect of the width of microstrip line is analyzed for the case of slow-wave mode. The analysis is performed through equivalent circuits based on low-frequency approximations and is thus limited by accuracy.

After Hasegawa's classical work, several papers have been published based on the numerical full-wave or quasi-TEM analyses [3]-[8]. The emphasis of the work is often on extracting the frequency dependent parameters R(f), C(f), L(f), G(f) [9]-[11]. These parameters can then be used in available CAD circuit design simulators (eg. SPICE) to get instant results of the interconnect effect. Thus, it accelerates the chip design process.

These works all show the progress in the investigation of on-chip interconnects characteristics. They have focused on propagation modes, crosstalk, substrate dispersion and loss in various ways [2]-[12]. However, in order to either simplify the electromagnetic formulation in the analytical derivation, or shrink the calculation model size, computer storage and processing overhead in the numerical method, these works either assume the thickness of the metal to be zero and make the quasi-TEM assumptions, or ignore the fringing effect of the interconnects. In addition, for the frequencies used nowadays, interconnects with lossy substrate will operate in the skin effect mode and transition region (This is the region between the

well defined three modes, which will be discussed in Chapter four). Little work has been published in this research area.

Crosstalk on coupled microstrip lines is another important topic in the problem of signal integrity. Closed-Form derivations [11], Quasi-Analytical analysis [12], Finite-Difference Time-Domain (FDTD) method [13], Spectral Domain approach (SDA) [14]-16] etc. have been used in crosstalk analysis. However, all these works have the same assumptions as the MIS structure analysis. A brief introduction of these numerical method is given in Chapter two.

Global on-chip interconnects modeling also shows progress. The Multiconductor Transmission Line Methodology (MTL) [17], The Statistical model [18] etc, have shown examples of global on-chip interconnect design. However this problem is more complicated than simple interconnect structures, so more assumptions and more simplifications have to be made. The discussion of the global on-chip interconnects modeling is beyond the work of this thesis.

1.2 Motivations of the Work

Previous research shows that the analytical method, as well as some numerical modeling methods (Spectral domain method [14]-[16], Transmission line matrix method [19], etc. These methods are discussed in Chapter two.) require numerous assumptions to simplify the model. The assumptions sacrifice the accuracy of the analysis. The FDTD method has its advantages in solving Maxwell Equations. But as the density of elements on-chip increases, operating frequency increases, and signal rising-falling time decreases. Because of the stability problem inherent in the FDTD

algorithm, the simulation model increases dramatically and the simulation time becomes very long. These limitations will be explained in Chapter two.

In 1999, Namiki presented the Alternating-Direction-Implicit Finite-Difference Time-Domain (ADI-FDTD) method [20]. This method has overcome the stability limitations in the FDTD algorithm. It does not have the conflict of time step and grid size that appears in the conventional FDTD method. Using this method, numerous signal propagating problems in the time-domain can be solved.

In this work, a 3-D ADI-FDTD solver is built and is used to analyze various transmission line characteristic problems, such as dispersion in the substrate, substrate loss and signal attenuation. The definition and analysis of these can be found in Chapter four.

During the study of various physical problems with the ADI-FDTD solver, we found sometimes the method will blow up, and numerical reflections on the boundary may occur occasionally. This stimulates us to investigate the factors affecting the stability and accuracy of the numerical method. The introduction of numerical algorithms as well as the evaluation of numerical behaviors can be found in Chpater two and three.

1.3 Thesis Structures

In Chapter two, numerical methods used in electromagnetic analysis are reviewed. The conventional FDTD method, which is the foundation of the ADI-FDTD method used in this thesis, is explained in detail with discussions on the numerical stability, dispersion and other concerns.

The derivation of the ADI-FDTD algorithm is presented in Chapter 3. The theoretical stability and numerical dispersion analysis of the ADI-FDTD method is discussed mathematically. The practical choice of time-step, grid-size is also discussed. The flow chart of the algorithm is demonstrated.

In Chapter 4, we performed the highly efficient unconditionally stable ADI-FDTD method on a classical Metal-Insulator-Silicon-Metal (MISM) structure. We first benchmark the ADI-FDTD method by comparing the numerical result obtained from the ADI-FDTD method to the experimental data published in the literature. The numerical result is also compared with the analytical analysis. Then, we further present the advantages of our analysis. In particular, we are able to show the detailed field distribution in the thin skin-depth layer in the metal and in the silicon substrate. This has not been published in the literature so it helps to explain the important phenomena, such as energy flow, conductor loss and semiconductor loss.

A summary and future works are given at the end of the thesis.

Chapter 2: Physical and Numerical Method in Interconnects Analysis

Signal propagation along on-chip interconnects is a complicated wave propagation problem. In order to solve Maxwell's equations, researchers have developed closed form and analytical solutions. With the progress in digital computer, numerical solutions such as finite difference (FD) method, finite element method (FEM) and integral equation formulations are becoming popular. We will have a brief review of selected numerical method uses in interconnects analysis, and discuss the Finite-Difference Time-Domain (FDTD) method in detail.

2.1 Physical Model of the Interconnects

Different physical models with various assumptions and simplifications have been performed in the Metal-Insulator-Silicon-Metal (MISM) interconnects study. According to [21], physical models are divided into four main categories: analytical or empirical lumped circuit models, parallel-plate waveguide models, planar multi-layered multi-conductor transmission line models, and combined electromagnetic and device simulation models.

The first physical model is the **analytical lumped circuit model**. In general, analytical lumped circuit models will provide fast calculation and instant insight to the performance of interconnects. However, they are restricted to certain simplified situations. The lumped-capacitance model assumes that signal rise/fall times are much larger than signal propagation time. However, this assumption is not true for modern high-speed VLSI. Figure 1 gives the performance enhancement of

interconnects as the technology advances [22]. The MOSFET switching delay is approximately equal to the signal rise/fall time. The interconnect RC response time is the propagation delay of interconnect. It is the time needed for a signal to travel from one point on the interconnect to another. The term "RC" comes from the lumped equivalent circuit model of interconnect. Under the 100nm technology, the time that takes the signal to travel along the interconnect (the propagation delay) is larger than the MOSFET switching delay (signal rise/fall times). Thus, the interconnect can no longer be viewed as a lumped model. The transmission line effect of the interconnect has to be taken into account.

Interconnect Performance Requirements

	Technology Generation		
	1.0 μm	100 nm	35 nm
MOSFET Switching Delay Interconnect "RC" Response Time (L_{int} = 1 mm)	~ 20 ps ~ 1 ps	~ 5 ps ~ 30ps	~ 2.5 ps ~ 250 ps
MOSFET Switching Energy Interconnect Switching Energy (L_{int} = 1 mm)	~ 300 *f*J ~ 400 *f*J	~ 2 *f*J ~ 10 *f*J	~ 0.1 *f*J ~ 3 *f*J
Clock Frequency	~ 30 MHz	~ 2-3.5 GHz	~ 3.6-13.5 GHz
Supply Current (V_{dd} = 5.0, 1.0, 0.5 V)	~ 2.5 A	~ 150 A	~ 360 A
Maximum Number of Wiring Levels	3	8-9	10
Maximum Total Wire Length per Chip	~ 100 m	~ 5000 m	( )
Chip Pad Count	~200	~ 3000-4000	4000-4400

Figure 1 Example of interconnects performance improvement with technology. Switching delay, interconnect RC response time are major aspects we are interested here [22].

Hasegawa and Seki [23] have shown that using lumped-capacitance models for interconnections is not applicable if switching times are less than 100 ps, which is almost always the case for present IC industries. In conclusion, the first physical model of interconnects is inapplicable on long interconnects in modern IC's.

The second physical model is the **parallel-plate waveguide model**. Parallel-plate waveguide models study the MISM structure by ignoring the fringing effect and assuming the metal line has infinite width. This problem can be solved by solving Maxwell's equations in each region while satisfying the boundary conditions on the interface. The propagation constants can be resolved from this method and the electric field and magnetic field can also be obtained. Based on this method, Guckel [2] and Hasegawa [3] proposed the foundation of the three fundamental propagation modes (the quasi-TEM mode, the slow-wave mode, and the skin-effect mode) theory in interconnects research area. However, this method requires regular structures to derive the solutions. It might not be available to decompose complicated line structures into regular regions, which makes it inapplicable. Also, for complicated structures with regular regions, the analytical problems become more difficult to solve, and the detailed field distribution in different materials is very hard to obtain.

Real on-chip interconnects usually have multi-conductor lines. The third physical model is the **planar multi-layered multi-conductor transmission line model**. This model is based on the full-wave analysis results and is found to best represent real on-chip interconnects structures. The different full-wave analysis includes the spectral domain analysis (SDA) method [15], the method of lines (MOL) [24], the transmission line matrix (TLM) method [25], the finite-difference time-domain (FDTD) method [8], the finite element method (FEM) [5], and the boundary element method (BEM) [26] etc.. A short introduction of these full-wave analysis methods can be found in the next two sections.

The last physical model is to combine the electromagnetic and device simulation together and solve coupled electromagnetic and device equations at the same time. When the electromagnetic wave is propagating along the MISM structure, there are two mechanisms affecting the field and energy distribution: One is the attenuation effect arising from the energy dissipation; the other is the screening effect of the carriers in the semiconductor that prohibits the field from penetrating into the semiconductor. The first mechanism is described by Maxwell's equations, while the second is described by the device transportation equations. This combined physical model allows the analysis to include carrier accumulation and depletion factors, screening effect of the carriers, and propagation properties of the electromagnetic waves along the MISM interconnects[27][30]. With this model, the interaction between the electromagnetic field and the movement of carriers in the semiconductor can be discovered.

2.2 Numerical Method in Interconnects Analysis Overview

Three major categories of numerical techniques are used in the electromagnetic analysis of MISM structures [21]: The quasi-TEM analysis, the frequency-domain full-wave analysis and the time-domain full-wave analysis.

2.2.1 Quasi-TEM analysis

Quasi-TEM analysis simulates the wave propagating in the MISM structures as Transverse Electromagnetic (TEM) wave. This means we assume the transmission line system has two lossless conductors. Strictly speaking, the MISM structure can not support the TEM wave, because of its inherent dissipation of the structure.

However, according to different research reports [3], [28] and [29], if the longitudinal electric field is much less than the transverse electric field of the mode, the quasi-TEM approximation is applicable. This is easy to understand. There are no longitudinal field components in an ideal TEM wave. Only transverse field components will exist. That is, only the field components perpendicular to the propagating direction are allowed in TEM wave.

According to [29], the quasi-TEM analysis is valid to switching speeds of 7 ps in 1989. The upper bound is more stringent in today's technique. In GHz frequency range, where interconnect radiates like an antenna, the effect of loss in the substrate is more and more important. The quasi-TEM assumption does not hold anymore, and the effect of the substrate loss has to be taken into account.

2.2.2 Frequency-Domain Full-Wave analysis

The frequency-domain full-wave analysis solves the variations of the original Maxwell's equations. For example, the time-harmonic Maxwell's equations, the Helmholtz wave equations, and the integral equations derived from the wave equations using the Green's function. The first two lead to differential methods, such as the finite difference method (FD) [30] or the finite element method (FEM) [5]. The third one yields integral equation methods, such as the boundary element method (BEM) [26] or the spectral domain analysis (SDA) [14]-[16] method.

The Spectral Domain Approach (SDA) [14]-[16] applies the Green's function in the Fourier transform domain (This is also known as spectral domain). The Green's function has a much simpler form in the spectral domain than in the space domain, which makes the SDA method very efficient.

Some advantages of the SDA method are [16]:

- Multi-layer, multi-conductor structures are easily modeled.
- Since it is a frequency-domain method, it can be used for all the frequency dependent conductivities, and all the frequencies.
- It is fast and efficient for planar and quasi-planar guiding structures.

Some disadvantages of the SDA method are [16]:

- This method bases on the Green's function. For a general configuration or inhomogeneous material, the Green's function may not exist.

The Finite Difference (FD) method approximates Maxwell's differential equations with the finite differences. It comes from the Taylor's expansion of the partial differential equations. The Finite Difference (FD) method is easy to implement, but it is best suitable for simple boundary problems. The curved boundary is generally approximated by a staircased approximation and will introduce extra errors in addition to the finite difference discretization error. Fortunately, in general the boundary of the MISM structure can be simulated exactly with proper arrangement of the mesh in Cartesian coordinates.

The Finite Element Method (FEM) can also be applied to study the performance of the MISM interconnects [5]. In FEM, the simulation domain is first discretized into small element, then, each element is mapped into a standard element with a local coordination. Fields are expressed in the form of interpolation functions in each local element. All the local elements are assembled together with proper boundary conditions to form an algebraic system.

Some advantages of the finite element method for wave problems are [26]:

- Complex geometries are easily modeled (eg. The curved boundaries).
- Boundary conditions are implicit.
- Nonhomogeneous materials are easily accommodated.
- The coefficient matrix is banded, sparse, symmetric, and positive definite.

Some disadvantages of the finite element method are [26]:

- It is difficult to represent open boundaries.
- The unknowns must be solved for throughout the whole domain even if the solution is required only at a few points.

Both the FEM and FD methods use a differential approach, which requires a large number of meshes to implement the absorbing boundary condition for the unbounded problems.

The Boundary Element Method (BEM) is an integral method based on Green's theorem. Maxwell's equations are transformed into integral equations on the boundaries of the simulation domain. To implement this method, only the mesh on the interface of the material is necessary.

Some advantages of the BEM for wave applications are [26]:

- BEM method can model the open boundary problem with less mesh.
- Numerical accuracy is generally greater than that of the FEM.
- BEM can easily model curved boundaries.
- The unknowns are only on the boundaries, and it's efficient to solve the problem.

Some disadvantages of the BEM are [26]:

- It is not convenient to represent nonlinear or non-homogeneous materials [17].
- The coefficient matrix is full and is not guaranteed to be positive definite.

2.2.3 Time-Domain Full-Wave analysis

The time-domain full-wave analysis is preferred if a transient analysis is desired. There are two widely used time-domain full-wave analysis method: The finite-difference time-domain (FDTD) method and the time-domain Transmission Line (Matrix) Modelling (TLM) method [31].

Transmission Line (Matrix) Modelling (TLM) method solves electromagnetic wave problems in the time domain. It approximates the exact solution by discretizing the solution domain into a network of transmission lines. The voltage and current on the nodes of the transmission line network provide the information of the electric and magnetic fields. At one time-step, voltage pulses first incident upon each transmission-line. According to the scattering matrix determined by the Maxwell's equations, these pulses will be scattered to produce a new set of pulses. These new pulses will incident on adjacent nodes at the next time-step. The major advantage of the TLM method is the capability of studying the transient responses and its simplicity in implementation.

The Finite-Difference Time-Domain (FDTD) method solves the original Maxwell's curl equations in the time domain. The traditional FDTD method is computationally expensive and has the difficulty to handle frequency-dependent

interactions such as material dispersion and metal skin effects [21]. In the next two sections in this chapter, we will review the FDTD in detail, since it acts as the foundation of the ADI-FDTD method applied in the MISM analysis. It is especially worth mentioning here that the FDTD method needs to be implemented with caution to avoid numerical instability. The reason will be explained in section 2.4.2.

2.3 Maxwell Equations and Yee's Cell

2.3.1 Maxwell's Equations for the FDTD method

Among the various numerical methods mentioned in the previous section, the Finite-Difference Time-Domain (FDTD) method is found to be very attractive in solving Maxwell's equations of the electromagnetic problems. It is the basis of the Alternating-Direction-Implicit Finite-Difference Time-Domain (ADI-FDTD) method. Thus, we will spend a few sections here to introduce this method.

Generally speaking, FDTD is simple and flexible. Since it is a time-domain method, when the excitation is a narrow pulse with a large bandwidth, one single run of the simulation can provide information over a large bandwidth. The basis of the FDTD algorithm is the two Maxwell curl equations in derivative form in the time domain. By means of central difference, these equations are expressed in linear forms. With the introduction of Yee's grid, the FDTD matches Maxwell's equations in space and time very well, and the implementation is very straight forward. It is well suited to computing responses to a continuous wave or single-frequency excitation, and particularly well suited to computing transient responses.

We introduce the FDTD method from the differential form of Maxwell's equations introduced by James Clark Maxwell in 1873. Maxwell's equations are shown below (2-1)-(2-4).

Ampere's Law

$$\nabla \times \vec{H} = \frac{\partial \vec{D}}{\partial t} + \vec{J}_e \tag{2-1}$$

Faraday's Law

$$\nabla \times \vec{E} = -\frac{\partial \vec{B}}{\partial t} - \vec{J}_m \tag{2-2}$$

Gauss's Law for the electric field:

$$\nabla \cdot \vec{D} = \rho \tag{2-3}$$

Gauss's Law for the magnetic field (No isolated magnetic charge):

$$\nabla \cdot \vec{B} = 0 \tag{2-4}$$

Here, $\vec{E}$ is the electric field vector (V/m); $\vec{D}$ is the electric flux density vector (C/m); $\vec{H}$ is the magnetic field vector (A/m); $\vec{B}$ is the magnetic flux density vector (Web/m^2); $\vec{J}_e$ is the electric conduction current density (A/m^2); and $\vec{J}_m$ is the equivalent magnetic conduction current density (V/m^2).

In linear and isotropic materials (i.e. materials having field-independent, frequency-independent, and direction-independent electric and magnetic properties), the constitutive relations are:

$$\vec{D} = \varepsilon \vec{E} \tag{2-5}$$

$$\vec{B} = \mu \vec{H} \tag{2-6}$$

Here, ε is the electric permittivity (F/m), and μ is the magnetic permeability (H/m). The equivalent electric current $\vec{J}_e$, and the equivalent magnetic current $\vec{J}_m$

refer to the electric and magnetic losses separately. The dissipation of electromagnetic fields will convert into heat energy.

$$\vec{J}_e = \sigma \vec{E} \tag{2-7}$$

$$\vec{J}_m = \rho' \vec{H} \tag{2-8}$$

Here, σ is the electric conductivity (S/m), and ρ' is an equivalent magnetic resistivity (Ω/m). It is easy to show that only considering the two curl equations in Maxwell's equations is sufficient. Furthermore, the two divergence equations for Gauss's Law need not be explicitly enforced. Substituting (2-5) - (2-8) into (2-2) - (2-1), we have

$$\frac{\partial \vec{H}}{\partial t} = -\frac{1}{\mu} \nabla \times \vec{E} - \frac{\rho'}{\mu} \vec{H} \tag{2-9}$$

$$\frac{\partial E}{\partial t} = \frac{1}{\varepsilon} \nabla \times \vec{H} - \frac{\sigma}{\varepsilon} \vec{E} \tag{2-10}$$

Writing out the vector components of the above curl equations yields the following six coupled scalar equations in the three-dimensional Cartesian coordinate system:

$$\frac{\partial H_x}{\partial t} = \frac{1}{\mu} \left(\frac{\partial E_y}{\partial z} - \frac{\partial E_z}{\partial y} - \rho' H_x \right) \tag{2-11a}$$

$$\frac{\partial H_y}{\partial t} = \frac{1}{\mu} \left(\frac{\partial E_z}{\partial x} - \frac{\partial E_x}{\partial z} - \rho' H_y \right) \tag{2-11b}$$

$$\frac{\partial H_z}{\partial t} = \frac{1}{\mu} \left(\frac{\partial E_x}{\partial y} - \frac{\partial E_y}{\partial x} - \rho' H_z \right) \tag{2-11c}$$

$$\frac{\partial E_x}{\partial t} = \frac{1}{\varepsilon} \left(\frac{\partial H_z}{\partial y} - \frac{\partial H_y}{\partial z} - \sigma E_x \right) \tag{2-12a}$$

$$\frac{\partial E_y}{\partial t} = \frac{1}{\varepsilon} \left(\frac{\partial H_x}{\partial z} - \frac{\partial H_z}{\partial x} - \sigma E_y \right) \tag{2-12b}$$

$$\frac{\partial E_z}{\partial t} = \frac{1}{\varepsilon}\left(\frac{\partial H_y}{\partial x} - \frac{\partial H_x}{\partial y} - \sigma E_z\right) \tag{2-12c}$$

This system of six coupled partial differential equations forms the basis of the FDTD numerical algorithm in three-dimensions. Two-dimensional and one-dimensional formulations can be easily derived according to (2-11) and (2-12) by letting the corresponding dimensions go to infinity.

2.3.2 Yee's cell and the formulas of the FDTD method

In 1966, Kane Yee originated a set of finite-difference equations for the time-dependent Maxwell's curl equations for a lossless system [32]. We will show the three-dimension formulas of the Finite-Difference Time-Domain methods based on the Yee's grid (Figure 2).

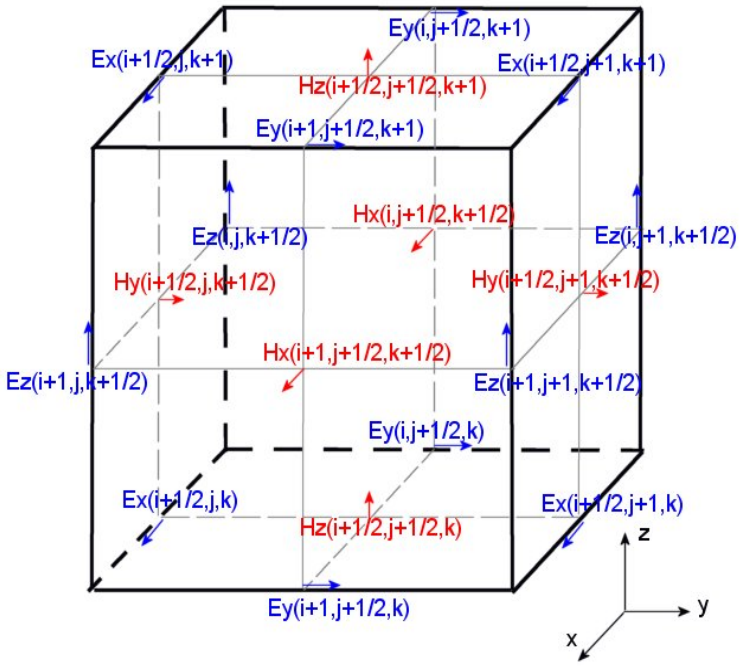

Figure 2 Yee's Cell for programming convenience

To begin our development, consider a one-dimension Maxwell's equation for lossless media (2-11b):

$$\frac{\partial H_y}{\partial t} = \frac{1}{\mu}\frac{\partial E_z}{\partial x} \tag{2-13}$$

From the classical definition of a derivative, we have

$$\lim_{\Delta t \to 0} \frac{\Delta H_y}{\Delta t} = \frac{1}{\mu} \lim_{\Delta t \to 0} \frac{\Delta E_z}{\Delta x} \tag{2-14}$$

From Figure 3, we note that in the limit a continuous and an exact solution to (2-14) is obtained at the point (x, t). It is important to note that at this point, Maxwell's equations do not directly yield electric and magnetic field values, but rather relate the rate of change between electric and magnetic field values.

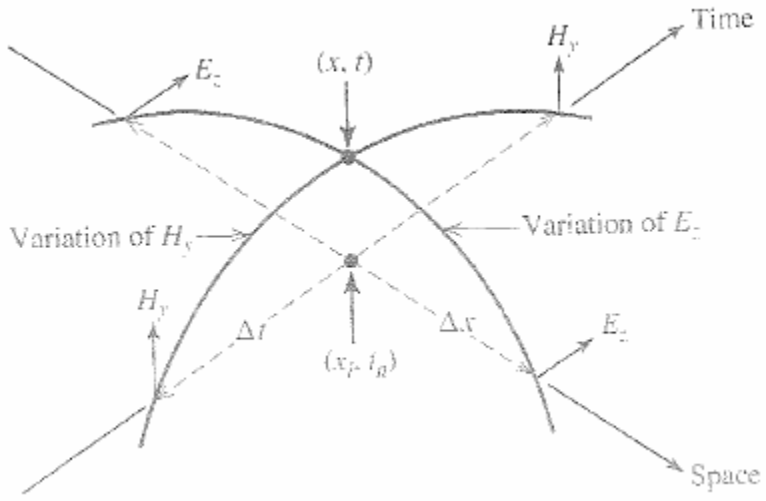

Figure 3 Space-time graphical interpretation of a one-dimensional component of Maxwell's equations and its discretization. (Originated by Eric Thiele, quoted in [33]).

We then apply the central differences to relate the derivatives of the neighboring discrete fields. The subscription i is for space, and superscript n is for

time. Any field component u as a function of space and time evaluated at a discrete point in the space lattice and at a discrete point in time is denoted as

$$u(i\Delta x, n\Delta t) = u_i^n \tag{2-15}$$

So now (2-14) becomes

$$H_i^{n+1/2} = H_i^{n-1/2} + \frac{\Delta t}{\mu \Delta x}\left(E_{i+1/2}^n - E_{i-1/2}^n\right), \tag{2-16}$$

This implies that we can solve for $H_i^{n+1/2}$ if we know the value for H at the same spatial point but at Δt earlier in time, and the value of E at spatial points $\pm\Delta x/2$ away from x_i and $\Delta t/2$ earlier in time.

It is thus natural to extend this idea into a three dimensional case. The arrangement of E field and H field components on the Yee's cell is shown in Figure 2. In three-dimensions , the time and space notation is

$$u(i\Delta x, j\Delta y, k\Delta z, n\Delta t) = u_{i,j,k}^n \tag{2-17}$$

At time step n, the Maxwell's curl equation (2-11a) on lattice point $\left(i\Delta x, (j+1/2)\Delta y, (k+1/2)\Delta z\right)$ can be discretized into (2-18a). Similarly, the curl equation (2-11b) on lattice point $\left((i+1/2)\Delta x, j\Delta y, (k+1/2)\Delta z\right)$ can be discretized into (2-18b), and (2-11c) on lattice point $\left((i+1/2)\Delta x, (j+1/2)\Delta y, k\Delta z\right)$ can be discretized into (2-18c).

$$\frac{H_x\,|_{i,j+1/2,k+1/2}^{n+1/2} - H_x\,|_{i,j+1/2,k+1/2}^{n-1/2}}{\Delta t} = \frac{1}{\mu_{i,j+1/2,k+1/2}} \begin{pmatrix} \dfrac{E_y\,|_{i,j+1/2,k+1}^n - E_y\,|_{i,j+1/2,k}^n}{\Delta z} \\ -\dfrac{E_z\,|_{i,j+1,k+1/2}^n - E_z\,|_{i,j,k+1/2}^n}{\Delta y} \\ -\rho'_{i,j+1/2,k+1/2} \cdot H_x\,|_{i,j+1/2,k+1/2}^n \end{pmatrix} \tag{2-18a}$$

$$\frac{H_y\,|_{i+1/2,j,k+1/2}^{n+1/2} - H_y\,|_{i+1/2,j,k+1/2}^{n-1/2}}{\Delta t} = \frac{1}{\mu_{i+1/2,j,k+1/2}} \begin{pmatrix} \dfrac{E_z\,|_{i+1,j,k+1/2}^{n} - E_z\,|_{i,j,k+1/2}^{n}}{\Delta x} \\ -\dfrac{E_x\,|_{i+1/2,j,k+1}^{n} - E_x\,|_{i+1/2,j,k}^{n}}{\Delta z} \\ -\rho'_{i+1/2,j,k+1/2} \cdot H_y\,|_{i+1/2,j,k+1/2}^{n} \end{pmatrix} \quad \text{(2-18b)}$$

$$\frac{H_z\,|_{i+1/2,j+1/2,k}^{n+1/2} - H_z\,|_{i+1/2,j+1/2,k}^{n-1/2}}{\Delta t} = \frac{1}{\mu_{i+1/2,j+1/2,k}} \begin{pmatrix} \dfrac{E_x\,|_{i+1/2,j+1,k}^{n} - E_x\,|_{i+1/2,j,k}^{n}}{\Delta y} \\ -\dfrac{E_y\,|_{i+1,j+1/2,k}^{n} - E_y\,|_{i,j+1/2,k}^{n}}{\Delta x} \\ -\rho'_{i+1/2,j+1/2,k} \cdot H_z\,|_{i+1/2,j+1/2,k}^{n} \end{pmatrix} \quad \text{(2-18c)}$$

At time step n+1/2, the Maxwell's curl equation (2-12a) on lattice point $((i+1/2)\Delta x, j\Delta y, k\Delta z)$ can be discretized into (2-19a). Similarly, the curl equation (2-12b) on lattice point $(i\Delta x, (j+1/2)\Delta y, k\Delta z)$ can be discretized into (2-19b), and (2-12c) on lattice point $(i\Delta x, j\Delta y, (k+1/2)\Delta z)$ can be discretized into (2-19c).

$$\frac{E_x\,|_{i+1/2,j,k}^{n+1} - E_x\,|_{i+1/2,j,k}^{n}}{\Delta t} = \frac{1}{\varepsilon_{i+1/2,j,k}} \begin{pmatrix} \dfrac{H_z\,|_{i+1/2,j+1/2,k}^{n+1/2} - H_z\,|_{i+1/2,j-1/2,k}^{n+1/2}}{\Delta y} \\ -\dfrac{H_y\,|_{i+1/2,j,k+1/2}^{n+1/2} - H_y\,|_{i+1/2,j,k-1/2}^{n+1/2}}{\Delta z} \\ -\sigma_{i+1/2,j,k} \cdot E_x\,|_{i+1/2,j,k}^{n+1/2} \end{pmatrix} \quad \text{(2-19a)}$$

$$\frac{E_y\,|_{i,j+1/2,k}^{n+1} - E_y\,|_{i,j+1/2,k}^{n}}{\Delta t} = \frac{1}{\varepsilon_{i,j+1/2,k}} \begin{pmatrix} \dfrac{H_x\,|_{i,j+1/2,k+1/2}^{n+1/2} - H_x\,|_{i,j+1/2,k-1/2}^{n+1/2}}{\Delta z} \\ -\dfrac{H_z\,|_{i+1/2,j+1/2,k}^{n+1/2} - H_z\,|_{i-1/2,j+1/2,k}^{n+1/2}}{\Delta x} \\ -\sigma_{i,j+1/2,k} \cdot E_y\,|_{i,j+1/2,k}^{n+1/2} \end{pmatrix} \quad \text{(2-19b)}$$

$$\frac{E_z\,|_{i,j,k+1/2}^{n+1} - E_z\,|_{i,j,k+1/2}^{n}}{\Delta t} = \frac{1}{\varepsilon_{i,j,k+1/2}} \left(\begin{array}{l} \dfrac{H_y\,|_{i+1/2,j,k+1/2}^{n+1/2} - H_y\,|_{i-1/2,j,k+1/2}^{n+1/2}}{\Delta x} \\ -\dfrac{H_x\,|_{i,j+1/2,k+1/2}^{n+1/2} - H_x\,|_{i,j-1/2,k+1/2}^{n+1/2}}{\Delta y} \\ -\sigma_{i,j,k+1/2} \cdot E_z\,|_{i,j,k+1/2}^{n+1/2} \end{array} \right) \qquad \text{(2-19c)}$$

According to Yee [32], E field is always calculated on time-step n,n+1, etc; H field is always calculated on time-step n+1/2, n+3/2, etc. In (2-18), the magnetic field terms on the right hand side are H^n's, which are not stored in computer memory. Only the previous values of H at time step $n-\frac{1}{2}$ are stored in memory. We could get a good estimation of this intermediate value by different approximations. For example, using the central difference at time-step n:

$$H\,|^n = \frac{H\,|^{n+1/2} + H\,|^{n-1/2}}{2} \quad . \qquad \text{(2-20)}$$

Now (2-18a) becomes

$$\frac{H_x\,|_{i,j+1/2,k+1/2}^{n+1/2} - H_x\,|_{i,j+1/2,k+1/2}^{n-1/2}}{\Delta t} = \frac{1}{\mu_{i,j+1/2,k+1/2}} \left(\begin{array}{l} \dfrac{E_y\,|_{i,j+1/2,k+1}^{n} - E_y\,|_{i,j+1/2,k}^{n}}{\Delta z} \\ -\dfrac{E_z\,|_{i,j+1,k+1/2}^{n} - E_z\,|_{i,j,k+1/2}^{n}}{\Delta y} \\ -\rho'_{i,j+1/2,k+1/2} \cdot \dfrac{H_x\,|_{i,j+1/2,k+1/2}^{n-1/2} + H_x\,|_{i,j+1/2,k+1/2}^{n+1/2}}{2} \end{array} \right). \qquad \text{(2-21a)}$$

We combine the coefficients of the field terms at the same space and same time step, and move the yet to be calculated value (unknown value) to the left hand side and the stored field terms (known) to the right hand side. This yields the following:

$$\left(1+\frac{\Delta t}{\mu_{i,j+1/2,k+1/2}}\frac{\rho'_{i,j+1/2,k+1/2}}{2}\right)H_x\,|^{n+1/2}_{i,j+1/2,k+1/2}=\left(1-\frac{\Delta t}{\mu_{i,j+1/2,k+1/2}}\frac{\rho'_{i,j+1/2,k+1/2}}{2}\right)H_x\,|^{n-1/2}_{i,j+1/2,k+1/2}$$
$$+\frac{\Delta t}{\mu_{i,j+1/2,k+1/2}}\begin{pmatrix}\dfrac{E_y\,|^n_{i,j+1/2,k+1}-E_y\,|^n_{i,j+1/2,k}}{\Delta z}\\ -\dfrac{E_z\,|^n_{i,j+1,k+1/2}-E_z\,|^n_{i,j,k+1/2}}{\Delta y}\end{pmatrix}$$

(2-21b)

Normalizing the field on the left hand side yields

$$H_x\,|^{n+1/2}_{i,j+1/2,k+1/2}=\left(\frac{1-\dfrac{\Delta t}{\mu_{i,j+1/2,k+1/2}}\dfrac{\rho'_{i,j+1/2,k+1/2}}{2}}{1+\dfrac{\Delta t}{\mu_{i,j+1/2,k+1/2}}\dfrac{\rho'_{i,j+1/2,k+1/2}}{2}}\right)H_x\,|^{n-1/2}_{i,j+1/2,k+1/2}$$
$$+\left(\frac{\dfrac{\Delta t}{\mu_{i,j+1/2,k+1/2}}}{1+\dfrac{\Delta t}{\mu_{i,j+1/2,k+1/2}}\dfrac{\rho'_{i,j+1/2,k+1/2}}{2}}\right)\begin{pmatrix}\dfrac{E_y\,|^n_{i,j+1/2,k+1}-E_y\,|^n_{i,j+1/2,k}}{\Delta z}\\ -\dfrac{E_z\,|^n_{i,j+1,k+1/2}-E_z\,|^n_{i,j,k+1/2}}{\Delta y}\end{pmatrix}$$

(2-21c)

Similarly, we can reorganize the formulas for (2-19) with $E\,|^{n+1/2}=\dfrac{E\,|^{n+1}+E\,|^n}{2}$.

In summary, we now have

$$H_x\,|^{n+1/2}_{i,j+1/2,k+1/2}=\left(\frac{1-\dfrac{\Delta t}{\mu_{i,j+1/2,k+1/2}}\dfrac{\rho'_{i,j+1/2,k+1/2}}{2}}{1+\dfrac{\Delta t}{\mu_{i,j+1/2,k+1/2}}\dfrac{\rho'_{i,j+1/2,k+1/2}}{2}}\right)H_x\,|^{n-1/2}_{i,j+1/2,k+1/2}$$
$$+\left(\frac{\dfrac{\Delta t}{\mu_{i,j+1/2,k+1/2}}}{1+\dfrac{\Delta t}{\mu_{i,j+1/2,k+1/2}}\dfrac{\rho'_{i,j+1/2,k+1/2}}{2}}\right)\begin{pmatrix}\dfrac{E_y\,|^n_{i,j+1/2,k+1}-E_y\,|^n_{i,j+1/2,k}}{\Delta z}\\ -\dfrac{E_z\,|^n_{i,j+1,k+1/2}-E_z\,|^n_{i,j,k+1/2}}{\Delta y}\end{pmatrix}$$

(2-22a)

$$H_y\,|_{i+1/2,j,k+1/2}^{n+1/2}=\left(\frac{1-\dfrac{\Delta t}{\mu_{i+1/2,j,k+1/2}}\dfrac{\rho'_{i+1/2,j,k+1/2}}{2}}{1+\dfrac{\Delta t}{\mu_{i+1/2,j,k+1/2}}\dfrac{\rho'_{i+1/2,j,k+1/2}}{2}}\right)H_y\,|_{i+1/2,j,k+1/2}^{n-1/2}$$
$$+\left(\frac{\dfrac{\Delta t}{\mu_{i+1/2,j,k+1/2}}}{1+\dfrac{\Delta t}{\mu_{i+1/2,j,k+1/2}}\dfrac{\rho'_{i+1/2,j,k+1/2}}{2}}\right)\left(\frac{E_z\,|_{i+1,j,k+1/2}^{n}-E_z\,|_{i,j,k+1/2}^{n}}{\Delta x}-\frac{E_x\,|_{i+1/2,j,k+1}^{n}-E_x\,|_{i+1/2,j,k}^{n}}{\Delta z}\right)$$

(2-22b)

$$H_z\,|_{i+1/2,j+1/2,k}^{n+1/2}=\left(\frac{1-\dfrac{\Delta t}{\mu_{i+1/2,j+1/2,k}}\dfrac{\rho'_{i+1/2,j+1/2,k}}{2}}{1+\dfrac{\Delta t}{\mu_{i+1/2,j+1/2,k}}\dfrac{\rho'_{i+1/2,j+1/2,k}}{2}}\right)H_z\,|_{i+1/2,j+1/2,k}^{n-1/2}$$
$$+\left(\frac{\dfrac{\Delta t}{\mu_{i+1/2,j+1/2,k}}}{1+\dfrac{\Delta t}{\mu_{i+1/2,j+1/2,k}}\dfrac{\rho'_{i+1/2,j+1/2,k}}{2}}\right)\left(\frac{E_x\,|_{i+1/2,j+1,k}^{n}-E_x\,|_{i+1/2,j,k}^{n}}{\Delta y}-\frac{E_y\,|_{i+1,j+1/2,k}^{n}-E_y\,|_{i,j+1/2,k}^{n}}{\Delta x}\right)$$

(2-22c)

$$E_x\,|_{i+1/2,j,k}^{n+1}=\left(\frac{1-\dfrac{\sigma_{i+1/2,j,k}\Delta t}{2\varepsilon_{i+1/2,j,k}}}{1+\dfrac{\sigma_{i+1/2,j,k}\Delta t}{2\varepsilon_{i+1/2,j,k}}}\right)E_x\,|_{i+1/2,j,k}^{n}+\left(\frac{\dfrac{\Delta t}{\varepsilon_{i+1/2,j,k}}}{1+\dfrac{\sigma_{i+1/2,j,k}\Delta t}{2\varepsilon_{i+1/2,j,k}}}\right)\left(\frac{H_z\,|_{i+1/2,j+1/2,k}^{n+1/2}-H_z\,|_{i+1/2,j-1/2,k}^{n+1/2}}{\Delta y}-\frac{H_y\,|_{i+1/2,j,k+1/2}^{n+1/2}-H_y\,|_{i+1/2,j,k-1/2}^{n+1/2}}{\Delta z}\right)$$

(2-23a)

$$E_y\,|_{i,j+1/2,k}^{n+1}=\left(\frac{1-\dfrac{\sigma_{i,j+1/2,k}\Delta t}{2\varepsilon_{i,j+1/2,k}}}{1+\dfrac{\sigma_{i,j+1/2,k}\Delta t}{2\varepsilon_{i,j+1/2,k}}}\right)E_y\,|_{i,j+1/2,k}^{n}+\left(\frac{\dfrac{\Delta t}{\varepsilon_{i,j+1/2,k}}}{1+\dfrac{\sigma_{i,j+1/2,k}\Delta t}{2\varepsilon_{i,j+1/2,k}}}\right)\left(\frac{H_x\,|_{i,j+1/2,k+1/2}^{n+1/2}-H_x\,|_{i,j+1/2,k-1/2}^{n+1/2}}{\Delta z}-\frac{H_z\,|_{i+1/2,j+1/2,k}^{n+1/2}-H_z\,|_{i-1/2,j+1/2,k}^{n+1/2}}{\Delta x}\right)$$

(2-23b)

$$E_z\,|_{i,j,k+1/2}^{n+1} = \left(\frac{1 - \dfrac{\sigma_{i,j,k+1/2}\Delta t}{2\varepsilon_{i,j,k+1/2}}}{1 + \dfrac{\sigma_{i,j,k+1/2}\Delta t}{2\varepsilon_{i,j,k+1/2}}} \right) E_z\,|_{i,j,k+1/2}^{n} + \left(\frac{\dfrac{\Delta t}{\varepsilon_{i,j,k+1/2}}}{1 + \dfrac{\sigma_{i,j,k+1/2}\Delta t}{2\varepsilon_{i,j,k+1/2}}} \right) \left(\frac{H_y\,|_{i+1/2,j,k+1/2}^{n+1/2} - H_y\,|_{i-1/2,j,k+1/2}^{n+1/2}}{\Delta x} - \frac{H_x\,|_{i,j+1/2,k+1/2}^{n+1/2} - H_x\,|_{i,j-1/2,k+1/2}^{n+1/2}}{\Delta y} \right)$$

(2-23c)

Yee's algorithm is one of the gridding methods of greatest use since its fundamental basis is so robust. The Yee algorithm is robust for the reasons that follow [33].

First, Yee's algorithm is useful because it solves for both electric an magnetic fields in time and space using the coupled Maxwell's curl equations rather than solving for the electric field alone (or the magnetic field alone) as with the wave equation.

In addition, in Yee's cell, every $\vec{E}$ field vector component is surrounded by four $\vec{H}$ field components, and every $\vec{H}$ field component is surrounded by four $\vec{E}$ field components, as illustrated in Figure 2. This provides a simple picture of three-dimensional space being filled by an interlinked array of Faraday's Law and Ampere's Law contours. The continuity of the tangential $\vec{E}$ is naturally maintained across an interface of dissimilar materials if the interface is parallel to one of the grid coordinate axes (This is proven in section 2.4.4). The resulting finite-difference expressions for the space derivatives are central in nature (central-difference) and second-order accurate.

Further, the Yee algorithm centers the $\vec{E}$ and $\vec{H}$ field vector components in time in what is termed as the leapfrog arrangement. This algorithm says: All the $\vec{E}$ field computations in the three-dimensional space of interest are computed for a particular time point using the most recently computed $\vec{H}$ field data stored in the

computer memory; Then, all the $\vec{H}$ field computations in the three-dimensional space are computed using the $\vec{E}$ field data just computed and stored in memory.

Finally, Yee's algorithm is robust because no matrices are involved and no large systems of simultaneous equations need to be solved.

The FDTD approach based on the Yee algorithm is a straightforward method. In summary, the time-stepping flowchart of the FDTD method is given in Figure 4. At time zero, all the E field and H field are set to zero.

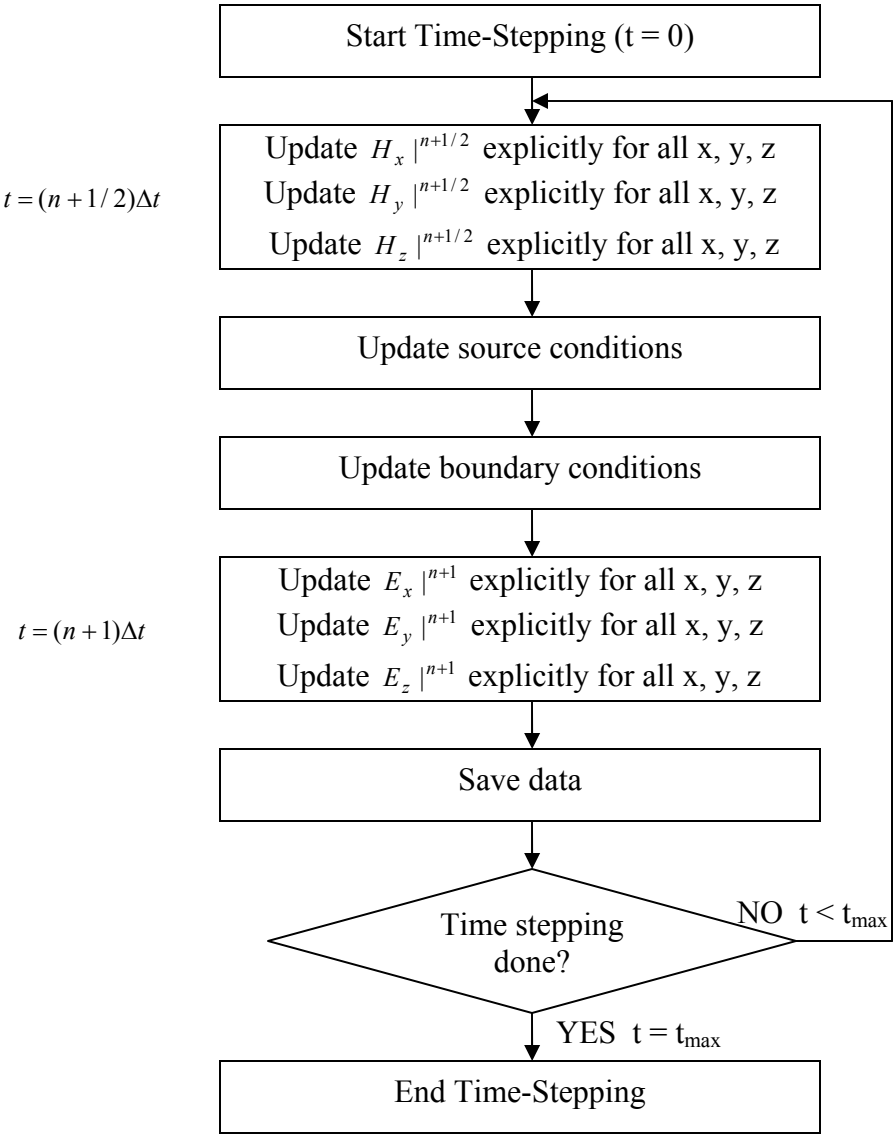

Figure 4 Flowchart of FDTD time-stepping process

2.4 FDTD Concerns

2.4.1 Cell size

The choice of cell size is very important in FDTD. It must be small enough to permit accurate results at the highest frequency of interest, and yet be large enough to keep resource requirements manageable.

From the Fourier analysis we know that for a pulse of width τ, the major portion of the frequency spectrum lies between zero and $f_u = 1/\tau$. The Nyquist sampling theorem would suggest that the cell size be less than $\lambda_u/2$ in order for the spatial variation of the fields to be adequately sampled. However, the pulse also has the frequency content higher than f_u so that not only will the numerical dispersion (Waves with different frequencies may travel at different velocities in the computational lattice.) appear, but also the differential equations are themselves approximations (because the higher order terms in the Taylor expansion are ignored, except for the magic time steps where the finite difference is an exact solution). A general agreement is that the cell size should be smaller than $\frac{\lambda_u}{10}$ in the material medium to obtain some desired accuracy and minimize the effects of the numerical dispersion. It has been proven that reducing the grid dispersion error to an acceptable level can be readily accomplished by reducing the cell size. People usually choose cell sizes smaller than $\frac{\lambda_u}{20}$ if computational resources allow. The reason for this will be shown in the dispersion discussion in section 2.4.3.

Another consideration in cell size is that the problem geometry must be accurately modeled. Thus, if the target problem has fine geometrical structures, the

cell size should be smaller than what is necessary to resolve the field within the fine structure. This cell size might be stricter than the frequency limit in some cases.

2.4.2 Numerical Stability and Time Step Size

Once the cell size is determined, the maximum size of the time step Δt immediately follows from the Courant condition. Let's first consider a plane wave propagating through the one-dimensional FDTD grid. In one time step, any point on this wave can only propagate from one cell to its nearest neighbors. Trying to use even a slightly larger time step will quickly lead to numerical instability. On the other hand, we can do less than one cell in one time step, but it is not an optimum situation and will not lead to increased accuracy. Suppose our plane wave is propagating most rapidly between the FDTD grid (Figure 5). If the uniform grid size is Δh and the time step is Δt, then, the Courant Condition in the one-dimensional case is

$$v\Delta t \le \Delta h . \tag{2-24}$$

v is the maximum velocity of propagation in that medium (c in free space).

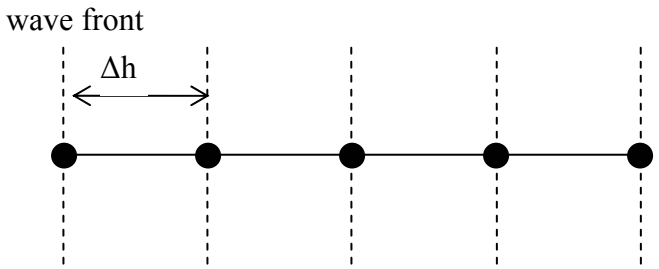

Figure 5 Stability for the one-dimensional FDTD mesh [26]

It is not hard to imagine the 2-D case, where the maximum propagating direction is perpendicular to the diagonal (Figure 6), and the Courant Condition is also (2-24).

Except here

$$\Delta h = \frac{\Delta x \Delta y}{\sqrt{\Delta x^2 + \Delta y^2}} = \frac{1}{\sqrt{\frac{1}{\Delta x^2} + \frac{1}{\Delta y^2}}} \tag{2-25}$$

$$\Delta t \le \frac{1}{v\sqrt{\frac{1}{\Delta x^2} + \frac{1}{\Delta y^2}}} \tag{2-26}$$

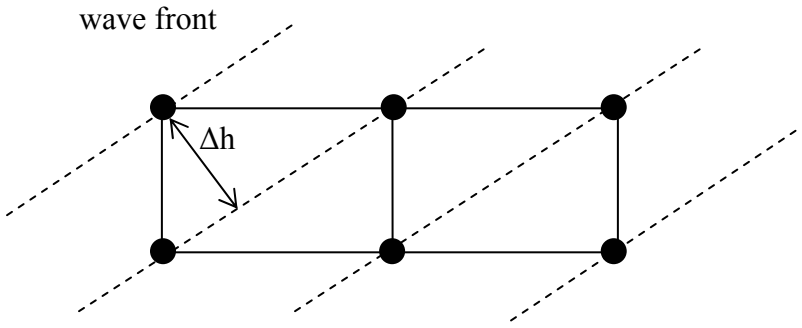

Figure 6 Stability for the two-dimensional FDTD mesh [26]

Similarly, the Courant Condition in 3-D is

$$\Delta t \le \frac{1}{v\sqrt{\frac{1}{\Delta x^2} + \frac{1}{\Delta y^2} + \frac{1}{\Delta z^2}}} \ . \tag{2-27}$$

A rigorous derivation of the Courant Stability Condition can be found in [34]. The derivation is based on solving the eigenvalue problem. A mathematically strict derivation for the stability condition in the ADI-FDTD method will be skipped here to be succinct, but it is performed in the next chapter for completeness. It is worth mentioning that the derivation is focused on the Yee's algorithm in Cartesian coordinates. A more generalized stability problem arises due to the interactions between the Yee's algorithm and augmenting algorithms used to model the boundary

conditions, the variable and unstructured meshing, and the lossy, dispersive, nonlinear, and gain materials.

Although in some complex problems, the exact stability criterion cannot be derived, a part analytical (or part empirical) upper bound on the time step can still be derived so that the numerical stability is maintained for many thousands of time steps, if not indefinitely.

2.4.3 Numerical Dispersion

Another important issue to the Finite-Difference Time-Domain (FD-TD) numerical algorithm for Maxwell's curl equations is the numerical dispersion. Waves with different frequencies may travel at different velocities in the computational lattice.

Numerical dispersion is different from physical dispersion. Physical dispersion is also called analog dispersion. Physical dispersion comes from the wave function directly. Numerical dispersion comes from the discretization and iteration formulas for the physical problem. Although to some extent, these two dispersions are the same (we can show that when the grid in space and the time steps in time go to zero, these two dispersions are the same.), generally speaking, they are different.

In order to derive the numerical dispersion relation, let's assume a normalized region of lossless space where $\mu = 1$, $\varepsilon = 1$, $\sigma = 0$, $\rho' = 0$, and $c = 1$. We can then write the two Maxwell's curl equations in a compact form [34]

$$j\nabla \times \vec{V} = \frac{\partial \vec{V}}{\partial t} \quad , \tag{2-28}$$

Here, $\vec{V} = \vec{H} + j\vec{E}$.

Suppose the vector-field traveling-wave expression is

$$\vec{V}\,|_{I,J,K}^{n} = \vec{V}_0 e^{j(\tilde{k}_x I\Delta x + \tilde{k}_y J\Delta y + \tilde{k}_z K\Delta z - \omega n\Delta t)} \tag{2-29}$$

Substituting (2-29) into the Yee space-time central-differencing form of (2-28), we have

$$\left[\frac{\hat{x}}{\Delta x}\sin\left[\frac{\tilde{k}_x\Delta x}{2}\right] + \frac{\hat{y}}{\Delta y}\sin\left[\frac{\tilde{k}_y\Delta y}{2}\right] + \frac{\hat{z}}{\Delta z}\sin\left[\frac{\tilde{k}_z\Delta z}{2}\right]\right] \times \vec{V}\,|_{I,J,K}^{n} = \frac{j}{\Delta t}\vec{V}\,|_{I,J,K}^{n}\ \sin\left(\frac{\omega\Delta t}{2}\right) \tag{2-30}$$

Here, $\hat{x}$, $\hat{y}$ and $\hat{z}$ are unit vectors in the x-, y-, and z- directions. $\tilde{k}_x = \tilde{k}\sin\theta\sin\phi$, $\tilde{k}_y = \tilde{k}\sin\theta\cos\phi$, $\tilde{k}_z = \tilde{k}\cos\theta$. The tilde on top of the k vectors refers to the numerical wave number, which differs from the physical wave number. We can look at (2-30) as a linear system where V_x, V_y and V_z are the unknown vectors. In order to get a unique solution, the determinant of the above eigenvalue system should be zero, giving us

$$\left[\frac{1}{\Delta t}\sin\left(\frac{\omega\Delta t}{2}\right)\right]^2 = \left[\frac{1}{\Delta x}\sin\left(\frac{\tilde{k}_x\Delta x}{2}\right)\right]^2 + \left[\frac{1}{\Delta y}\sin\left(\frac{\tilde{k}_y\Delta y}{2}\right)\right]^2 + \left[\frac{1}{\Delta z}\sin\left(\frac{\tilde{k}_z\Delta z}{2}\right)\right]^2 \tag{2-31}$$

After denormalizing to a nonunity free space speed of light c, the general form of the numerical dispersion relation for the full vector-field Yee's algorithm in three dimensions is

$$\left[\frac{1}{c\Delta t}\sin\left(\frac{\omega\Delta t}{2}\right)\right]^2 = \left[\frac{1}{\Delta x}\sin\left(\frac{\tilde{k}_x\Delta x}{2}\right)\right]^2 + \left[\frac{1}{\Delta y}\sin\left(\frac{\tilde{k}_y\Delta y}{2}\right)\right]^2 + \left[\frac{1}{\Delta z}\sin\left(\frac{\tilde{k}_z\Delta z}{2}\right)\right]^2 \tag{2-32}$$

Solving $\tilde{k}$ in (2-32) will give us the numerical dispersion relationship. $\tilde{k}$ is a function of grid size, time-step size, frequency and propagating direction through the grid net. Because $\tilde{k}$ is different from the physical wavenumber k, the numerical

phase velocity of the wave also differs from physical velocity c (in free space), and it is defined as

$$\tilde{v}_p = \frac{\omega}{\tilde{k}}. \tag{2-33}$$

The normalized phase velocity is (assuming in free space):

$$\frac{\tilde{v}_p}{c} = \frac{\omega}{c\tilde{k}} = \frac{\omega/c}{\tilde{k}} = \frac{k}{\tilde{k}} \tag{2-34}$$

The physical wavenumber is $k = \frac{2\pi}{\lambda_0}$, λ_0 is the wave length in free space. If we use the normalized wave length $\lambda_0 = 1$, then

$$\frac{\tilde{v}_p}{c} = \frac{k}{\tilde{k}} = \frac{2\pi/\lambda_0}{\tilde{k}} = \frac{2\pi}{\tilde{k}}. \tag{2-35}$$

Thus, we can evaluate the numerical dispersion through studying the relation between $\tilde{k}$ and Δt, θ, φ etc.. We introduce the so called Courant number here to relate dispersion study with stability limit (2-36). Because of the Courant stability condition (2-27), CFL must be always equal or less than 1 in FDTD algorithm.

$$CFL = c\Delta t\sqrt{\frac{1}{\Delta x^2} + \frac{1}{\Delta y^2} + \frac{1}{\Delta z^2}} \tag{2-36}$$

First, we show the numerical dispersion in a two-dimensional problem. In two-dimensions (for example, in the x-y plane), dispersion relation (2-32) reduces to

$$\left[\frac{1}{c\Delta t}\sin\left(\frac{\omega\Delta t}{2}\right)\right]^2 = \left[\frac{1}{\Delta x}\sin\left(\frac{\tilde{k}_x\Delta x}{2}\right)\right]^2 + \left[\frac{1}{\Delta y}\sin\left(\frac{\tilde{k}_y\Delta y}{2}\right)\right]^2. \tag{2-37}$$

In (2-37), $\tilde{k}_x = \tilde{k}\cos\alpha$, and $\tilde{k}_y = \tilde{k}\sin\alpha$, where $\tilde{k}$ is the numerical wavenumber, and α is the propagation angle with respect to the positive x-axis. We solve (2-37) over different grid size, time-step size and propagating direction for $\tilde{k}$. The results

are in Figure 7. We compare high CFL ($CFL = 0.9 \approx 1$, Figure 7 (a)), medium CFL ($CFL = 0.6$, Figure 7 (b)), and low CFL ($CFL = 0.1$, Figure 7 (c)) for square cell ($\Delta x = \Delta y$), and rectangular cell $(\Delta x \neq \Delta y)$ with high CFL ($CFL = 0.9 \approx 1$, Figure 7 (d)).

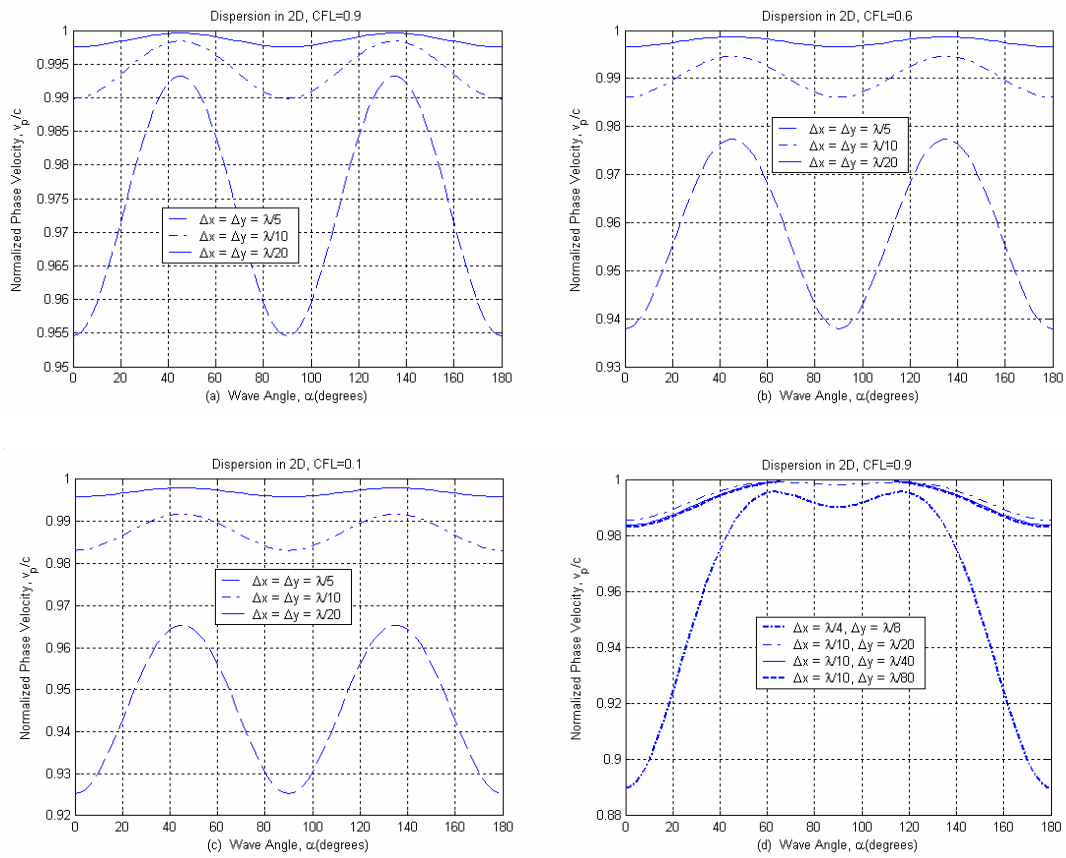

Figure 7 Numerical dispersion relationship of a TM wave. The x-axis is propagation direction. Different cell sizes, CFL numbers are compared.

Figure 7 (a)-(c) shows stronger dispersion when the wave is propagating along the grid ($\alpha = 0, \pi/2, \pi$) for square cells, and less dispersion when the wave is propagating towards the diagonal of the grid ($\alpha = \pi/4$) for square cells. When the number of cells per wave length is increased (This means reducing cell size and increasing resolution), the dispersion along different directions is reduced significantly. The difference between different propagating directions in finer cell cases are smaller than that in coarser cell cases. This means, if the solution has dispersion, it is more uniformly distributed along different traveling direction for finer cells. We also find

dispersion is larger if the CFL number is smaller. In order to keep the dispersion small, we should choose the CFL number as large as possible (the maximum CFL is 1, according to (2-27)), and use smaller cells, as long as the simulation burden is bearable. Figure 7(d) shows dispersion for rectangular cells. We find the dispersion is minimized when the wave propagates along the direction of Δh (Δh is defined in Figure 6).

Figure 7 also tells us the general convention of using at least 20 cells per wavelength will introduce very little numerical dispersion and higher accuracy if the iteration is not infinite. This explains why people will generally put at least 20 cells per wavelength in their geometry settings.

We now solve (2-34) with Newton Raphson method, and study the dispersion relation in a 3D scheme. Again, we discuss the dispersion with respect to propagating angle, cell size and CFL number. In 3D case, there are two angles: φ is the angle in the x-y plane, and θ is the angle from z axis to the x-y plane (Figure 8).

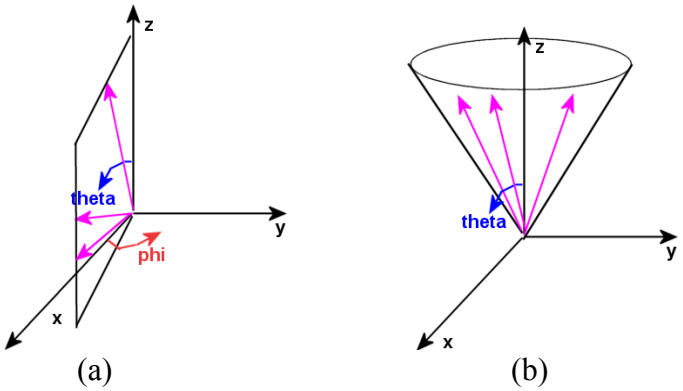

Figure 8 Dispersion surface definition

(a) planes perpendicular to xy plane
(b) cone suface plane with z as the axle

Figure 9 analyzes the dispersion on planes parallel to the z axis (Figure 8 (a)). $\varphi = 0^o$, $\varphi = 30^o$, $\varphi = 45^o$, $\varphi = 60^o$ and $\varphi = 90^o$ planes are all perpendicular to x-y plane. On these planes, waves propagating along different θ have different phase velocities. Figure 10 shows dispersion of cubic cells ($\Delta x = \Delta y = \Delta z$) on cone surfaces (Figure 8(b)). The axle of these cones is the z axis. Radiuses of these cones vary with the value of θ. In both Figure 9 and 10, we vary the CFL number from 0.1 to 0.9. We perform similar investigation in Figure 11 and 12, except now the edge of the cell in one direction is

defined to be smaller than the rest two directions. We find again that the larger the CFL number, the less dispersion occurs. For cubic cells, the minimum dispersion occurs when the wave travels along the cubic diagonal direction. This can be viewed as we collapse the 3D problem into 1D. The equivalent CFL number along the cubic diagonal direction is larger than the equivalent CFL number along other directions. The minimum dispersion occurs when the CFL number is maximized. We are expecting that for non-cubic cells, the minimum dispersion occurs when the wave propagates perpendicular to the "lattice planes" with the shortest intervals. Along this direction, the collapsed 1D problem has the maximum CFL number. The "lattice plane" is a term we borrowed from the solid state physics. Here the primary lattice is the Yee's cell (cubic, or non-cubic). This trend can be seen from Figure 11 and 12. A rigorous proof is our future work.

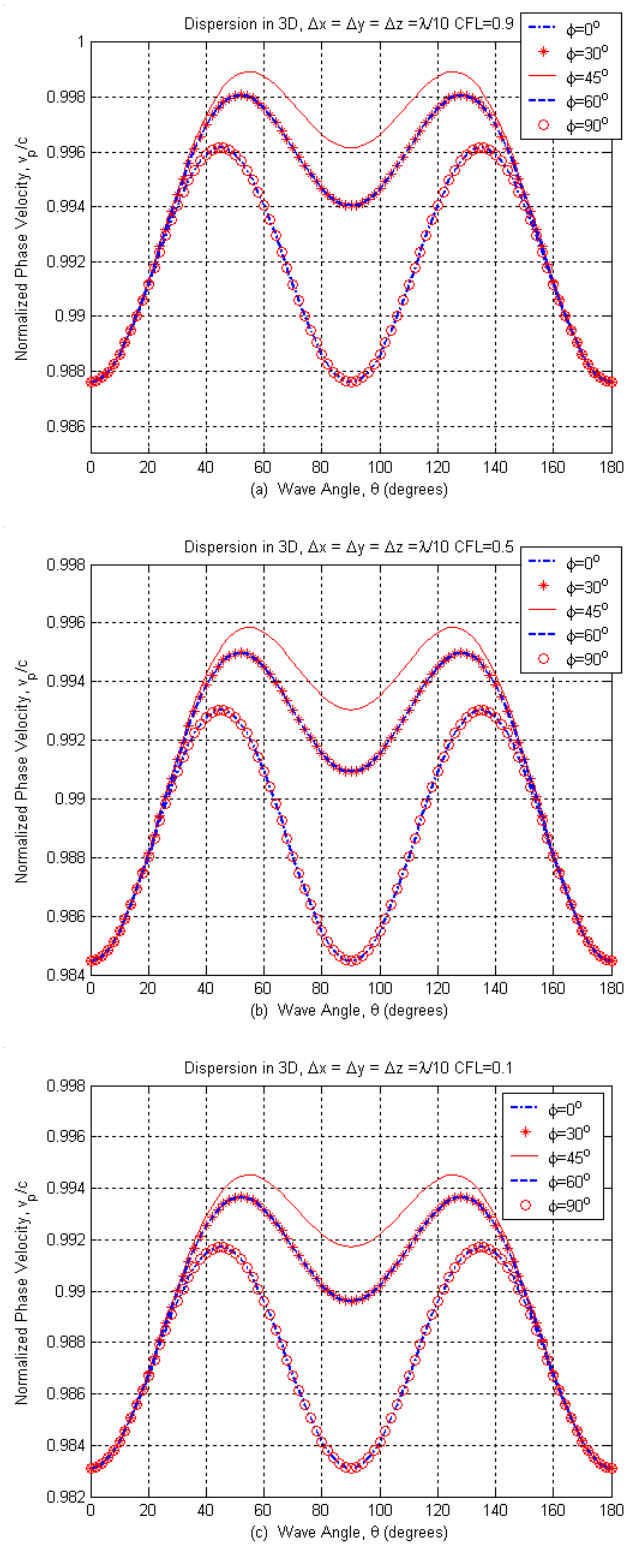

Figure 9 Numerical dispersion of cubic cells on planes perpendicular to x-y plane in 3D FDTD. Different propagation directions, CFL numbers are compared.

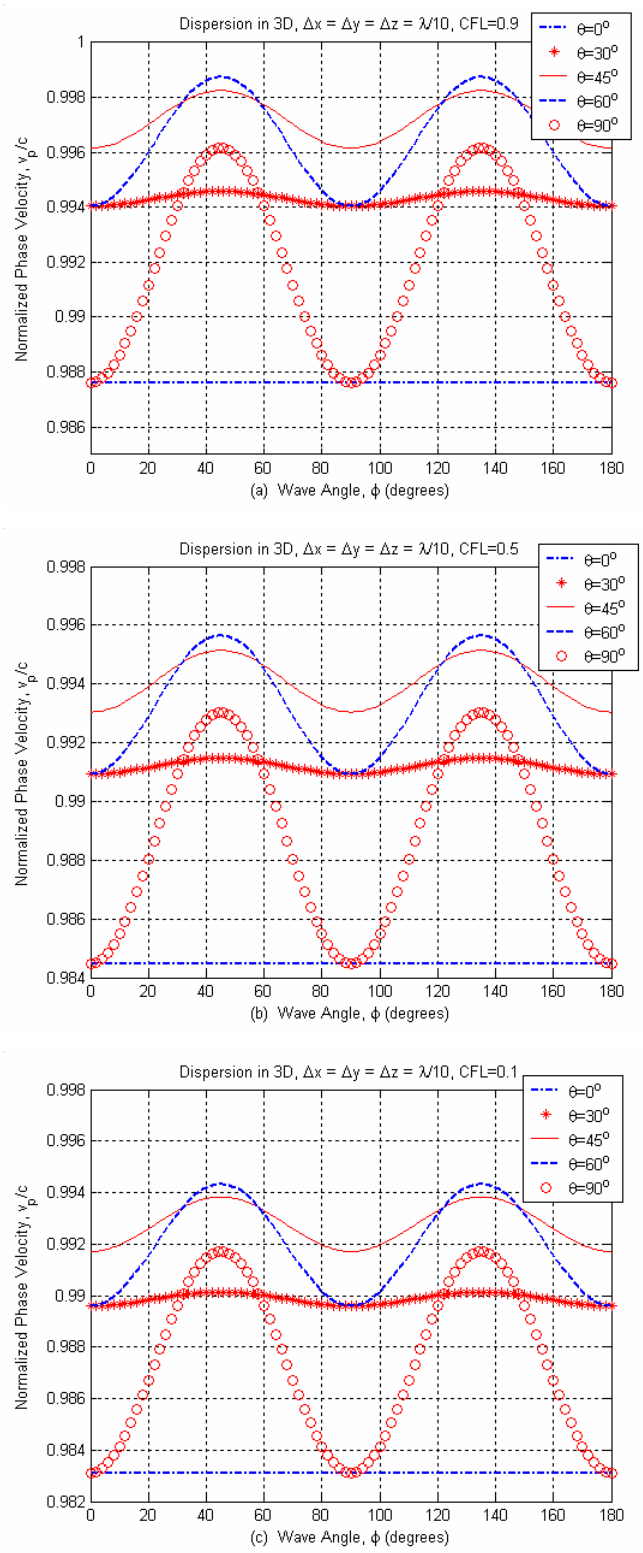

Figure 10 Numerical dispersion of cubic cells on cone surfaces with z as the axle in 3D FDTD. Different propagation directions, CFL numbers are compared.

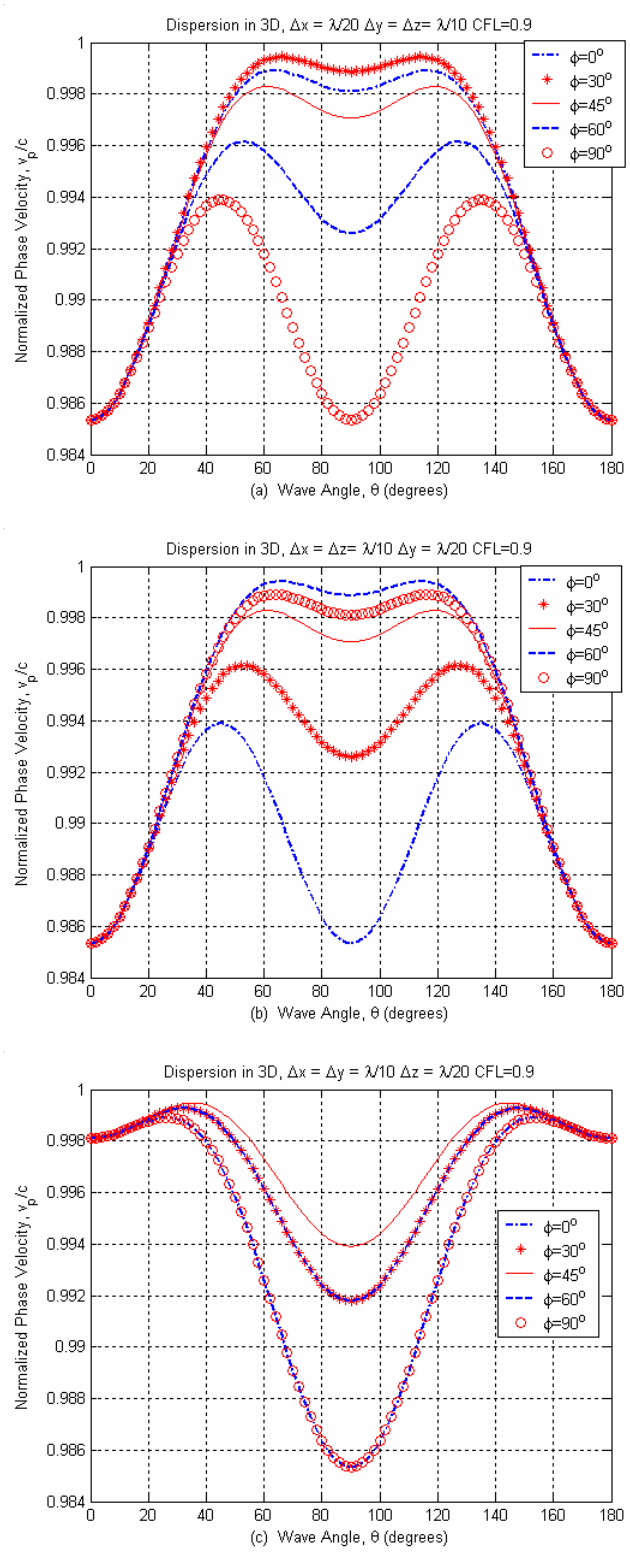

Figure 11 Numerical dispersion of non-cubic cells on planes perpendicular to x-y plane in 3D FDTD. Different propagation directions, CFL numbers are compared.

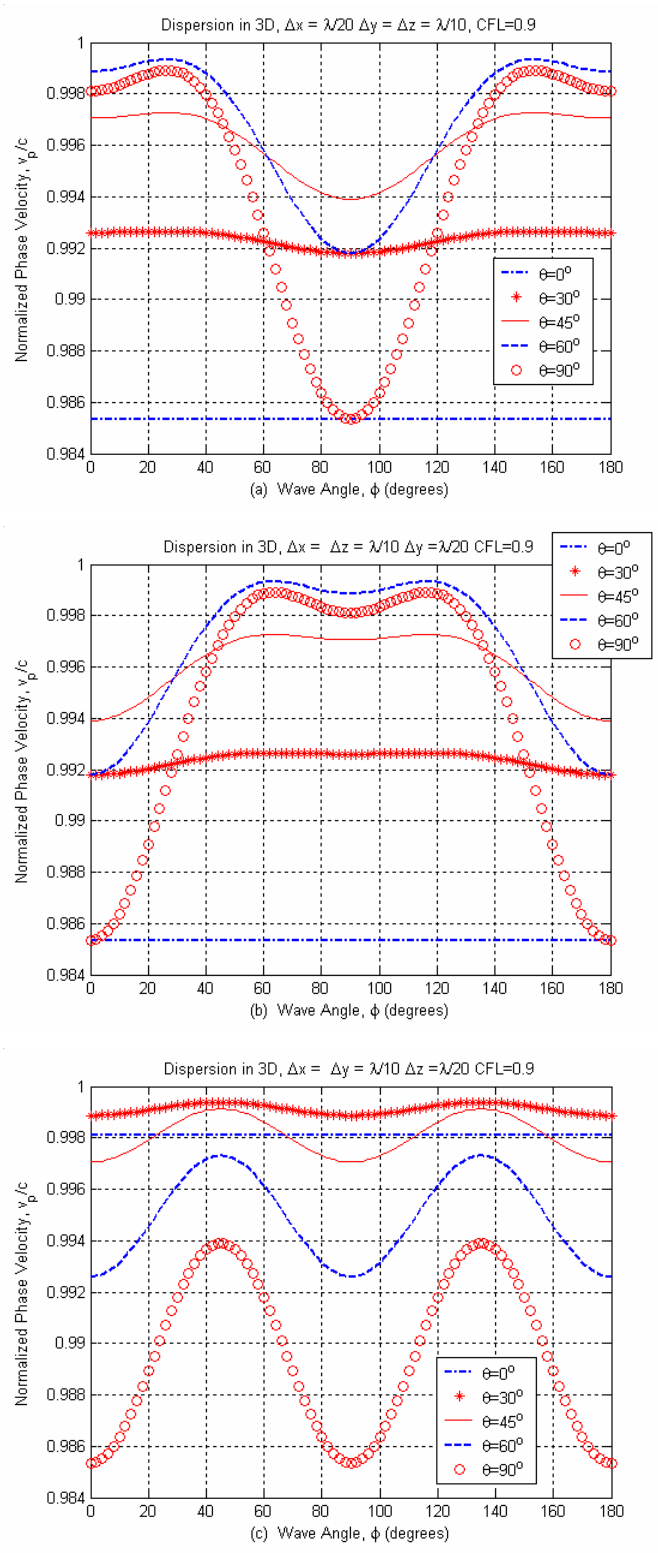

Figure 12 Numerical dispersion of non-cubic cells on cone surfaces with z as the axle in 3D FDTD. Different propagation directions, CFL numbers are compared.

2.4.4 Boundary Conditions

Our major interest in this thesis is to simulate the MISM structure, which is illustrated in Figure 21 in Chapter 4. We summarized the "boundary" of our problem in physical world as follows: A ground metal plane is at the bottom of the substrate. This ground plane is assumed to be an ideal metal plane. This means, the tangential electric field on the surface of the ground plane is zero. On top of the MISM, the open air region exists. The excitation is added to one side of the metal line (we call this side the starting plane of the metal line). There is no reflections at the other end of the metal line (we call this end the ending plane of the metal line). This means the metal line has matched loads, or the metal line is infinitely long. The region to the left and right side of the metal line goes to infinity (open region).

In numerical simulation, we have to build numerical formulas that can properly model the above physical boundaries.

PEC boundary condition

We will use the Perfect Electrical Conductor (PEC) boundary condition on the ideal ground metal plane. On the surface of this boundary, all the tangential electric fields are zeroes. Because the electric fields are located at the edge of the each Yee's cell, we must put the cell edge at the boundary edge in order to implement this boundary condition. For example, if the bottom plane of the Yee's cell is the ideal ground metal plane in Figure 2, then the bottom face is the surface where the PEC is located. Setting the tangential components of the electric field to be zero results in:

$$E_x\,|^n_{i+1/2,j,k} = E_x\,|^n_{i+1/2,j+1,k} = E_y\,|^n_{i,j+1/2,k} = E_y\,|^n_{i+1,j+1/2,k} = 0 \qquad (2\text{-}38)$$

ABC (Absorbing Boundary Conditions)

In real world the chip is usually in an open region. However, the computation domain must have a limited size, since no computer can store and operate on infinity number of data. The FDTD simulation must be performed in a finite domain, which requires the truncation of the open region. We defined the finite simulation domain by putting one air plane on top of the MISM structure, four side walls on each side of the MISM structure, and one ground plane at the bottom of this structure. The boundary condition on the bottom ground plane is already discussed in the previous section. We will discuss the other five boundary planes here.

If the computational domain is extended far from sources and scatterers, electromagnetic waves can be assumed to propagate outwards the boundary. Proper boundary conditions have to be added on the truncation plane to minimize the artificial reflections on the boundary. The Absorbing Boundary Conditions (ABC) will simulate the model as if there is no reflection on the truncation interface. This is useful in simulating the truncated open region or the guided-wave problems with matched termination loads. Therefore, ABC's will be performed on the top air plane, the side walls and the ending plane of the metal line. A survey of different ABC's can be found in [34]. Mur's boundary condition [35] is one of the most popular ABC's. The first order Mur's boundary condition is very easy to implement and will achieve good accuracy. The second order Mur's boundary condition is derived in uniform space and has larger spurious wave if the boundary has dielectric discontinuities [35]. Thus, we will use the first order Mur's boundary condition in our concerns.

The FDTD method uses Yee's cell as its fundamental components, where the electric field is always on the edge of the cell. Therefore, on each boundary plane, there exist only the tangential electric field components and the normal magnetic field components.

From the wave equation,

$$\left(\frac{\partial^2}{\partial x^2}+\frac{\partial^2}{\partial y^2}+\frac{\partial^2}{\partial z^2}-\frac{1}{c^2}\frac{\partial^2}{\partial t^2}\right)\vec{E}=0 \tag{2-39}$$

According to Mur's original work [35], we introduce the operators D_x, D_y and D_z to represent the inverse of the velocity along different coordinates. We can then split the wave equation into each x, y, and z directions:

$$\frac{1}{c^2}=D_x^2+D_y^2+D_z^2=\mu\varepsilon \tag{2-40}$$

$$\left(\frac{\partial^2}{\partial x^2}+\frac{\partial^2}{\partial y^2}+\frac{\partial^2}{\partial z^2}-\frac{1}{c^2}\frac{\partial^2}{\partial t^2}\right)\vec{E}=$$
$$\left(\left(\frac{\partial}{\partial x}+D_x\frac{\partial}{\partial t}\right)\left(\frac{\partial}{\partial x}-D_x\frac{\partial}{\partial t}\right)+\left(\frac{\partial}{\partial y}+D_y\frac{\partial}{\partial t}\right)\left(\frac{\partial}{\partial y}-D_y\frac{\partial}{\partial t}\right)+\left(\frac{\partial}{\partial z}+D_z\frac{\partial}{\partial t}\right)\left(\frac{\partial}{\partial z}-D_z\frac{\partial}{\partial t}\right)\right)\vec{E}=0 \tag{2-41}$$

The plus and minus signs in each bracket demonstrate the wave is traveling along the negative or positive direction of the corresponding Cartesian axes. For example, $\left(\frac{\partial}{\partial y}+D_y\frac{\partial}{\partial t}\right)\vec{E}=0$ represent an electric field propagating along the positive y direction; $\left(\frac{\partial}{\partial y}-D_y\frac{\partial}{\partial t}\right)\vec{E}=0$ represent an electric field propagating along the negative y direction. Considering the boundary at y=0, only the E_x and E_z field are on the

boundary according to the Yee's cell (Figure 2). We will take E_x traveling toward the negative y direction as an example to derive the Mur's first boundary condition.

$$\left(\frac{\partial}{\partial y}-D_y\frac{\partial}{\partial t}\right)E_x=0=\left(\frac{\partial}{\partial y}-\sqrt{\frac{1}{c^2}-D_x^2-D_z^2}\,\frac{\partial}{\partial t}\right)E_x=\left(\frac{\partial}{\partial y}-\frac{1}{c}\sqrt{1-c^2D_x^2-c^2D_z^2}\,\frac{\partial}{\partial t}\right)E_x \quad (2\text{-}42)$$

Applying the first order Taylor's expansion on the square root will give us the Mur's first Boundary Condition:

$$\sqrt{1-c^2D_x^2-c^2D_z^2}\approx 1-\frac{1}{2}\left(\left(cD_x\right)^2+\left(cD_z\right)^2\right)+H.O.T.\approx 1 \quad (2\text{-}43)$$

This approximation is valid only when $(cD_x)^2+(cD_z)^2$ is very small. If the wave incidents normally to the boundary (y=0 plane), the velocity in the x and z directions is much less than it in the y direction. $D_y\approx\frac{1}{c}$. This condition will be satisfied. The wave incidents to the boundary almost in a normal direction:

$$\left(\frac{\partial}{\partial y}-D_y\frac{\partial}{\partial t}\right)E_x=0\approx\left(\frac{\partial}{\partial y}-\frac{1}{c}\frac{\partial}{\partial t}\right)E_x\,|_{y=0} \quad (2\text{-}44a)$$

(2-44a) is the Mur's first boundary condition for E_x on y=0 plane.

To implement (2-44a) in the FDTD scheme, we will perform the central difference at time step n+1/2, on lattice point $((i+1/2)\Delta x,1/2,k\Delta z)$.

$$\begin{aligned}\frac{\partial}{\partial y}E_x\,|_{i+1/2,1/2,k}^{n+1/2}&=\frac{E_x\,|_{i+1/2,1,k}^{n+1/2}-E_x\,|_{i+1/2,0,k}^{n+1/2}}{\Delta y}\\&=\left(\frac{E_x\,|_{i+1/2,1,k}^{n+1}+E_x\,|_{i+1/2,1,k}^{n}}{2\Delta y}-\frac{E_x\,|_{i+1/2,0,k}^{n+1}+E_x\,|_{i+1/2,0,k}^{n}}{2\Delta y}\right)\end{aligned} \quad (2\text{-}44b)$$

$$\begin{aligned}-\frac{1}{c}\frac{\partial}{\partial t}E_x\,|_{i+1/2,1/2,k}^{n+1/2}&=-\frac{1}{c}\left(\frac{E_x\,|_{i+1/2,1/2,k}^{n+1}-E_x\,|_{i+1/2,1/2,k}^{n}}{\Delta t}\right)\\&=-\frac{1}{c\Delta t}\left(\frac{E_x\,|_{i+1/2,1,k}^{n+1}+E_x\,|_{i+1/2,0,k}^{n+1}}{2}-\frac{E_x\,|_{i+1/2,1,k}^{n}+E_x\,|_{i+1/2,0,k}^{n}}{2}\right)\end{aligned} \quad (2\text{-}44c)$$

This gives the boundary condition for E_x on the y=0 boundary:

$$E_x\,|^{n+1}_{i+1/2,0,k} = E_x\,|^{n}_{i+1/2,1,k} + \left(\frac{c\Delta t - \Delta y}{c\Delta t + \Delta y}\right)\left(E_x\,|^{n+1}_{i+1/2,1,k} - E_x\,|^{n}_{i+1/2,0,k}\right) \tag{2-45a}$$

Mur's first boundaries conditions of other electric field components can be derived similarly. They are listed below.

Boundary condition for E_z on the y=0 boundary is:

$$E_z\,|^{n+1}_{i,0,k+1/2} = E_x\,|^{n}_{i,1,k+1/2} + \left(\frac{c\Delta t - \Delta y}{c\Delta t + \Delta y}\right)\left(E_z\,|^{n+1}_{i,1,k+1/2} - E_z\,|^{n}_{i,0,k+1/2}\right) \tag{2-45b}$$

Boundary condition for E_x on the y=ny boundary is:

$$E_x\,|^{n+1}_{i+1/2,ny,k} = E_x\,|^{n}_{i+1/2,ny-1,k} + \left(\frac{c\Delta t - \Delta y}{c\Delta t + \Delta y}\right)\left(E_x\,|^{n+1}_{i+1/2,ny-1,k} - E_x\,|^{n}_{i+1/2,ny,k}\right) \tag{2-45c}$$

Boundary condition for E_z on the y=ny boundary is:

$$E_z\,|^{n+1}_{i,ny,k+1/2} = E_x\,|^{n}_{i,ny-1,k+1/2} + \left(\frac{c\Delta t - \Delta y}{c\Delta t + \Delta y}\right)\left(E_z\,|^{n+1}_{i,ny-1,k+1/2} - E_z\,|^{n}_{i,ny,k+1/2}\right) \tag{2-45d}$$

Dielectric-Dielectric Interface

If there are more than one materials in the simulation domain, from the Maxwell's equations, the tangential component of the electric field and the normal component of the magnetic flux density must be continuous at the these interfaces. This is automatically satisfied with the use of Yee's cell in our FDTD scheme as we mentioned in section 2.3.2. The reason is discussed below.

Considering the $E_x\,|_{i+1/2,j,k}$ in the middle of four Yee's cells with different permittivity and conductivities, as illustrated in Figure 13. Loop C is the path used for the integrated form of Maxwell's equation. The magnetic field pointing out in the middle of the interface of each cell goes exactly through loop C.

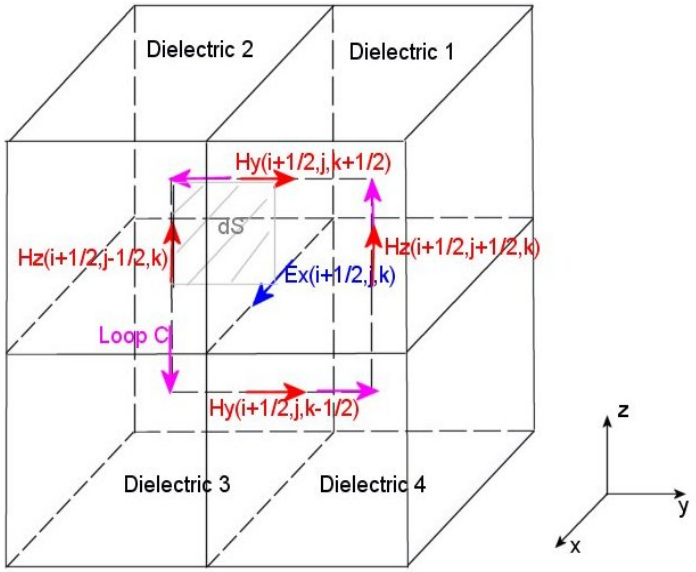

Figure 13 Dielectric-Dielectric Interface Implementation.

The integrated Maxwell's equation along loop C is:

$$\sum_{i=1}^{4}\left(\iint\left(\varepsilon_i\frac{\partial}{\partial t}\vec{E}+\sigma_i\vec{E}\right)\bullet d\vec{s}\right)=\sum_{i=1}^{4}\left(\oint_{C_i}\vec{H}\bullet d\vec{l}\right) \tag{2-46}$$

Applying the central-difference equations to the above equation yields:

$$\begin{aligned}
&\left(\varepsilon_1\frac{E_x|_{i+1/2,j,k}^{n+1}-E_x|_{i+1/2,j,k}^{n}}{\Delta t}+\sigma_1 E_x|_{i+1/2,j,k}^{n+1}+E_x|_{i+1/2,j,k}^{n}\right)S_1\\
&+\left(\varepsilon_2\frac{E_x|_{i+1/2,j,k}^{n+1}-E_x|_{i+1/2,j,k}^{n}}{\Delta t}+\sigma_2 E_x|_{i+1/2,j,k}^{n+1}+E_x|_{i+1/2,j,k}^{n}\right)S_2\\
&+\left(\varepsilon_3\frac{E_x|_{i+1/2,j,k}^{n+1}-E_x|_{i+1/2,j,k}^{n}}{\Delta t}+\sigma_3 E_x|_{i+1/2,j,k}^{n+1}+E_x|_{i+1/2,j,k}^{n}\right)S_3\\
&+\left(\varepsilon_4\frac{E_x|_{i+1/2,j,k}^{n+1}-E_x|_{i+1/2,j,k}^{n}}{\Delta t}+\sigma_4 E_x|_{i+1/2,j,k}^{n+1}+E_x|_{i+1/2,j,k}^{n}\right)S_4=\\
&\left(H_z|_{i+1/2,j+1/2,k}^{n+1/2}-H_z|_{i+1/2,j-1/2,k}^{n+1/2}\right)\Delta z+\left(-H_y|_{i+1/2,j,k+1/2}^{n+1/2}+H_y|_{i+1/2,j,k-1/2}^{n+1/2}\right)\Delta y
\end{aligned} \tag{2-47}$$

Here, $\varepsilon_1 = \varepsilon_2 = \varepsilon_3 = \varepsilon_4 = \varepsilon_{i+1/2,j,k}$, $\sigma_1 = \sigma_2 = \sigma_3 = \sigma_4 = \sigma_{i+1/2,j,k}$. For uniform cells, $S_1 = S_2 = S_3 = S_4 = \frac{\Delta z}{2} \cdot \frac{\Delta y}{2} = \frac{\Delta y \Delta z}{4}$. After combining the coefficients of the same terms together, we have

$$E_x\,|_{i+1/2,j,k}^{n+1} = \left(\frac{1 - \frac{\sigma_{i+1/2,j,k}\Delta t}{2\varepsilon_{i+1/2,j,k}}}{1 + \frac{\sigma_{i+1/2,j,k}\Delta t}{2\varepsilon_{i+1/2,j,k}}} \right) E_x\,|_{i+1/2,j,k}^{n} + \left(\frac{\frac{\Delta t}{\varepsilon_{i+1/2,j,k}}}{1 + \frac{\sigma_{i+1/2,j,k}\Delta t}{2\varepsilon_{i+1/2,j,k}}} \right) \left(\frac{H_z\,|_{i+1/2,j+1/2,k}^{n+1/2} - H_z\,|_{i+1/2,j-1/2,k}^{n+1/2}}{\Delta y} - \frac{H_y\,|_{i+1/2,j,k+1/2}^{n+1/2} - H_y\,|_{i+1/2,j,k-1/2}^{n+1/2}}{\Delta z} \right)$$

(2-48)

(2-48) the same as (2-23). This tells us if we define the permittivity and conductivity on the edge of each cell, the boundary condition on dielectric discontinuity is automatically satisfied in FDTD algorithm. If the permittivity and the conductivity are defined in the center of each cell, instead on the edge, then the equivalent permittivity and the conductivity on the edge is the average of those properties of the four adjacent cells that include this edge.

The permeability of all the materials in our problem is assumed to be the same as in free space. Therefore, there is no permeability discontinuity in our simulation. However, it can be proven in a similar way that our FDTD formulas will guarantee the field continuity at the boundary of materials with different permeability.

2.5 Summary

In this chapter, we reviewed the numerical methods used in interconnect analysis and the Finite-Difference Time-Domain (FD-TD) method. A standard flow chart of this conventional algorithm is introduced. Important numerical factors that strongly impact the stability and the accuracy of the algorithm, such as the choice of

cell size, the numerical stability, dispersion properties and boundary conditions are discussed in detail. The conventional FD-TD algorithm is the ancestor of the Alternate-Direction-Implicit Finite-Difference Time-Domain (ADI-FDTD) method, which will be introduced in the next chapter.

Chapter 3: ADI-FDTD Method

3.1 Background of the ADI-FDTD Method

We have learned from Chapter 2 that the very simple FDTD method can model various problems. However, in real problems, the distance scale over which the key physical processes or the material/structural properties must be resolved can range over several orders of magnitude. FDTD is limited to electrically small structure problems. The constraints stay in two folds: the grid size must be small enough in comparison with the shortest wave length (the shortest wave length represents the highest frequency component in the modeling problem.) and the time step must be small enough to satisfy the Courant stability condition. FDTD is yet to be a computationally efficient method.

To circumvent the Courant stability condition, various schemes of hybrid FDTD algorithm or higher order FDTD techniques have been presented. The hybrid FDTD method first calculates the problem region with coarse grids, recording the data on the interface of the region where we care more about the details. Then, we use these data on the interface as the boundary and use local mesh cells (sub grids or sub cells) to calculate the local field again and get the more accurate solution in the local region. In this method, we have to use the FDTD twice for the same problem. Considering that FDTD is a time iteration method, the hybrid FDTD method is less efficient. Also, the non-uniform cells will increase the truncation error of the finite-difference approximation at the boundary of two domains whose cell sizes differ. This results in a significant calculation error in some problems [36]. Higher order

FDTD techniques use higher order Taylor's expansions (instead of the standard second order accurate form) to discretize the partial differential equations. This can reduce the numerical dispersion [34]. For example, a much coarser grid can be used in the fourth-order accurate spatial central difference form to obtain less dispersion than the lower order FDTD with finer grids. However, calculating the fourth-order difference is very difficult when there is more than one material in the computation region, which is true for almost all real physical problems. Also, the fourth-order FDTD has slightly degraded the Courant stability conditions. Thus the higher order FDTD is not a perfect solution to the space-time restrictions either [34].

Meanwhile, other time-domain methods have been investigated. Krumpholz and Katehi proposed the Multiresolution Time-Domain method (MRTD) to relax the constraint on grid size [37]. The spatial discretization resolution can reach as low as two grid points per wavelength, and still provide tolerable numerical dispersion. Liu has proposed the pseudo spectral time-domain (PSTD) method [38] which uses the fast Fourier transform (FFT) to express spatial derivatives. The PSTD method can also provide high accuracy with two grid points per wavelength. However, in both methods, the Courant stability condition still has to be satisfied. Moreover, in MRTD, the time-to-spatial step ratio is five times less than that of conventional FDTD [37][39]. The stability condition becomes more stringent.

There has not been many attempts to relax or to remove the famous Courant stability condition. Implicit methods may eliminate the Courant condition induced in the explicit FDTD method. Unfortunately, a fully implicit scheme requires the solution of a large linear system of equations representing the full volume

discretization at each time step. Among these implicit techniques, the Alternating-direction Implicit (ADI) method is widely used in solving fluid mechanics and heat transfer problems, which results in various unconditionally stable finite-difference formulations for parabolic questions since it was introduced in the mid 1950's [40]-[41]. In 1984, the alternating-direction-implicit (ADI) technique was first used on Yee's grid to formulate an implicit FDTD scheme by Holland [39]. In that work, the finite-difference operator for 3D solution of Maxwell's equations was factored into three operators with each operator being performed in respect to the Cartesian coordinate directions. In each FDTD iteration cycle, three implicit substep computations were required. It was never found to be completely stable without adding significant dielectric loss. In 1999, the ADI method was applied on Yee's staggered grid in a 2D-TE wave problem [20]. The method is named the ADI-FDTD method. It shows great success in removing the Courant stability constraint and the selection of the time step used in this ADI-FDTD method only depends on problem accuracy [20].

3-D ADI-FDTD was also developed both in the Cartesian coordinates and in the cylindrical coordinates [42]. Various boundary condition implementations have been applied on the ADI-FDTD method as well [40].

3.2 ADI-FDTD Formulas and Flowchart

We will present the conventional ADI-FDTD method in this section. The ADI-FDTD method comes directly from the conventional second order accurate FDTD method based on Yee's cell. Because we are interested in on-chip interconnect problems, the conductivity should not be neglected. This means σ in Maxwell's

equations is not zero. However, the magnetic loss is not important and we can assume $\rho' = 0$.

We start by deriving the ADI-FDTD from the FDTD method (2-18), (2-19). In FDTD method, we compute the field marching from time step *n* to *n+1* in an explicit way. However, in ADI-FDTD method, we will break this one time step into two sub time steps: the first step is from *n* to *n+1/2* and the second step is from *n+1/2* to *n+1*. In the other words, we will make the finite differences centered at *n+1/4* in the first step and *n+3/4* in the second step. In the first half-step, the first partial derivative on the right hand side of (2-19) is replaced with an implicit difference approximation at the future *n+1/2* time step while the second partial derivative on the right hand side is replaced with an explicit finite difference approximation of the known values at the previous *n* time step. In the second half-step, the second partial derivative on the right hand side of (2-19) is replaced with an implicit difference approximation at the future *n+1* time step while the first partial derivative on the right hand side is replaced with an explicit finite difference approximation of the known values at the previous *n+1/2* time step. For example, for the partial differential equation of x component of the electric field:

$$\frac{\partial E_x}{\partial t} + \frac{\sigma}{\varepsilon} E_x = \frac{1}{\varepsilon}\left(\frac{\partial H_z}{\partial y} - \frac{\partial H_y}{\partial z} \right) \tag{3-1}$$

In the first half-step:

$$\varepsilon \frac{\partial E_x}{\partial t} |^{n+1/4} + \sigma E_x |^{n+1/4} = \frac{\partial H_z}{\partial y} |^{n+1/2} - \frac{\partial H_y}{\partial z} |^{n} \tag{3-2a}$$

In the second half-step:

$$\varepsilon \frac{\partial E_x}{\partial t} |^{n+3/4} + \sigma E_x |^{n+3/4} = \frac{\partial H_z}{\partial y} |^{n+1/2} - \frac{\partial H_y}{\partial z} |^{n+1} \tag{3-2b}$$

The corresponding central difference form is

$$\left(\begin{array}{l}\varepsilon_{i+1/2,j,k}\dfrac{E_x\,|^{n+1/2}_{i+1/2,j,k}-E_x\,|^{n}_{i+1/2,j,k}}{\Delta t/2}\\ +\sigma_{i+1/2,j,k}\dfrac{E_x\,|^{n+1/2}_{i+1/2,j,k}+E_x\,|^{n}_{i+1/2,j,k}}{2}\end{array}\right)=\left(\begin{array}{l}\dfrac{H_z\,|^{n+1/2}_{i+1/2,j+1/2,k}-H_z\,|^{n+1/2}_{i+1/2,j-1/2,k}}{\Delta y}\\ -\dfrac{H_y\,|^{n}_{i+1/2,j,k+1/2}-H_y\,|^{n}_{i+1/2,j,k-1/2}}{\Delta z}\end{array}\right) \tag{3-3a}$$

$$\left(\begin{array}{l}\varepsilon_{i+1/2,j,k}\dfrac{E_x\,|^{n+1}_{i+1/2,j,k}-E_x\,|^{n+1/2}_{i+1/2,j,k}}{\Delta t/2}\\ +\sigma_{i+1/2,j,k}\dfrac{E_x\,|^{n+1}_{i+1/2,j,k}+E_x\,|^{n+1/2}_{i+1/2,j,k}}{2}\end{array}\right)=\left(\begin{array}{l}\dfrac{H_z\,|^{n+1/2}_{i+1/2,j+1/2,k}-H_z\,|^{n+1/2}_{i+1/2,j-1/2,k}}{\Delta y}\\ -\dfrac{H_y\,|^{n+1}_{i+1/2,j,k+1/2}-H_y\,|^{n+1}_{i+1/2,j,k-1/2}}{\Delta z}\end{array}\right) \tag{3-3b}$$

We will perform this on all six scalar Maxwell's differential equations. The summary of the equations is shown below.

Step 1

$$\left(\begin{array}{l}\varepsilon_{i+1/2,j,k}\dfrac{E_x\,|^{n+1/2}_{i+1/2,j,k}-E_x\,|^{n}_{i+1/2,j,k}}{\Delta t/2}\\ +\sigma_{i+1/2,j,k}\dfrac{E_x\,|^{n+1/2}_{i+1/2,j,k}+E_x\,|^{n}_{i+1/2,j,k}}{2}\end{array}\right)=\left(\begin{array}{l}\dfrac{H_z\,|^{n+1/2}_{i+1/2,j+1/2,k}-H_z\,|^{n+1/2}_{i+1/2,j-1/2,k}}{\Delta y}\\ -\dfrac{H_y\,|^{n}_{i+1/2,j,k+1/2}-H_y\,|^{n}_{i+1/2,j,k-1/2}}{\Delta z}\end{array}\right) \tag{3-4a}$$

$$\left(\begin{array}{l}\varepsilon_{i,j+1/2,k}\dfrac{E_y\,|^{n+1/2}_{i,j+1/2,k}-E_y\,|^{n}_{i,j+1/2,k}}{\Delta t/2}\\ +\sigma_{i,j+1/2,k}\dfrac{E_y\,|^{n+1/2}_{i,j+1/2,k}+E_y\,|^{n}_{i,j+1/2,k}}{2}\end{array}\right)=\left(\begin{array}{l}\dfrac{H_x\,|^{n+1/2}_{i,j+1/2,k+1/2}-H_x\,|^{n+1/2}_{i,j+1/2,k-1/2}}{\Delta z}\\ -\dfrac{H_z\,|^{n}_{i+1/2,j+1/2,k}-H_z\,|^{n}_{i-1/2,j+1/2,k}}{\Delta x}\end{array}\right) \tag{3-4b}$$

$$\left(\begin{array}{l}\varepsilon_{i,j,k+1/2}\dfrac{E_z\,|^{n+1/2}_{i,j,k+1/2}-E_z\,|^{n}_{i,j,k+1/2}}{\Delta t/2}\\ +\sigma_{i,j,k+1/2}\dfrac{E_z\,|^{n+1/2}_{i,j,k+1/2}+E_z\,|^{n}_{i,j,k+1/2}}{2}\end{array}\right)=\left(\begin{array}{l}\dfrac{H_y\,|^{n+1/2}_{i+1/2,j,k+1/2}-H_y\,|^{n+1/2}_{i-1/2,j,k+1/2}}{\Delta x}\\ -\dfrac{H_x\,|^{n}_{i,j+1/2,k+1/2}-H_x\,|^{n}_{i,j-1/2,k+1/2}}{\Delta y}\end{array}\right) \tag{3-4c}$$

$$\mu_{i,j+1/2,k+1/2}\left(\frac{H_x\,|^{n+1/2}_{i,j+1/2,k+1/2}-H_x\,|^{n}_{i,j+1/2,k+1/2}}{\Delta t/2}\right)=\left(\begin{array}{l}\dfrac{E_y\,|^{n+1/2}_{i,j+1/2,k+1}-E_y\,|^{n+1/2}_{i,j+1/2,k}}{\Delta z}\\ -\dfrac{E_z\,|^{n}_{i,j+1,k+1/2}-E_z\,|^{n}_{i,j,k+1/2}}{\Delta y}\end{array}\right) \tag{3-4d}$$

$$\mu_{i+1/2,j,k+1/2}\left(\frac{H_y\,|_{i+1/2,j,k+1/2}^{n+1/2}-H_y\,|_{i+1/2,j,k+1/2}^{n}}{\Delta t/2}\right)=\begin{pmatrix}\dfrac{E_z\,|_{i+1,j,k+1/2}^{n+1/2}-E_z\,|_{i,j,k+1/2}^{n+1/2}}{\Delta x}\\ -\dfrac{E_x\,|_{i+1/2,j,k+1}^{n}-E_x\,|_{i+1/2,j,k}^{n}}{\Delta z}\end{pmatrix} \tag{3-4e}$$

$$\mu_{i+1/2,j+1/2,k}\left(\frac{H_z\,|_{i+1/2,j+1/2,k}^{n+1/2}-H_z\,|_{i+1/2,j+1/2,k}^{n}}{\Delta t/2}\right)=\begin{pmatrix}\dfrac{E_x\,|_{i+1/2,j+1,k}^{n+1/2}-E_x\,|_{i+1/2,j,k}^{n+1/2}}{\Delta y}\\ -\dfrac{E_y\,|_{i+1,j+1/2,k}^{n}-E_y\,|_{i,j+1/2,k}^{n}}{\Delta x}\end{pmatrix} \tag{3-4f}$$

Step 2

$$\begin{pmatrix}\varepsilon_{i+1/2,j,k}\dfrac{E_x\,|_{i+1/2,j,k}^{n+1}-E_x\,|_{i+1/2,j,k}^{n+1/2}}{\Delta t/2}\\ +\sigma_{i+1/2,j,k}\dfrac{E_x\,|_{i+1/2,j,k}^{n+1}+E_x\,|_{i+1/2,j,k}^{n+1/2}}{2}\end{pmatrix}=\begin{pmatrix}\dfrac{H_z\,|_{i+1/2,j+1/2,k}^{n+1/2}-H_z\,|_{i+1/2,j-1/2,k}^{n+1/2}}{\Delta y}\\ -\dfrac{H_y\,|_{i+1/2,j,k+1/2}^{n+1}-H_y\,|_{i+1/2,j,k-1/2}^{n+1}}{\Delta z}\end{pmatrix} \tag{3-5a}$$

$$\begin{pmatrix}\varepsilon_{i,j+1/2,k}\dfrac{E_y\,|_{i,j+1/2,k}^{n+1}-E_y\,|_{i,j+1/2,k}^{n+1/2}}{\Delta t/2}\\ +\sigma_{i,j+1/2,k}\dfrac{E_y\,|_{i,j+1/2,k}^{n+1}+E_y\,|_{i,j+1/2,k}^{n+1/2}}{2}\end{pmatrix}=\begin{pmatrix}\dfrac{H_x\,|_{i,j+1/2,k+1/2}^{n+1/2}-H_x\,|_{i,j+1/2,k-1/2}^{n+1/2}}{\Delta z}\\ -\dfrac{H_z\,|_{i+1/2,j+1/2,k}^{n+1}-H_z\,|_{i-1/2,j+1/2,k}^{n+1}}{\Delta x}\end{pmatrix} \tag{3-5b}$$

$$\begin{pmatrix}\varepsilon_{i,j,k+1/2}\dfrac{E_z\,|_{i,j,k+1/2}^{n+1}-E_z\,|_{i,j,k+1/2}^{n+1/2}}{\Delta t/2}\\ +\sigma_{i,j,k+1/2}\dfrac{E_z\,|_{i,j,k+1/2}^{n}+E_z\,|_{i,j,k+1/2}^{n+1/2}}{2}\end{pmatrix}=\begin{pmatrix}\dfrac{H_y\,|_{i+1/2,j,k+1/2}^{n+1/2}-H_y\,|_{i-1/2,j,k+1/2}^{n+1/2}}{\Delta x}\\ -\dfrac{H_x\,|_{i,j+1/2,k+1/2}^{n+1}-H_x\,|_{i,j-1/2,k+1/2}^{n+1}}{\Delta y}\end{pmatrix} \tag{3-5c}$$

$$\mu_{i,j+1/2,k+1/2}\left(\frac{H_x\,|_{i,j+1/2,k+1/2}^{n+1}-H_x\,|_{i,j+1/2,k+1/2}^{n+1/2}}{\Delta t/2}\right)=\begin{pmatrix}\dfrac{E_y\,|_{i,j+1/2,k+1}^{n+1/2}-E_y\,|_{i,j+1/2,k}^{n+1/2}}{\Delta z}\\ -\dfrac{E_z\,|_{i,j+1,k+1/2}^{n+1}-E_z\,|_{i,j,k+1/2}^{n+1}}{\Delta y}\end{pmatrix} \tag{3-5d}$$

$$\mu_{i+1/2,j,k+1/2}\left(\frac{H_y\,|_{i+1/2,j,k+1/2}^{n+1}-H_y\,|_{i+1/2,j,k+1/2}^{n+1/2}}{\Delta t/2}\right)=\begin{pmatrix}\dfrac{E_z\,|_{i+1,j,k+1/2}^{n+1/2}-E_z\,|_{i,j,k+1/2}^{n+1/2}}{\Delta x}\\ -\dfrac{E_x\,|_{i+1/2,j,k+1}^{n+1}-E_x\,|_{i+1/2,j,k}^{n+1}}{\Delta z}\end{pmatrix} \tag{3-5e}$$

$$\mu_{i+1/2,j+1/2,k}\left(\frac{H_z\,|_{i+1/2,j+1/2,k}^{n+1}-H_z\,|_{i+1/2,j+1/2,k}^{n+1/2}}{\Delta t/2}\right)=\begin{pmatrix}\dfrac{E_x\,|_{i+1/2,j+1,k}^{n+1/2}-E_x\,|_{i+1/2,j,k}^{n+1/2}}{\Delta y}\\ -\dfrac{E_y\,|_{i+1,j+1/2,k}^{n+1}-E_y\,|_{i,j+1/2,k}^{n+1}}{\Delta x}\end{pmatrix} \tag{3-5f}$$

It is worth noting that the choice of implicit and explicit difference approximation in each sub time step is not unique. For example, in the first half-step, we can replace the second partial derivative on the right hand side with an implicit difference approximation at the future *n+1/2* time step while the first partial derivative on the right hand side of (2-19) is replaced with explicit finite difference approximation using known values at the previous *n* time step. In the second half-step, the first partial derivative on the right hand side of (2-19) is replaced with an implicit difference approximation at the future *n+1* time step while the second partial derivative on the right hand side are replaced with an explicit finite difference approximation from known values at the previous *n+1/2* time step. In this way, we will get a set of iterations different from (3-4) and (3-5), but all the physical and numerical characteristics of these two iterations are similar. In this thesis, our discussion will focus on the iterations shown in (3-4) and (3-5).

In the first half-step, in order to find the E field at the *n+1/2* time step, we need to solve (3-4a). Substituting (3-4f) in (3-4a) allows cancellation of the unknown H_z terms at the future *n+1/2* time step. After reorganizing the terms, we have:

$$\left(\begin{array}{l}\left(\left(\dfrac{-\Delta t^2}{4\varepsilon_{i+1/2,j,k}\mu_{i+1/2,j+1/2,k}\Delta y^2}\right)E_x\,|^{n+1/2}_{i+1/2,j+1,k}\right.\\ +\left(1+\dfrac{\sigma_{i+1/2,j,k}\Delta t}{2\varepsilon_{i+1/2,j,k}}+\dfrac{\Delta t^2}{4\varepsilon_{i+1/2,j,k}\mu_{i+1/2,j+1/2,k}\Delta y^2}+\dfrac{\Delta t^2}{4\varepsilon_{i+1/2,j,k}\mu_{i+1/2,j-1/2,k}\Delta y^2}\right)E_x\,|^{n+1/2}_{i+1/2,j,k}\\ \left.+\left(\dfrac{-\Delta t^2}{4\varepsilon_{i+1/2,j,k}\mu_{i+1/2,j-1/2,k}\Delta y^2}\right)E_x\,|^{n+1/2}_{i+1/2,j-1,k}\right)=\\ \left(E_x\,|^{n}_{i+1/2,j,k}+\left(\dfrac{-\Delta t^2}{4\varepsilon_{i+1/2,j,k}\mu_{i+1/2,j+1/2,k}\Delta x\Delta y}\right)\left(E_y\,|^{n}_{i+1,j+1/2,k}-E_y\,|^{n}_{i,j+1/2,k}\right)\right.\\ +\left(\dfrac{\Delta t^2}{4\varepsilon_{i+1/2,j,k}\mu_{i+1/2,j-1/2,k}\Delta x\Delta y}\right)\left(E_y\,|^{n}_{i+1,j-1/2,k}-E_y\,|^{n}_{i,j-1/2,k}\right)\\ \left.+\left(\dfrac{\Delta t}{2\varepsilon_{i+1/2,j,k}\Delta y}\right)\left(H_z\,|^{n}_{i+1/2,j+1/2,k}-H_z\,|^{n}_{i+1/2,j-1/2,k}\right)-\left(\dfrac{\Delta t}{2\varepsilon_{i+1/2,j,k}\Delta z}\right)\left(H_y\,|^{n}_{i+1/2,j,k+1/2}-H_y\,|^{n}_{i+1/2,j,k-1/2}\right)\right)\end{array}\right.$$

(3-6a)

The left hand side terms in (3-6a) are unknown E_x field vectors along the y direction. The right hand side terms in (3-6a) are the known field components calculated from and stored in the previous half-time-step. Now, the E_x field vectors along the y direction can be calculated by (3-6a).

Similarly, substituting (3-4e) into (3-4b), (3-4d) into (3-4c), we have:

$$\left(\begin{array}{l}\left(\left(\dfrac{-\Delta t^2}{4\varepsilon_{i,j+1/2,k}\mu_{i,j+1/2,k+1/2}\Delta z^2}\right)E_y\,|^{n+1/2}_{i,j+1/2,k+1}\right.\\ +\left(1+\dfrac{\sigma_{i,j+1/2,k}\Delta t}{2\varepsilon_{i,j+1/2,k}}+\dfrac{\Delta t^2}{4\varepsilon_{i,j+1/2,k}\mu_{i,j+1/2,k+1/2}\Delta z^2}+\dfrac{\Delta t^2}{4\varepsilon_{i,j+1/2,k}\mu_{i,j+1/2,k-1/2}\Delta z^2}\right)E_y\,|^{n+1/2}_{i,j+1/2,k}\\ \left.+\left(\dfrac{-\Delta t^2}{4\varepsilon_{i,j+1/2,k}\mu_{i,j+1/2,k-1/2}\Delta z^2}\right)E_y\,|^{n+1/2}_{i,j+1/2,k-1}\right)=\\ \left(E_y\,|^{n}_{i,j+1/2,k}+\left(\dfrac{-\Delta t^2}{4\varepsilon_{i,j+1/2,k}\mu_{i,j+1/2,k+1/2}\Delta y\Delta z}\right)\left(E_z\,|^{n}_{i,j+1,k+1/2}-E_z\,|^{n}_{i,j,k+1/2}\right)\right.\\ +\left(\dfrac{\Delta t^2}{4\varepsilon_{i,j+1/2,k}\mu_{i,j+1/2,k-1/2}\Delta y\Delta z}\right)\left(E_z\,|^{n}_{i,j+1,k-1/2}-E_z\,|^{n}_{i,j,k-1/2}\right)\\ \left.+\left(\dfrac{\Delta t}{2\varepsilon_{i,j+1/2,k}\Delta z}\right)\left(H_x\,|^{n}_{i,j+1/2,k+1/2}-H_x\,|^{n}_{i,j+1/2,k-1/2}\right)-\left(\dfrac{\Delta t}{2\varepsilon_{i,j+1/2,k}\Delta x}\right)\left(H_z\,|^{n}_{i+1/2,j+1/2,k}-H_z\,|^{n}_{i-1/2,j+1/2,k}\right)\right)\end{array}\right.$$

(3-6b)

$$\left(\begin{array}{l}\left(\dfrac{-\Delta t^2}{4\varepsilon_{i,j,k+1/2}\mu_{i+1/2,j,k+1/2}\Delta x^2}\right)E_z\,|_{i+1,j,k+1/2}^{n+1/2}\\ +\left(1+\dfrac{\sigma_{i,j,k+1/2}\Delta t}{2\varepsilon_{i,j,k+1/2}}+\dfrac{\Delta t^2}{4\varepsilon_{i,j,k+1/2}\mu_{i+1/2,j,k+1/2}\Delta x^2}+\dfrac{\Delta t^2}{4\varepsilon_{i,j,k+1/2}\mu_{i-1/2,j,k+1/2}\Delta x^2}\right)E_z\,|_{i,j,k+1/2}^{n+1/2}=\\ +\left(\dfrac{-\Delta t^2}{4\varepsilon_{i,j,k+1/2}\mu_{i-1/2,j,k+1/2}\Delta x^2}\right)E_z\,|_{i-1,j,k+1/2}^{n+1/2}\end{array}\right)$$

$$\left(\begin{array}{l}E_z\,|_{i,j,k+1/2}^{n}+\left(\dfrac{-\Delta t^2}{4\varepsilon_{i,j,k+1/2}\mu_{i+1/2,j,k+1/2}\Delta x\Delta z}\right)\left(E_x\,|_{i+1/2,j,k+1}^{n}-E_x\,|_{i+1/2,j,k}^{n}\right)\\ +\left(\dfrac{\Delta t^2}{4\varepsilon_{i,j,k+1/2}\mu_{i-1/2,j,k+1/2}\Delta x\Delta z}\right)\left(E_x\,|_{i-1/2,j,k+1}^{n}-E_x\,|_{i-1/2,j,k}^{n}\right)\\ +\left(\dfrac{\Delta t}{2\varepsilon_{i,j,k+1/2}\Delta x}\right)\left(H_y\,|_{i+1/2,j,k+1/2}^{n}-H_y\,|_{i-1/2,j,k+1/2}^{n}\right)-\left(\dfrac{\Delta t}{2\varepsilon_{i,j,k+1/2}\Delta y}\right)\left(H_x\,|_{i,j+1/2,k+1/2}^{n}-H_x\,|_{i,j-1/2,k+1/2}^{n}\right)\end{array}\right)$$

(3-6c)

The E_y field vectors along the z direction can be calculated by (3-6b) and the E_z field vectors along the x direction can be calculated by (3-6c). Then, we will use (3-4d) - (3-4f) to update the H field at the *n+1/2* time step explicitly.

Similarly, in the second half time step, after substituting (3-5d) - (3-5f) into (3-5a) - (3-5c) accordingly, we have:

$$\left(\begin{array}{l}\left(\dfrac{-\Delta t^2}{4\varepsilon_{i+1/2,j,k}\mu_{i+1/2,j,k+1/2}\Delta z^2}\right)E_x\,|_{i+1/2,j,k+1}^{n+1}\\ +\left(1+\dfrac{\sigma_{i+1/2,j,k}\Delta t}{2\varepsilon_{i+1/2,j,k}}+\dfrac{\Delta t^2}{4\varepsilon_{i+1/2,j,k}\mu_{i+1/2,j,k+1/2}\Delta z^2}+\dfrac{\Delta t^2}{4\varepsilon_{i+1/2,j,k}\mu_{i+1/2,j,k-1/2}\Delta z^2}\right)E_x\,|_{i+1/2,j,k}^{n+1}=\\ +\left(\dfrac{-\Delta t^2}{4\varepsilon_{i+1/2,j,k}\mu_{i+1/2,j,k-1/2}\Delta z^2}\right)E_x\,|_{i+1/2,j,k-1}^{n+1}\end{array}\right)$$

$$\left(\begin{array}{l}E_x\,|_{i+1/2,j,k}^{n+1/2}+\left(\dfrac{-\Delta t^2}{4\varepsilon_{i+1/2,j,k}\mu_{i+1/2,j,k+1/2}\Delta x\Delta z}\right)\left(E_z\,|_{i+1,j,k+1/2}^{n+1/2}-E_z\,|_{i,j,k+1/2}^{n+1/2}\right)\\ +\left(\dfrac{\Delta t^2}{4\varepsilon_{i+1/2,j,k}\mu_{i+1/2,j,k-1/2}\Delta x\Delta z}\right)\left(E_z\,|_{i+1,j,k-1/2}^{n+1/2}-E_z\,|_{i,j,k-1/2}^{n+1/2}\right)\\ +\left(\dfrac{\Delta t}{2\varepsilon_{i+1/2,j,k}\Delta y}\right)\left(H_z\,|_{i+1/2,j+1/2,k}^{n+1/2}-H_z\,|_{i+1/2,j-1/2,k}^{n+1/2}\right)-\left(\dfrac{\Delta t}{2\varepsilon_{i+1/2,j,k}\Delta z}\right)\left(H_y\,|_{i+1/2,j,k+1/2}^{n+1/2}-H_y\,|_{i+1/2,j,k-1/2}^{n+1/2}\right)\end{array}\right)$$

(3-7a)

$$
\begin{aligned}
&\left(\left(\frac{-\Delta t^2}{4\varepsilon_{i,j+1/2,k}\mu_{i+1/2,j+1/2,k}\Delta x^2}\right)E_y\,|_{i+1,j+1/2,k}^{n+1}\right.\\
&+\left(1+\frac{\sigma_{i,j+1/2,k}\Delta t}{2\varepsilon_{i,j+1/2,k}}+\frac{\Delta t^2}{4\varepsilon_{i,j+1/2,k}\mu_{i+1/2,j+1/2,k}\Delta x^2}+\frac{\Delta t^2}{4\varepsilon_{i,j+1/2,k}\mu_{i-1/2,j+1/2,k}\Delta x^2}\right)E_y\,|_{i,j+1/2,k}^{n+1}=\\
&\left.+\left(\frac{-\Delta t^2}{4\varepsilon_{i,j+1/2,k}\mu_{i-1/2,j+1/2,k}\Delta x^2}\right)E_y\,|_{i-1,j+1/2,k}^{n+1}\right)\\
&\left(E_y\,|_{i,j+1/2,k}^{n+1/2}+\left(\frac{-\Delta t^2}{4\varepsilon_{i,j+1/2,k}\mu_{i-1/2,j+1/2,k}\Delta x\Delta y}\right)\left(E_x\,|_{i-1/2,j+1,k}^{n+1/2}-E_x\,|_{i-1/2,j,k}^{n+1/2}\right)\right.\\
&+\left(\frac{\Delta t^2}{4\varepsilon_{i,j+1/2,k}\mu_{i+1/2,j+1/2,k}\Delta x\Delta y}\right)\left(E_x\,|_{i+1/2,j+1,k}^{n+1/2}-E_x\,|_{i+1/2,j,k}^{n+1/2}\right)\\
&\left.+\left(\frac{\Delta t}{2\varepsilon_{i,j+1/2,k}\Delta z}\right)\left(H_x\,|_{i,j+1/2,k+1/2}^{n+1/2}-H_x\,|_{i,j+1/2,k-1/2}^{n+1/2}\right)-\left(\frac{\Delta t}{2\varepsilon_{i,j+1/2,k}\Delta x}\right)\left(H_z\,|_{i+1/2,j+1/2,k}^{n+1/2}-H_z\,|_{i-1/2,j+1/2,k}^{n+1/2}\right)\right)
\end{aligned}
\tag{3-7b}
$$

$$
\begin{aligned}
&\left(\left(\frac{-\Delta t^2}{4\varepsilon_{i,j,k+1/2}\mu_{i,j+1/2,k+1/2}\Delta y^2}\right)E_z\,|_{i,j+1,k+1/2}^{n+1}\right.\\
&+\left(1+\frac{\sigma_{i,j,k+1/2}\Delta t}{2\varepsilon_{i,j,k+1/2}}+\frac{\Delta t^2}{4\varepsilon_{i,j,k+1/2}\mu_{i,j+1/2,k+1/2}\Delta y^2}+\frac{\Delta t^2}{4\varepsilon_{i,j,k+1/2}\mu_{i,j-1/2,k+1/2}\Delta y^2}\right)E_z\,|_{i,j,k+1/2}^{n+1}=\\
&\left.+\left(\frac{-\Delta t^2}{4\varepsilon_{i,j,k+1/2}\mu_{i,j-1/2,k+1/2}\Delta y^2}\right)E_z\,|_{i,j-1,k+1/2}^{n+1}\right)\\
&\left(E_z\,|_{i,j,k+1/2}^{n+1/2}+\left(\frac{-\Delta t^2}{4\varepsilon_{i,j,k+1/2}\mu_{i,j+1/2,k+1/2}\Delta y\Delta z}\right)\left(E_y\,|_{i,j+1/2,k+1}^{n+1/2}-E_y\,|_{i,j+1/2,k}^{n+1/2}\right)\right.\\
&+\left(\frac{\Delta t^2}{4\varepsilon_{i,j,k+1/2}\mu_{i,j-1/2,k+1/2}\Delta y\Delta z}\right)\left(E_y\,|_{i,j-1/2,k+1}^{n+1/2}-E_y\,|_{i,j-1/2,k}^{n+1/2}\right)\\
&\left.+\left(\frac{\Delta t}{2\varepsilon_{i,j,k+1/2}\Delta x}\right)\left(H_y\,|_{i+1/2,j,k+1/2}^{n+1/2}-H_y\,|_{i-1/2,j,k+1/2}^{n+1/2}\right)-\left(\frac{\Delta t}{2\varepsilon_{i,j,k+1/2}\Delta y}\right)\left(H_x\,|_{i,j+1/2,k+1/2}^{n+1/2}-H_x\,|_{i,j-1/2,k+1/2}^{n+1/2}\right)\right)
\end{aligned}
\tag{3-7c}
$$

Now, at the end of the $(n+1)$ time step, we can calculate the E_x field vectors along the z direction by (3-7a), the E_y field vectors along the x direction by (3-7b), and the E_z field vectors along the y direction by (3-7c). Then, we will update the H field at the $(n+1)$ time step with (3-5d)-(3-5f) explicitly. The above ADI-FDTD time-stepping process is summarized in the flowchart in Figure 14.

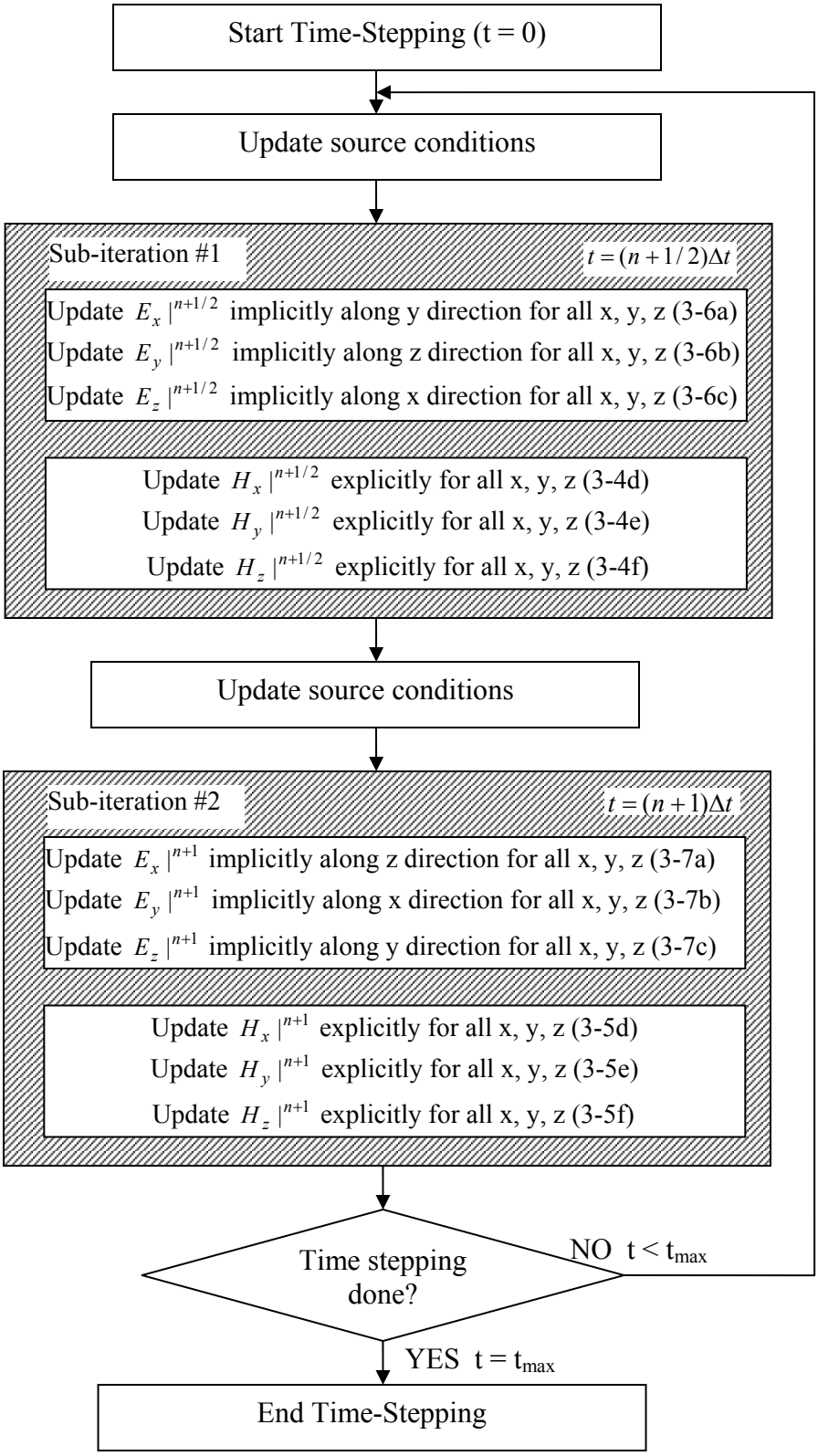

Figure 14 Flowchart of the ADI-FDTD time-stepping process [40]

3.3 ADI-FDTD Concerns

Similar to the FDTD algorithm, numerical stability and numerical dispersion are important fundamental characteristics of the ADI-FDTD method. According to numerical stability analysis, we will find the proper relationship between the grid size and the time step size. Through numerical dispersion analysis, we will further clarify the factors that impact the accuracy of the ADI-FDTD algorithm.

However, the analysis of the numerical stability and the numerical dispersion relationship is much more complicated than the conventional FDTD method. This is because in the ADI-FDTD method, we have introduced the sub time-step and therefore, the non-physical intermediate field components. The research of stability and numerical dispersion in the ADI-FDTD method is still an open problem in many aspects.

3.3.1 Cell size

Similar to the FDTD method, the first step in applying the ADI-FDTD method is to determine the proper cell size in the modeling problem.

FDTD algorithm could handle electrically small problems. In **electrically small problems**, the grid cell size that can effectively capture the transient wave propagating characteristics is much smaller than the minimum geometrical size of the component in the model.

ADI-FDTD is designed to simulate those problems with fine geometrical structure. The grid size is pinned to be much smaller than the grid size required by the wavelength. This is the **electrically large problem**. We will discuss the limitation of

time-step size in the next subsection, where we will also discuss the stability of the ADI-FDTD method.

The choice of cell size must satisfy two requirements simultaneously. First, it must be small enough to allow accurate results at the highest frequency of interest. Second, it must be able to resolve the finest geometrical structures of interest. As an additional requirement, the number of cells must not be too large in order to keep resource requirements manageable.

Similarly as in the FDTD method, people usually choose cell sizes smaller than $\frac{\lambda_u}{20}$ if computational resources allow, where λ_u is the shortest wavelength of interest. The reason for this will be covered in section 3.3.3.

3.3.2 Numerical Stability, Cell and Time Step Sizes

ADI-FDTD is announced to be stable for any time-step sizes. However, at certain time-step sizes, the numerical results are noise-like and no wave travels. Thus, the ADI-FDTD method does have time-step size limitations.

3.3.2.1 1D and 2D Stability Analysis using the von Neumann's method

The numerical stability analysis of the ADI-FDTD algorithm is first presented by Namiki when he introduced this algorithm in 1999 [20]. This analysis is performed in 2D ADI-FDTD scheme. Later on, Guilin Sun has performed the stability analysis based on the same method both in the 1-D and 2-D ADI-FDTD scheme [43]-[44].

We introduce amplification factor in the iteration. The recursive process is stable when the amplification factor is equal or smaller than the unit value.

We will use the 2-D TE wave equations as an example. The field solution is defined as:

$$\psi = \psi_0 \xi^n e^{j(\tilde{k}_x x + \tilde{k}_y y)} \tag{3-8a}$$

where $j = \sqrt{-1}$, $\tilde{k}_x$ and $\tilde{k}_y$ are numerical wave numbers. ξ is the amplification factor. For each field component, we have

$$E_x = \psi_A \xi_l^n e^{j(\tilde{k}_x x + \tilde{k}_y y)} \tag{3-8b}$$

$$E_y = \psi_B \xi_l^n e^{j(\tilde{k}_x x + \tilde{k}_y y)} \tag{3-8c}$$

$$H_z = \psi_B \xi_l^n e^{j(\tilde{k}_x x + \tilde{k}_y y)} \tag{3-8d}$$

$l = 1,2$, where $l = 1$ refers to the first half-time step, and $l = 2$ indicates the second half-time step. ψ is the amplitude of field components.

Substituting (3-8b)-(3-8d) into the first half-time step of the 2-D TE mode ADI-FDTD equations will yield:

$$\xi_1 = \frac{1 \pm j\sqrt{\left(1 + W_x^2\right)\left(1 + W_y^2\right) - 1}}{1 + W_x^2}, \tag{3-9a}$$

And substituting (3-8b)-(3-8d) into the second half-time step of the 2-D TE mode ADI-FDTD equations will yield:

$$\xi_2 = \frac{1 \pm j\sqrt{\left(1 + W_x^2\right)\left(1 + W_y^2\right) - 1}}{1 + W_y^2} \tag{3-9b}$$

Here $j = \sqrt{-1}$; Δt is the time step size; $W_x = \frac{c\Delta t}{\Delta x}\sin\left(\frac{\tilde{k}_x \Delta x}{2}\right)$, $W_y = \frac{c\Delta t}{\Delta y}\sin\left(\frac{\tilde{k}_y \Delta y}{2}\right)$; Δx, Δy are spatial meshing sizes along the x and y axes; $c = \frac{1}{\sqrt{\mu\varepsilon}}$ is the free space velocity; μ and ε are the permittivity and permeability of the material, respectively;

$\tilde{k}_x = \tilde{k}\cos\phi$, $\tilde{k}_y = \tilde{k}\sin\phi$, $\tilde{k} = \sqrt{\tilde{k}_x^2 + \tilde{k}_y^2}$ is the numerical wave phase constant; ϕ is the travel direction with respect to the positive x axis.

For convenience, we rewrite the (3-9) in the phasor form:

$$\xi_1 = \xi_{10} e^{\pm j\varphi_1} \tag{3-10a}$$

$$\xi_2 = \xi_{20} e^{\pm j\varphi_2} \tag{3-10b}$$

where

$$\xi_{10} = \frac{1}{\xi_{20}} = \sqrt{\frac{1+W_y^2}{1+W_x^2}}, \tag{3-10c}$$

$$\varphi_1 = \varphi_2 = \tan^{-1}\sqrt{\left(1+W_x^2\right)\left(1+W_y^2\right)-1}. \tag{3-10d}$$

Since $\xi = \xi_{10}\xi_{20} = 1$, for one complete update cycle (including two sub-time steps), the overall magnitude of the amplification factor is unity. This indicates that there is no growth or dissipation in the ADI-FDTD algorithm. Thus the ADI-FDTD recursive process is stable and nondissipative. A closer observation shows that the amplification factors in two substeps are reciprocals. The amplitudes of them are plotting in Figure 15 [43]. Similar to FDTD method, we introduce Courant number in ADI-FDTD algorithm:

$$CFL^{ADI-FDTD} = c\Delta t^{ADI-FDTD}\sqrt{\frac{1}{\Delta x^2}+\frac{1}{\Delta y^2}+\frac{1}{\Delta z^2}}. \tag{3-11a}$$

Recall that in Chapter 2, we defined the Courant number for the FDTD algorithm as $CFL = c\Delta t^{FDTD}\sqrt{1/\Delta x^2 + 1/\Delta y^2 + 1/\Delta z^2} \le 1$. If CFL is set to achieve minimum dispersion (According to Chapter two, minimum dispersion happens at CFL=1, where the time step reaches its maximum value.), we have:

$$CFL^{ADI-FDTD} = c\Delta t^{ADI-FDTD}\sqrt{\frac{1}{\Delta x^2}+\frac{1}{\Delta y^2}+\frac{1}{\Delta z^2}} = \frac{\Delta t^{ADI-FDTD}}{\Delta t_{\max}^{FDTD}} \tag{3-11b}$$

We can use (3-11b) to compare ADI-FDTD method and traditional FDTD method conveniently.

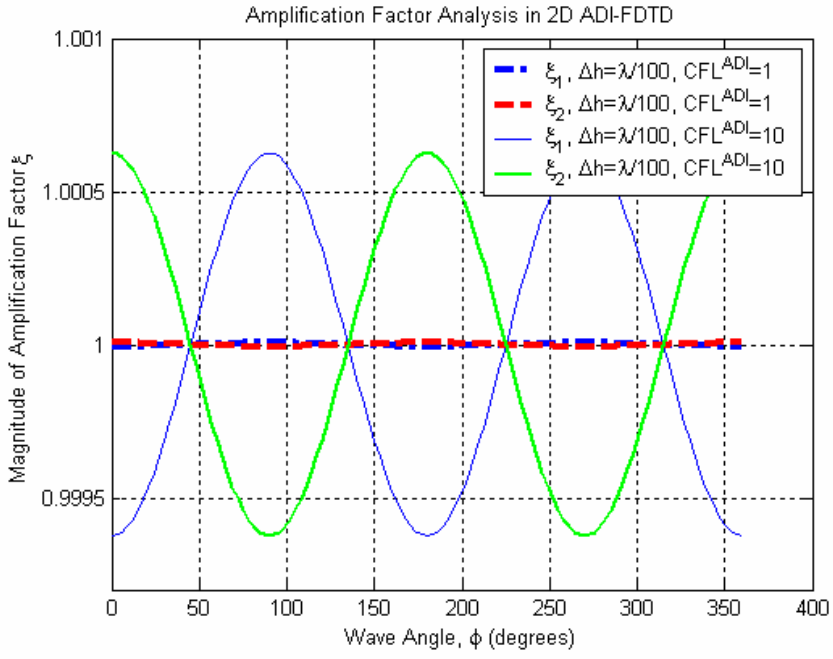

Figure 15 Magnitude of the amplification factor for Courant number equals 1 and 10 with 100 cells per wavelength [43].

Figure 15 tells us, when we use $\Delta t_{\max}^{FDTD}$ in ADI-FDTD (the optimized time step of FDTD), both amplification factors are close to one. The iteration is neither growing nor dissipating. Otherwise, in one sub-time step, the iteration is growing, and in the other sub-time step, the iteration is dissipating.

It has been pointed out that the numerical dissipation and growth in the ADI-FDTD sub time steps is the result of the unbalanced time splitting algorithm. Other investigation shows that in the balanced time splitting scheme of the Crank-Nicholson

method for the FDTD does not have the numerical growth or dissipation and it is not dissipative [45].

3.3.2.2 3D stability analysis with the amplification matrix method [46].

The stability analysis of the ADI-FDTD method is extended to 3-D system by Zheng with the amplification matrix method [47]. First, the two sub time-steps of recursive process in the ADI-FDTD are written in a compact matrix form (3-12):

Step1 (from the n th to the $(n+1/2)$ th time step)

$$M_1 X^{n+1/2} = P_1 X^n \tag{3-12a}$$

Step2 (from the $(n+1/2)$ th to the $(n+1)$ th time step)

$$M_2 X^{n+1} = P_2 X^{n+1/2} \tag{3-12b}$$

Here, $X^n = \left(E_x^n, E_y^n, E_z^n, H_x^n, H_y^n, H_z^n\right)^T$. M_1, M_2, P_1, P_2 are coefficient matrices with their elements related to values of spatial and temporal steps. Since they are all sparse matrices, (3-12a), and (3-12b) can be solved explicitly by taking the inverse of the sparse matrix. The result is:

$$X^{n+1} = \Lambda X^n \tag{3-12c}$$

where $\Lambda = M_2^{-1} P_2 M_1^{-1} P_1$.

System (3-12) is stable only if the norm of the error of the solution in (3-12) is bounded. It has been proven that this occurs if the spectral radius of the iteration matrix Λ is less or equal to unity, or the norm of the iteration matrix Λ is less or equal to a unity matrix.

First, we will assume the field components in Maxwell's equations in the spatial spectral domain is

$$E_x\,|^n_{i+1/2,j,k} = E^n_x e^{-j\left(\tilde{k}_x(i+1/2)\Delta x+\tilde{k}_y j\Delta y+\tilde{k}_z k\Delta z\right)} \tag{3-13a}$$

$$E_y\,|^n_{i,j+1/2,k} = E^n_y e^{-j\left(\tilde{k}_x(i)\Delta x+\tilde{k}_y (j+1/2)\Delta y+\tilde{k}_z k\Delta z\right)} \tag{3-13b}$$

$$E_z\,|^n_{i,j,k+1/2} = E^n_z e^{-j\left(\tilde{k}_x i\Delta x+\tilde{k}_y j\Delta y+\tilde{k}_z (k+1/2)\Delta z\right)} \tag{3-13c}$$

$$H_x\,|^n_{i,j+1/2,k+1/2} = H^n_x e^{-j\left(\tilde{k}_x i\Delta x+\tilde{k}_y (j+1/2)\Delta y+\tilde{k}_z (k+1/2)\Delta z\right)} \tag{3-13d}$$

$$H_y\,|^n_{i+1/2,j,k+1/2} = H^n_x e^{-j\left(\tilde{k}_x (i+1/2)\Delta x+\tilde{k}_y j\Delta y+\tilde{k}_z (k+1/2)\Delta z\right)} \tag{3-13e}$$

$$H_z\,|^n_{i+1/2,j+1/2,k} = H^n_z e^{-j\left(\tilde{k}_x (i+1/2)\Delta x+\tilde{k}_y (j+1/2)\Delta y+\tilde{k}_z k\Delta z\right)} \tag{3-13f}$$

Substituting (3-13) into (3-6)-(3-7) can lead to (3-12) in the spatial spectral domain in terms of $\tilde{k}_x, \tilde{k}_y, \tilde{k}_z, \Delta t, \Delta x, \Delta y$, and Δz. The definition of $\tilde{k}_x, \tilde{k}_y, \tilde{k}_z, \tilde{k}$ is the same as it in section 2.4.3.

Although this idea is straightforward, the manipulation of the equations is not very handy. With the help of MAPLE, Zheng found eigenvalues of Λ are [47]:

$$\lambda_1 = \lambda_2 = 1 \tag{3-14a}$$

$$\lambda_3 = \lambda_4 = \frac{\sqrt{R^2 - S^2} + jS}{R} \tag{3-14b}$$

$$\lambda_5 = \lambda_6 = \lambda_3^* = \lambda_4^* = \frac{\sqrt{R^2 - S^2} - jS}{R} \tag{3-14c}$$

Here,

$$R = \left(\mu\varepsilon + W_x^2\right)\left(\mu\varepsilon + W_y^2\right)\left(\mu\varepsilon + W_z^2\right) \tag{3-14d}$$

$$S = \sqrt{4\mu\varepsilon\left(\mu\varepsilon W_x^2 + \mu\varepsilon W_y^2 + \mu\varepsilon W_z^2 + W_x^2 W_y^2 + W_y^2 W_z^2 + W_z^2 W_x^2\right)\left(\mu^3\varepsilon^3 + W_x^2 W_y^2 W_z^2\right)} \tag{3-14e}$$

$$W_\alpha = \frac{\Delta t}{\Delta\alpha}\sin\left(\frac{\tilde{k}_\alpha \Delta\alpha}{2}\right) \qquad \alpha = x, y, z \tag{3-14f}$$

It is easy to see that all eigenvalues in (3-14) are unity, which implies the spectral radius of the iteration matrix Λ is unity. Thus the 3D ADI-FDTD method is stable. Also, because the stability is independent of the time step Δt, the ADI-FDTD method is unconditionally stable, and is not restricted by the Courant limit.

3.3.2.3 Stability Analysis with the Generalized ADI Formulation

The stability analysis with the von Neumann's method is hard to manipulate in the 3D ADI-FDTD scheme. Using the matrix method to realize the 3D ADI-FDTD case requires the help of computer to operate complicated matrix operations. Strictly speaking, the von Neumann method which based on the Fourier series applies only to linear difference equations with constant coefficients. Boundary conditions are also neglected in the von Neumann method, which applies only to initial value problems with periodic initial data. Our problem here satisfies these restrictions. For other problems, the von Neumann's method may apply locally where the above restrictions satisfy; otherwise the method is not fully valid. In that case, the energy method may be applied, which is not trivial and beyond the discussion of this thesis [48].

Darms also proved the stability of the ADI-FDTD algorithm with the Generalized ADI-FDTD formulation [49]. In his work, the ADI-FDTD iteration is reconstructed in a more compact form based on the idea of the operator splitting technology. However, since this compact formula can not be implemented in a numerical way directly, details of this derivation will not be discussed here.

3.3.3 Numerical Dispersion

The numerical dispersion error is one of the main error sources that directly affect the accuracy of any kind of the FDTD method. We must know the correct numerical dispersion relation in order to evaluate the performance of the method.

In the literature, the numerical dispersion of the ADI-FDTD method has been analyzed by the authors in [20][41][43][44][49][50]. Since the investigation of the numerical dispersion characteristics is very complicated, all the published works start from the simplest mathematical expression of the ADI-FDTD method. That is, they all assume the media is isotropic, lossless media, and the system is source free. During the evolution of the dispersion analysis, confusions occur in the academic area. An Ping Zhao proved that under the same isotropic assumptions, using the von Neumann's method, the amplification matrix method or present the problem in the generalized ADI-FDTD formula, will all result in the same numerical dispersion relation, which paves the way for further understanding of the numerical dispersion in ADI-FDTD method [51]. Based on their summary and the original investigation on the dispersion relation, we will explain the dispersion relation of the ADI-FDTD method and adding our thought here.

3.3.3.1 1D and 2D Dispersion Analysis using the von Neumann's method

Namiki's original dispersion research assumes amplification factors in two sub-steps are equal [20], which leads to incorrect results. This is fixed by Sun [43][44], and is summarized here. From (3-9) and (3-10),

$$\xi = \xi_1 \xi_2 = e^{j\omega\Delta t} = e^{j(\varphi_1+\varphi_2)}, \tag{3-15}$$

where ξ is the amplification factor of a full update cycle; $\omega = 2\pi f$ is the angular frequency and f is the frequency. From (3-10d), $\varphi_1 = \varphi_2 = \frac{\omega \Delta t}{2}$. The phase of the amplification factor governs the numerical dispersion. Again, from (3-10d), the dispersion relation in a 2D TE ADI-FDTD scheme is

$$\tan^2\left(\frac{\omega \Delta t}{2}\right) = W_x^2 + W_y^2 + W_x^2 W_y^2 \left(= \tan^2 \varphi_1 = \tan^2 \varphi_2\right). \tag{3-16}$$

The above dispersion relation is valid for each individual sub time step, as well as the overall ADI-FDTD method.

The numerical proof of (3-16) is not trivial. Namiki failed to provide the direct comparison between the theoretical results and the numerical experiments in his numerical dispersion investigation in the ADI-FDTD method [52]. Sun attempted to apply numerical experiments to verify the theoretical dispersion relation in (3-16). However, (3-16) is derived based on the plane wave assumption. In order to make a valid verification, Sun used the point source excitation in a very large computation domain (5000×5000) [44]. Locating the observation point as far away as possible from the point source will make the accuracy of using a cylindrical wave to replace the plane wave as high as possible [53]. However, it is pointed out in [53] that the technology used by Sun [44] is not only rough, but also illogical. This left us another open topic in numerical dispersion problems.

3.3.3.2 3D Dispersion Analysis with the amplification matrix method

Corresponding to the section 3.3.2.2, Zheng also analyzed the numerical dispersion as a continuous work of stability studies [47]. Since the numerical dispersion describes the wave propagation characteristics, we will introduce the

angular frequency component $e^{j\omega\Delta t}$. We will use the results derived in (3-12) and (3-14) directly from the previous section. Taking into account the angular frequency component $e^{j\omega\Delta t}$, field components are

$$E_\alpha^n = E_\alpha e^{j\omega\Delta tn}, H_\alpha^n = H_\alpha e^{j\omega\Delta tn}, \ \alpha = x, y, z . \tag{3-17}$$

A compact form is $X^n = Xe^{j\omega\Delta tn}$, where $X = \left(E_x, E_y, E_z, H_x, H_y, H_z\right)^T$. (3-12) becomes

$$\left(e^{j\omega\Delta t} I - \Lambda\right) X = 0, \tag{3-18}$$

where I is a 6×6 identity matrix.

The determinant of the coefficient matrix must be zero in order to obtain the nontrivial solution of the field in (3-18). This gives

$$\left| e^{j\omega\Delta t} I - \Lambda \right| = 0 . \tag{3-19}$$

Again, (3-19) is solved by MAPLE [47]. The results yield the dispersion relations of the 3D ADI-FDTD algorithm:

$$\begin{aligned} &\sin^2\left(\omega\Delta t\right) = \frac{4\mu\varepsilon\left(\mu\varepsilon W_x^2 + \mu\varepsilon W_y^2 + \mu\varepsilon W_z^2 + W_x^2 W_y^2 + W_y^2 W_z^2 + W_z^2 W_x^2\right)\left(\mu^3\varepsilon^3 + W_x^2 W_y^2 W_z^2\right)}{\left(\mu\varepsilon + W_x^2\right)^2\left(\mu\varepsilon + W_y^2\right)^2\left(\mu\varepsilon + W_z^2\right)^2} \\ &or \ \sin^2\left(\omega\Delta t\right) = \frac{S^2}{R^2} \end{aligned} \tag{3-20}$$

where S, R are defined in (3-14).

We perform the same method used in Chapter two to study the numerical dispersion in ADI-FDTD. In other words, we use Newton-Raphson method to solve (3-20) for numerical wavenumber $\tilde{k}$. $\tilde{k}$ is a function of grid size, time-step size, frequency and propagating direction. The relation in (2-35) is also true here.

For cubic cells, Figure 16 shows in both the AID-FDTD and traditional FDTD methods, the numerical phase velocity error reaches minimum at φ=45° (cubic

diagonal), and maximum at 0° and 90° (cubic edge). Note the time step used here is within the Courant limit, and the numerical dispersion of the ADI-FDTD (the upper graph) is very similar as the conventional FDTD (the lower graph). However, with the same cell size and time-step size, the ADI-FDTD has slightly larger dispersion than the traditional FDTD method in all directions.

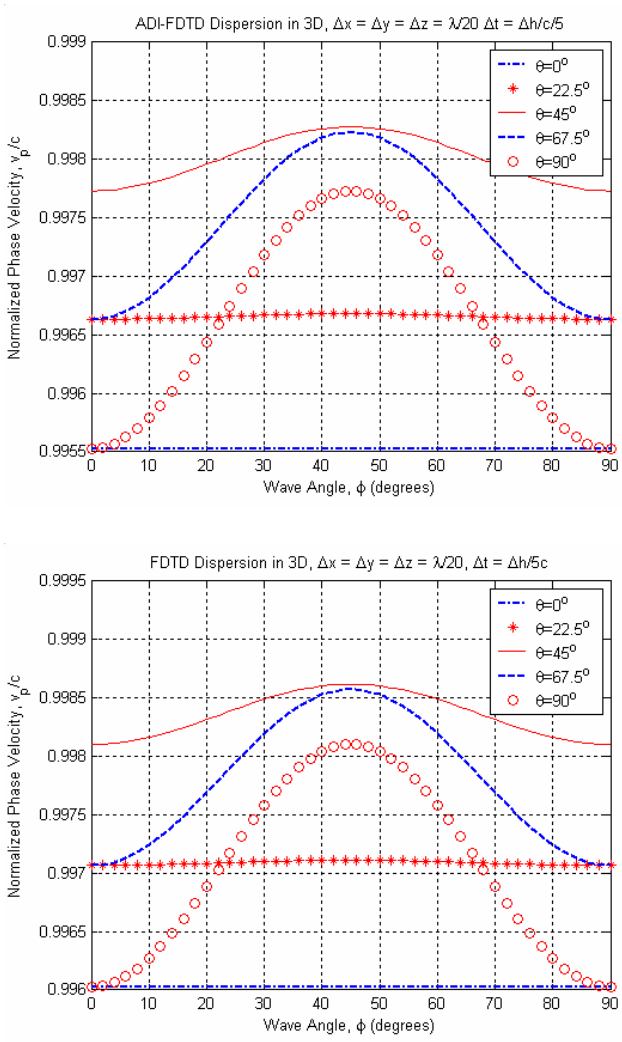

Figure 16 Numerical phase velocity versus wave propagation angle. Δh=λ/20, Δt=Δh/5c. Upper figure is with the ADI FDTD [47]; Lower figure is with the FDTD.

Figure 17 studies dispersion of cubic cells ($\Delta x = \Delta y = \Delta z$) on cone surfaces in ADI-FDTD for larger time steps. Cone surface is defined in Figure 8 (b). Time-steps

used here is larger than the CFL^{FDTD} limit, thus we can not compare it with its FDTD counterpart (FDTD is instable with the time steps used here.).

From the study of numerical dispersion in FDTD, we believe the minimum dispersion occurs when the wave is propagating along the direction which has the shortest "lattice plane" intervals (section 2.4.3). We guess in ADI-FDTD, a similar numerical dispersion will occur. The result in Figure 17 shows partial support to this assumption. When the wave is propagating along the cubic diagonal, the minimum dispersion appears ($\theta = 54.74^o$ curve in both plots). This thought is proposed for the first time to the best of our knowledge. Our future work in dispersion analysis will provide the strict mathematical derivation as well as numerical proof to this assumption.

In ADI-FDTD method alone, when the time step is larger, the dispersion error is larger (In contrast, in FDTD, when the time step reaches maximum, the dispersion reaches minimum.). Thus, the selection of the time step depends on the accuracy of the modeling. Zheng mentioned in his work the time steps could be made up to four times larger than that of the conventional FDTD with acceptable accuracy when a spatial resolution $\delta = \frac{\lambda}{10} \sim \frac{\lambda}{20}$ is used [47]. The time step suggested in his work is stricter than the one suggested in Sun's work [44]. In [44], the time-step size is recommended to be chosen so that the resulting Courant number is much smaller than the mesh density, and satisfies the Nyquist sampling requirement at the same time ($CFL^{ADI} << N/2$). This is equivalent to say $\Delta t << \frac{\lambda}{2c}$. The accuracy of the ADI-FDTD will increase with the finer grid size. The coarse grid errors are larger than the fine

mesh. We would pick the time step between these strict bound [47] and loose bound [44] as long as the error in the simulation is tolerable.

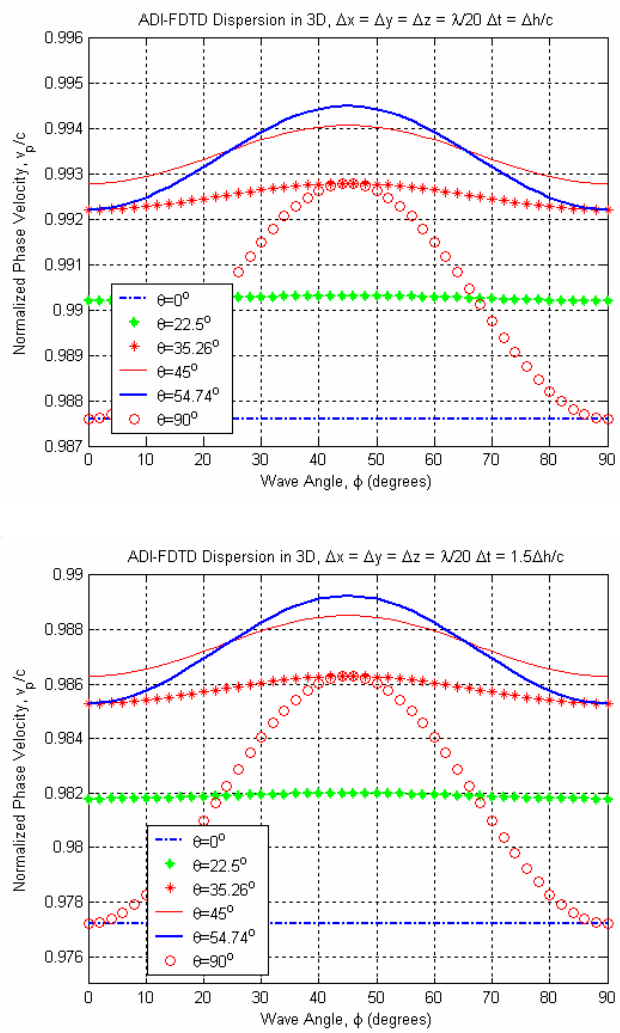

Figure 17 Numerical phase velocity versus wave propagation angle with the ADI-FDTD grid with $\Delta h=\lambda/20$. Upper graph: $\Delta t=\Delta h/c$ ($CFL^{ADI}=\text{sqrt}(3)$). Lower graph: $\Delta t=1.5 \times \Delta h / c$ ($CFL^{ADI}=2.6$).

We will go one step further, and show more dispersion analysis than [47]. Figure 18 analyzes the dispersion on planes parallel to the z axis. The $\varphi = 0^o$, $\varphi = 22.5^o$, $\varphi = 45^o$, $\varphi = 67.5^o$ and $\varphi = 90^o$ planes are all perpendicular to the x-y plane (Figure 8 (a)). Here, the time-step is 2.6 times of the maximum time-step allowed in the FDTD method ($CFL^{ADI} = 2.6$). On these planes, waves propagating along different θ have different phase velocities. Figure 18 shows the dispersion is

larger when the time step is larger. Because the symmetry in cubic cells, waves propagating along $\varphi = 22.5^o$ and $\varphi = 67.5^o$ directions have no difference in dispersion error. Waves propagating along $\varphi = 0^o$ and $\varphi = 90^o$ directions have no difference in dispersion error. This is again can be understood from the "lattice plane" idea. This further explains numerical dispersion (phase error) strongly relates to the discretization of the continuous time-space domain.

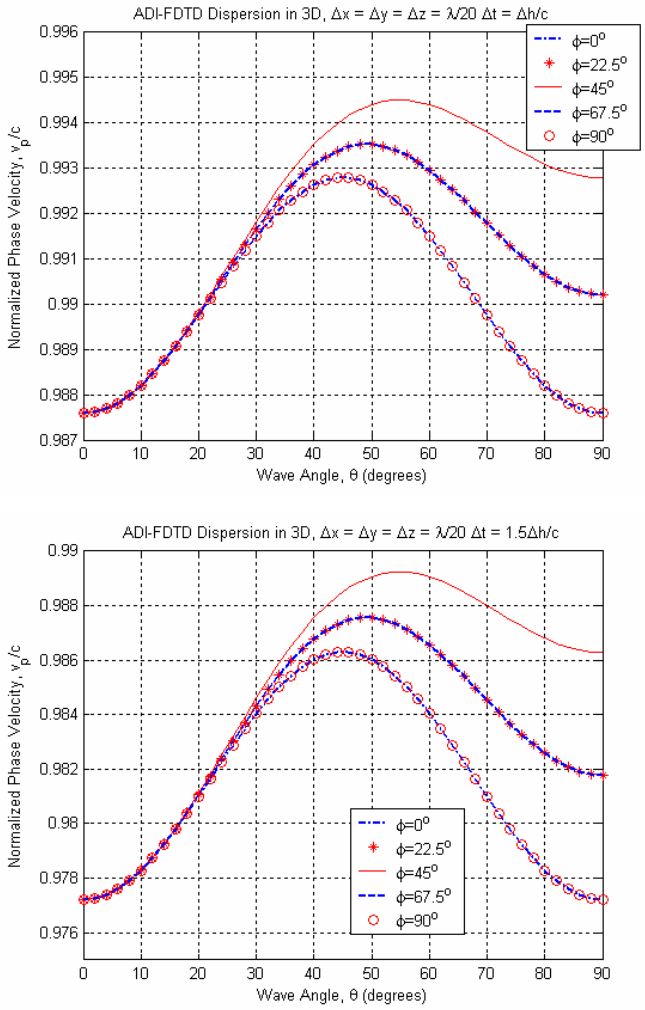

Figure 18 Numerical phase velocity versus wave propagation angle with the ADI-FDTD grid with Δh=λ/20. Upper graph: Δt=Δh/c (CFL^{ADI}=1.73). Lower graph: Δt=1.5 x Δh /c (CFL^{ADI}=2.6).

Now, we show the effect of non uniform grids on the numerical dispersion of ADI-FDTD method. Figure 19 studies the dispersion on the cone surface (Figure 8

(b)). Figure 20 studies the dispersion of the waves propagating on planes perpendicular to the x-y plane (Figure 8 (a)). In both Figure 19 and 20, we use a time-step larger than the maximum allowed time step in the traditional FDTD ($CFL^{ADI}>1$). Cells in both analysis are not cubes ($\Delta x, \Delta y, \Delta z$ are not equal). Approximately the minimum dispersion occurs when the wave propagates perpendicular to the "lattice planes" with the shortest distance.

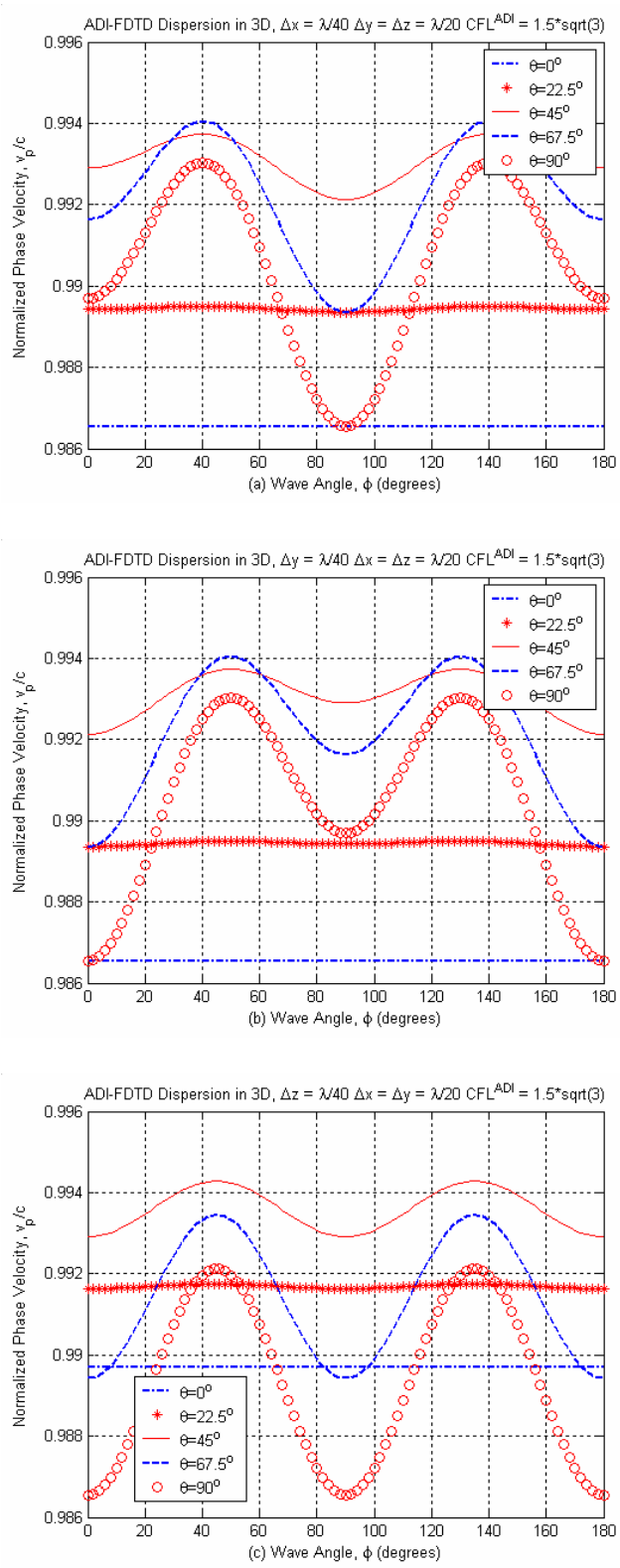

Figure 19 Numerical dispersion of non-cubic cells on the cone surface in 3D ADI-FDTD. Different cell sizes along different propagation directions are compared.

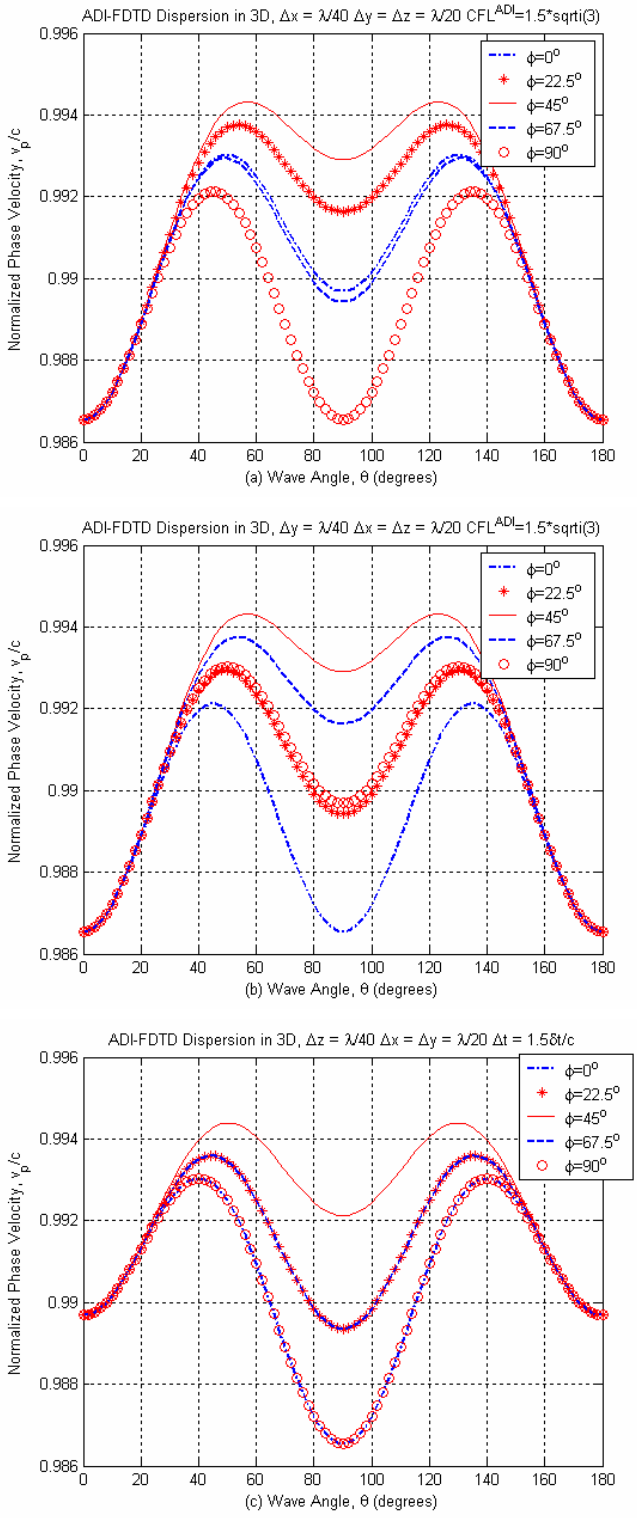

Figure 20 Numerical dispersion of non-cubic cells on planes perpendicular to x-y plane in 3D ADI-FDTD. Different cell sizes along different propagation directions are compared.

3.3.3.3 Dispersion Analysis with the Generalized ADI Formulation

Darms also published the dispersion relation in his studies with the more compact generalized ADI formulation [49]. The result is

$$\tan^2\left(\frac{\omega\Delta t}{2}\right)=\frac{\mu\varepsilon\left(\mu\varepsilon W_x^2+\mu\varepsilon W_y^2+\mu\varepsilon W_z^2+W_x^2W_y^2+W_y^2W_z^2+W_z^2W_x^2\right)}{\left(\mu^3\varepsilon^3+W_x^2W_y^2W_z^2\right)}$$
$$or\ \tan^2\left(\frac{\omega\Delta t}{2}\right)=\frac{P}{Q} \qquad (3\text{-}21)$$

From the trigonometric identity, it can be seen that (3-20) and (3-21) are equivalent to each other.

3.3.3.4 Time-step size choosing

As we mentioned in section 3.3.1, although the ADI-FDTD is an unconditionally stable method, its time-step size is limited by the errors. Guilin Sun showed that at certain time-step sizes, the numerical results are noise-like and no wave travels. Hence, the ADI-FDTD method does have time-step size limitations.

Let's take another look at the dispersion relationship (3-21). To demonstrate the limitation of the time-step, the higher dimensional ADI-FDTD can be collapsed into the one-dimensional case. Thus, the three-dimensional relation (3-21) can be rewritten as

$$\tan^2\left(\frac{\omega\Delta t}{2}\right)=s^2\sin^2\left(\frac{\beta\Delta x}{2}\right) \qquad (3\text{-}22)$$

where s is the Courant Number CFL^{ADI}, defined in (3-11) (3-12). Although the ADI-FDTD is stable for any time-step size, if the left hand side (LHS) of (3-22) is zero, then the phase constant β must be zero, which means the numerical wave does not

propagate. This actually happens when $\frac{\omega\Delta t_1}{2} = n\pi$. When the time step $\Delta t_1 = \frac{2n\pi}{\omega}$, the numerical wave stops propagating. Another observation is that if $\tan^2\left(\frac{\omega\Delta t}{2}\right) > s^2$, then $\sin\left(\frac{\beta\Delta x}{2}\right) > 1$, so β is a complex number ($\beta = \beta_r + j\beta_i$, $j = \sqrt{-1}$), and the wave will decay in space. The extreme case is when $\frac{\omega\Delta t}{2} = (2n+1)\frac{\pi}{2}$ (and thus, $\Delta t_2 = (2n+1)\frac{\pi}{\omega}$) , so the LHS is infinity, and the numerical wave will decay infinitely fast. The reason is discovered here. Let's rewrite (3-22) as

$$\sin^2\left(\frac{\beta\Delta x}{2}\right) = \tan^2\left(\frac{\omega\Delta t}{2}\right)\Big/ s^2 = Z^2 \tag{3-23}$$

Without loss of generality, we assume

$$\frac{\beta\Delta x}{2} = \sin^{-1}(Z) = \chi\,. \tag{3-24}$$

If $Z > 1$, χ is a complex value, which implies β is a complex value. It is worth noting that Z is a real number, not a complex number. The solution of χ is

$$\chi = -j\ln\left(jZ + \sqrt{1-Z^2}\right). \tag{3-25}$$

Because $Z > 1$, we can define $\tilde{Z} = Z + \sqrt{Z^2-1} > 1$. Then, the solution of χ is:

$$\begin{aligned}\chi &= -j\ln\left(jZ + j\sqrt{Z^2-1}\right) = -j\ln\left(j\tilde{Z}\right)\\ &= -j\left(\ln\left(\left|\tilde{Z}\right|\right) + j\arg\left(\left|\tilde{Z}\right|\right)\right) = -j\left(\ln\left(\left|\tilde{Z}\right|\right) + \arg\left(\left|\tilde{Z}\right|\right) = (\beta_r + j\beta_i)\frac{\Delta x}{2}\right.\end{aligned} \tag{3-26}$$

Recall that we have assumed the solution of the wave equation has the form of $Ae^{-j\beta\Delta x}$. Thus, here we have

$$Ae^{-j\beta\Delta x} = Ae^{-j(\beta_r + j\beta_i)\Delta x} = Ae^{-j\beta_r\Delta x}e^{\beta_i\Delta x} = Ae^{-2\left(\ln\left(\left|\tilde{Z}\right|\right)\right)}e^{2j\arg\left(\left|\tilde{Z}\right|\right)}. \tag{3-27}$$

Here, β_i is the attenuation constant and β_r is the phase constant. The first exponential term represents attenuation. It is easy to see that the larger the $\tilde{Z}$, and thus the larger the ratio of $\tan\left(\frac{\omega\Delta t}{2}\right)\Big/ s = Z$, the faster the attenuation is. If the left term goes into infinity, the wave will attenuate infinitely fast.

According to [44], we rewrite (3-22):

$$\cosh(j\beta\Delta h) = \frac{2\tan^2\left(\frac{\omega\Delta t}{2}\right)}{s^2} - 1. \tag{3-28}$$

Here, β is a complex number, such that $\beta = \beta_r + j\beta_i$.

Let the real part and the imaginary part equal on both sides of (3-28), we have

$$1 - \cosh(\beta_i\Delta x)\cos(\beta_r\Delta x) = \frac{2\tan^2\left(\frac{\omega\Delta t}{2}\right)}{s^2} \tag{3-29a}$$

$$\sinh(\beta_i\Delta x)\sin(\beta_r\Delta x) = 0. \tag{3-29b}$$

In (3-26b), either the hyperbolic sine is equal to zero or the sine is zero, or both. If $\left|\tan\left(\frac{\omega\Delta t}{2}\right)\right| < s$, the attenuation constant β_i is zero, the numerical wave travels without attenuation. When $\left|\tan\left(\frac{\omega\Delta t}{2}\right)\right| = s$, both $\sinh(\beta_i\Delta x)$ and $\sin(\beta_i\Delta x)$ are zero, and the velocity limit is reached. If $\left|\tan\left(\frac{\omega\Delta t}{2}\right)\right| > s$, then $\sin(\beta_i\Delta x)$ is zero, and a "faster than the light" numerical wave propagation could happen [44].

According to the Nyquist criterion

$$\Delta h = \frac{\lambda}{2}, \tag{3-30}$$

in one dimensional case, the Courant number ($s = \frac{c\Delta t}{\Delta h}$) and the mush density ($N = \frac{\lambda}{\Delta h}$) has the following relation:

$$s = \frac{N}{2}. \tag{3-31}$$

So, the maximum Courant number is $s = \frac{N}{2}$. For any $s > \frac{N}{2}$, which implies $\Delta h = c\Delta t > \frac{\lambda}{2}$, will not be possible to recover the signal. This should be the upper limit of the time-step size.

In practice, for the accuracy purpose, the Courant number is usually much smaller than the mesh density. The time-step size should be chosen according to this agreement.

3.4.4 Boundary Conditions

The derivation of the PEC boundary condition, the Mur's 1st order boundary conditions and the boundary conditions on the dielectric-dielectric interface is the same as the conventional FDTD method. The difference here is that in each sub-time step, we need to apply the boundary condition once. In each iteration, we perform the boundary condition twice.

For example, in the **first sub-time step** of the n+1 th iteration, **the PEC** boundary condition on the z=k plane is:

$$E_x\,|_{i+1/2,j,k}^{n+1/2} = E_x\,|_{i+1/2,j+1,k}^{n+1/2} = E_y\,|_{i,j+1/2,k}^{n+1/2} = E_y\,|_{i+1,j+1/2,k}^{n+1/2} = 0 \tag{3-32a}$$

The Mur's 1st Absorbing Boundary condition for E_x on the y=0 boundary is:

$$E_x\,|_{i+1/2,0,k}^{n+1/2} = E_x\,|_{i+1/2,1,k}^{n} + \left(\frac{c\Delta t/2 - \Delta y}{c\Delta t/2 + \Delta y}\right)\left(E_x\,|_{i+1/2,1,k}^{n+1/2} - E_x\,|_{i+1/2,0,k}^{n}\right) \tag{3-32b}$$

The Mur's 1st Absorbing Boundary condition for E_x on the y=ny boundary is:

$$E_x\,|^{n+1/2}_{i+1/2,ny,k} = E_x\,|^{n}_{i+1/2,ny-1,k} + \left(\frac{c\Delta t/2-\Delta y}{c\Delta t/2+\Delta y}\right)\left(E_x\,|^{n+1/2}_{i+1/2,ny-1,k} - E_x\,|^{n}_{i+1/2,ny,k}\right) \qquad (3\text{-}32c)$$

The Mur's 1st Absorbing Boundary condition for E_y on the z=0 boundary is:

$$E_y\,|^{n+1/2}_{i,j+1/2,0} = E_y\,|^{n}_{i,j+1/2,1} + \left(\frac{c\Delta t/2-\Delta z}{c\Delta t/2+\Delta z}\right)\left(E_y\,|^{n+1/2}_{i,1+1/2,1} - E_x\,|^{n}_{i,j+1/2,0}\right) \qquad (3\text{-}32d)$$

The Mur's 1st Absorbing Boundary condition for E_y on the z=nz boundary is:

$$E_y\,|^{n+1/2}_{i,j+1/2,nz} = E_y\,|^{n}_{i,j+1/2,nz-1} + \left(\frac{c\Delta t/2-\Delta z}{c\Delta t/2+\Delta z}\right)\left(E_y\,|^{n+1/2}_{i,1+1/2,nz-1} - E_x\,|^{n}_{i,j+1/2,nz}\right) \qquad (3\text{-}32e)$$

The Mur's 1st Absorbing Boundary condition for E_z on the x=0 boundary is:

$$E_z\,|^{n+1/2}_{0,j,k+1/2} = E_z\,|^{n}_{1,j,k+1/2} + \left(\frac{c\Delta t/2-\Delta x}{c\Delta t/2+\Delta x}\right)\left(E_z\,|^{n+1/2}_{1,j,k+1/2} - E_z\,|^{n}_{0,j,k+1/2}\right) \qquad (3\text{-}32f)$$

The Mur's 1st Absorbing Boundary condition for E_z on the x=nx boundary is:

$$E_z\,|^{n+1/2}_{nx,j,k+1/2} = E_z\,|^{n}_{nx-1,j,k+1/2} + \left(\frac{c\Delta t/2-\Delta x}{c\Delta t/2+\Delta x}\right)\left(E_z\,|^{n+1/2}_{nx-1,j,k+1/2} - E_z\,|^{n}_{nx,j,k+1/2}\right) \qquad (3\text{-}32g)$$

In the **second sub-time step** of the n+1 th iteration, **the PEC** boundary condition on the z=k plane is:

$$E_x\,|^{n+1}_{i+1/2,j,k} = E_x\,|^{n+1}_{i+1/2,j+1,k} = E_y\,|^{n+1}_{i,j+1/2,k} = E_y\,|^{n+1}_{i+1,j+1/2,k} = 0\,. \qquad (3\text{-}32h)$$

The Mur's 1st Absorbing Boundary condition for E_x on the z=0 boundary is:

$$E_x\,|^{n+1}_{i+1/2,j,0} = E_x\,|^{n+1/2}_{i+1/2,j,1} + \left(\frac{c\Delta t/2-\Delta z}{c\Delta t/2+\Delta z}\right)\left(E_x\,|^{n+1}_{i+1/2,j,1} - E_x\,|^{n+1/2}_{i+1/2,j,0}\right) \qquad (3\text{-}32i)$$

The Mur's 1st Absorbing Boundary condition for E_x on the z=nz boundary is:

$$E_x\,|^{n+1}_{i+1/2,j,nz} = E_x\,|^{n+1/2}_{i+1/2,j,nz-1} + \left(\frac{c\Delta t/2-\Delta z}{c\Delta t/2+\Delta z}\right)\left(E_x\,|^{n+1}_{i+1/2,j,nz-1} - E_x\,|^{n+1/2}_{i+1/2,j,nz}\right) \qquad (3\text{-}32j)$$

The Mur's 1st Absorbing Boundary condition for E_y on the x=0 boundary is:

$$E_y\,|_{0,j+1/2,k}^{n+1} = E_y\,|_{1,j+1/2,k}^{n+1/2} + \left(\frac{c\Delta t/2-\Delta x}{c\Delta t/2+\Delta x}\right)\left(E_y\,|_{1,j+1/2,k}^{n+1} - E_y\,|_{0,j+1/2,k}^{n+1/2}\right) \quad \text{(3-32k)}$$

The Mur's 1st Absorbing Boundary condition for E_y on the x=nx boundary is:

$$E_y\,|_{nx,j+1/2,k}^{n+1} = E_y\,|_{nx-1,j+1/2,k}^{n+1/2} + \left(\frac{c\Delta t/2-\Delta x}{c\Delta t/2+\Delta x}\right)\left(E_y\,|_{nx-1,j+1/2,k}^{n+1} - E_x\,|_{nx,j+1/2,k}^{n+1/2}\right) \quad \text{(3-32l)}$$

The Mur's 1st Absorbing Boundary condition for E_z on the y=0 boundary is:

$$E_z\,|_{i,0,k+1/2}^{n+1} = E_z\,|_{i,1,k+1/2}^{n+1/2} + \left(\frac{c\Delta t/2-\Delta y}{c\Delta t/2+\Delta y}\right)\left(E_z\,|_{i,1,k+1/2}^{n+1} - E_x\,|_{i,0,k+1/2}^{n+1/2}\right) \quad \text{(3-32m)}$$

The Mur's 1st Absorbing Boundary condition for E_z on the y=ny boundary is:

$$E_z\,|_{i,ny,k+1/2}^{n+1} = E_z\,|_{i,ny-1,k+1/2}^{n+1/2} + \left(\frac{c\Delta t/2-\Delta y}{c\Delta t/2+\Delta y}\right)\left(E_z\,|_{i,ny-1,k+1/2}^{n+1} - E_x\,|_{i,ny,k+1/2}^{n+1/2}\right) \quad \text{(3-32n)}$$

Again, the boundary condition on the dielectric-dielectric interface is automatically satisfied.

3.4 Summary

The numerical stability and dispersion discussed in this chapter are based on the simplest mathematic forms, namely, they are specified for the system with isotropic media. The von Neumann's method, the amplification matrix method, and the generalized ADI formulation have been applied in studying the numerical stability and dispersion relations.

It has been proven with all these methods that for the isotropic, source free problem, in all 1-D, 2-D, and 3-D ADI-FDTD schemes, the ADI-FDTD is unconditionally stable.

For anisotropic materials, although the idea of stability and dispersion analysis is straightforward, the matrix manipulation is beyond the scope of hand derivation. A

much simpler energy-based stability proof is found in the literature [35]. It is possible to use the energy-based method to obtain the stability and dispersion relation for anisotropic materials, which is left for future research.

Chapter 4: Study the MISM structure with the ADI-FDTD method

4.1 Interconnect Model

The metal-insulator-semiconductor-metal (MISM) plane interconnect is one of the most elementary components in the modern integrated circuits. This unit is a four layered structure, and it's demonstrated in Figure 21. Figure 22 shows the side view of the MISM structure. This 2-D structure neglects the fringing effect of the metal line, and approximates the model to be a two-dimensional parallel plate wave guide. The earlier research has defined three fundamental propagation modes existed in this structure by solving wave equations [2] - [3].

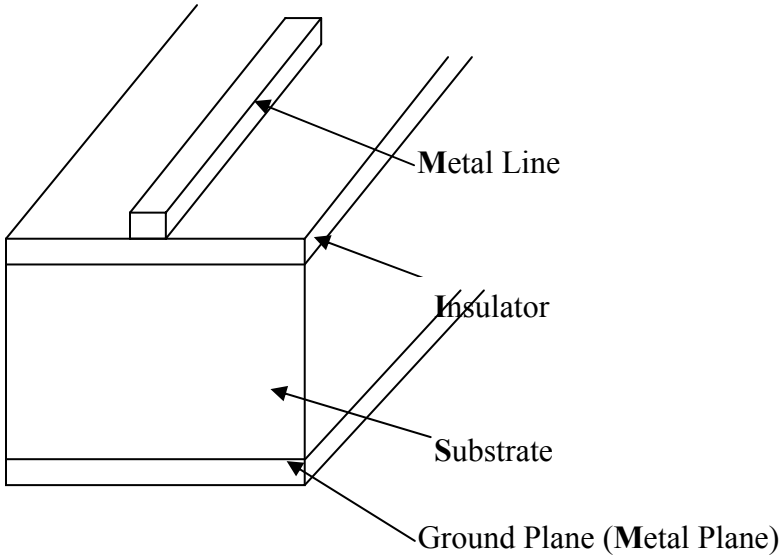

Figure 21 The Metal-Insulator-Substrate-Metal (MISM) structure

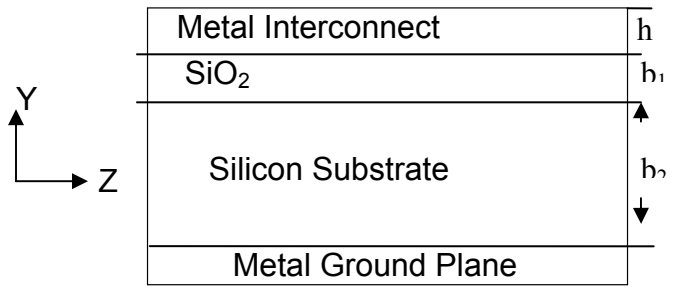

Figure 22 Side view of the MISM structure. Z is the direction of propagation. h, b1, and b2 is the thickness of the metal layer, the SiO2 layer, and the silicon substrate, separately.

4.2 Quasi-Analytical Analysis and 3-Mode Limits

The MISM structure gives rise to a four layered boundary problem. In the quasi-analytical analysis, we neglect the metal thicknesses, and extend the line width to infinity. We use Perfectly Electric Conductor (PEC) boundary conditions for the top and bottom metal layers. The equations for the longitudinal and the transverse propagation constants have been derived previously [2], and are written below:

$$\gamma_i^2 + \gamma^2 = -k_0^2 \mu_i \varepsilon_i^{'} \quad \text{i=1,2} \tag{4-1}$$

$$\sum_i \frac{\gamma_i}{\varepsilon_i^{'}} \tanh(\gamma_i b_i) = 0 \quad \text{i=1,2,} \tag{4-2}$$

where γ_1 and γ_2 denote the transverse propagation constants (y direction) in SiO_2 and Si layers, respectively, and γ is the longitudinal one (z direction). Here, $\gamma = \alpha + j\beta$, where α is the attenuation constant (Np/m), and β is the phase constant (rad/m). k_0 is the wave number in free space, and $\varepsilon_i' = \varepsilon_i + \sigma_i/(j\omega\varepsilon_0)$, i=1,2. ε_0 and μ_0 are the permittivity and permeability in the vacuum, respectively.

The attenuation constants and the phase constants are calculated from (4-1) and (4-2) using the Newton-Raphson method. They are the functions of both the conductivity and the frequency. A direct way to observe the relationship of

attenuation constants and phase constants between conductivity and frequency is to plot those constants on frequency-conductivity map (similar to the plot in [3] and [55]). However, in semiconductor problems, it is not proper to use conductivity as an evaluation factor. The reason is discussed below.

Conductivity describes the ability of moving free charge and forming conduction current (drift current) for a material. Drift current is the summation of all the charge carriers traveling along the same direction. For example, the drift current generated by free electrons is defined as:

$$J = \sum_{i=1}^{n} -qv_i = -nqv_d = nq\mu_n E \tag{4-3}$$

Here, n is the number of electrons, q is electronic charge, v is drift velocity, μ_n is mobility of electron. Drift velocity is defined as

$$v_d = -\mu_n E\,, \tag{4-4}$$

Mobility μ describes how easily an electron moves in response to an applied electric field E. Unlike most metals, drift current in semiconductor materials is the joint contribution of the movement electrons and holes. The total drift current J can be written as the sum of the electron current J_n and hole current J_p:

$$J = J_n + J_p = \left(nq\mu_n + pq\mu_p\right)E\,. \tag{4-5}$$

n is electron concentration, q is the hole concentration. μ_n is the electron mobility, and μ_p is the hole mobility. For semiconductors, conductivity depends on the concentration and mobility of both electrons and holes:

$$\sigma = nq\mu_n + pq\mu_p \tag{4-6}$$

Silicon is a typical semiconductor material used in the IC's industry. Intrinsic silicon at room temperature acts like an insulator. The electrical conductivity of silicon is dominated by the type and concentration of the impurity atoms, or dopants. The number of dopants per unit volume is called doping density (cm^{-3}). Conductivity of the semiconductor is influenced by multiple factors, such as doping density, temperature and mobility. Using conductivity as a single factor to evaluate semiconductor characteristics will hide the effect of these fundamental physical factors.

Therefore, it is more reasonable to pick either mobility or doping density as the fundamental factor to evaluate semiconductor's behavior. However, mobility of electrons and holes results from carriers scattering, which is influenced by temperature, doping density, semiconductor defects, etc.. It is also a complicated physical parameter. On the other hand, doping density is determined simply by the technology. Although the results of the phase and attenuation constants are solved from Maxwell's equations, in which the conductivity is a standard variable, it is physically more logical to use doping density in the semiconductor context to discuss the solution.

Figure 23 illustrates the relation between dopant density (doping density) and resistivity (the inverse of conductivity) at 296 K from measurement [54]. It shows that the conductivity is approximately proportional to the doping density.

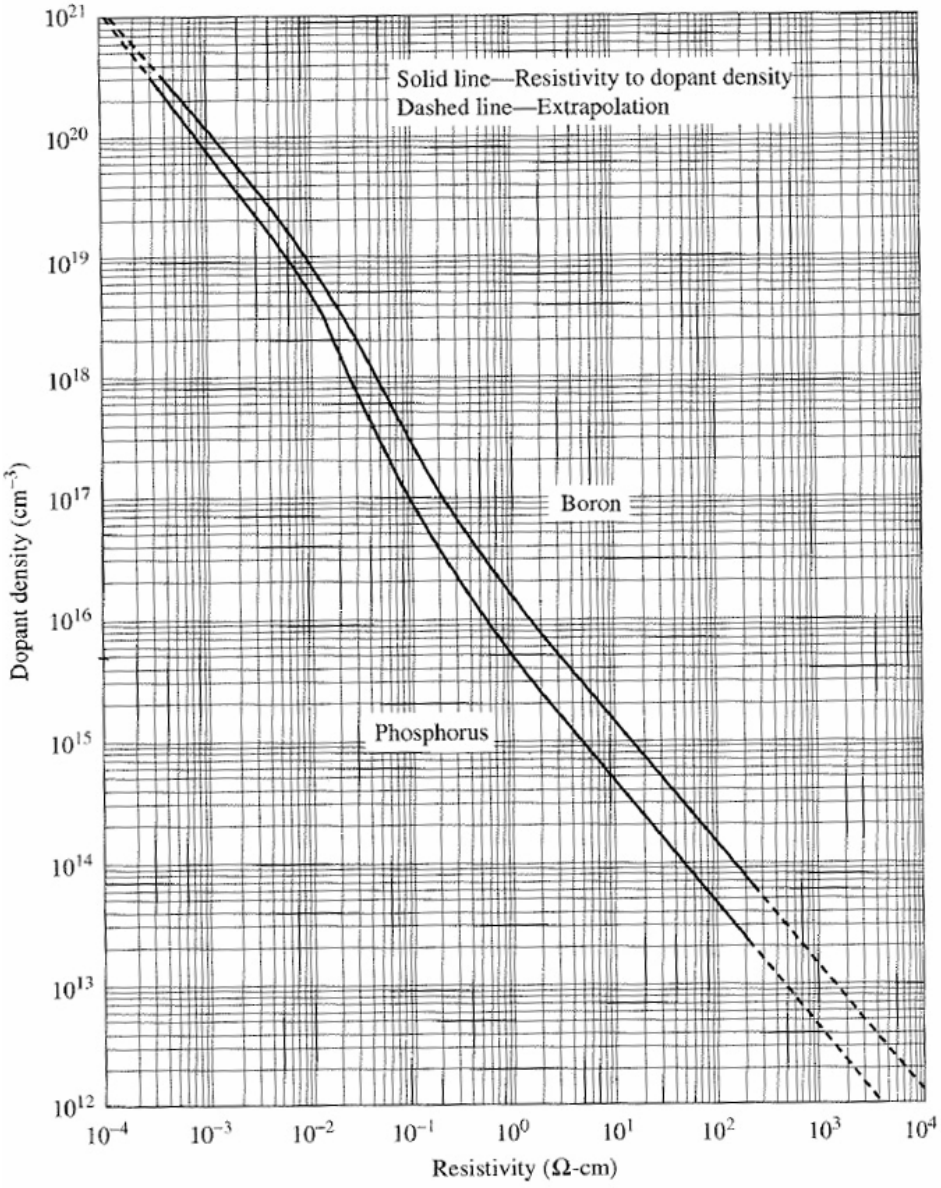

Figure 23 Dopant density versus resistivity at 296 K for silicon doped with phosphorus and with boron [54]

One empirical expression describes the dependence of mobility on temperature and doping density [56]:

$$\mu_n = 88T_n^{-0.57} + \frac{1250T_n^{-2.33}}{1+\left[N/\left(1.26\times10^{17}T_n^{2.4}\right)\right]0.88T_n^{-0.146}} \tag{4-7a}$$

$$\mu_p = 54.3T_n^{-0.57} + \frac{407T_n^{-2.33}}{1+\left[N/\left(2.35\times10^{17}T_n^{2.4}\right)\right]0.88T_n^{-0.146}} \tag{4-7b}$$

where $T_n = T/300$ with T measured in K (Kelvin), and N is the total doping density in silicon. (4-7) is useful up to doping densities of 10^{20} cm^{-3}, and for temperatures between 250 and 500 K [56].

From (4-6) and (4-7), we express conductivity as a function of doping density (4-8). We do not include the temperature effect is our work at present, thus T will be fixed at 300 K ($T_n = T/300 = 1$) in our analysis. Use (4-8a) for n-type substrate, and (4-8b) for p-type substrate. N_d and N_a are the doping density of phosphorus donors and boron acceptors (corresponds to n-type substrate and p-type substrate) separately.

$$\sigma = q\left(88 + \frac{1250}{1 + 0.698 \times 10^{17} N_d}\right) N_d \tag{4-8a}$$

$$\sigma = q\left(54.3 + \frac{407}{1 + 0.3745 \times 10^{17} N_a}\right) N_a \tag{4-8b}$$

In Figure 24 and 25, the x axis is the doping density of the semiconductor. In Figure 24, three bold lines divide the map into 3 fundamental mode regions, between which is the transition region. The definitions of various characteristic frequencies can be found in [3]. The characteristic frequency for the skin-effect in the Si substrate is $f_\delta = 1/(2\pi)\cdot 2/(\mu_0 \sigma_2 b_2^2)$, the dielectric relaxation frequency in the Si substrate is $f_e = 1/(2\pi)\cdot \sigma_2/(\varepsilon_2 \varepsilon_0)$, and the characteristic frequency of slow-wave mode is $f_0 = (f_s^{-1} + 2/3 \cdot f_\delta^{-1})^{-1}$. $f_s = 1/(2\pi)\cdot \sigma_2/(\varepsilon_2 \varepsilon_0)\cdot (b_1/b_2)$ is the relaxation frequency of the interfacial polarization. The location of these edge lines depends on both the geometrical factors (b_1,b_2), and the electrical factors (σ_2,ε_1,ε_2). σ is defined in (4-8). We used Figure 23 to complete the conductivity-doping density mapping in Figure 24 and 25.

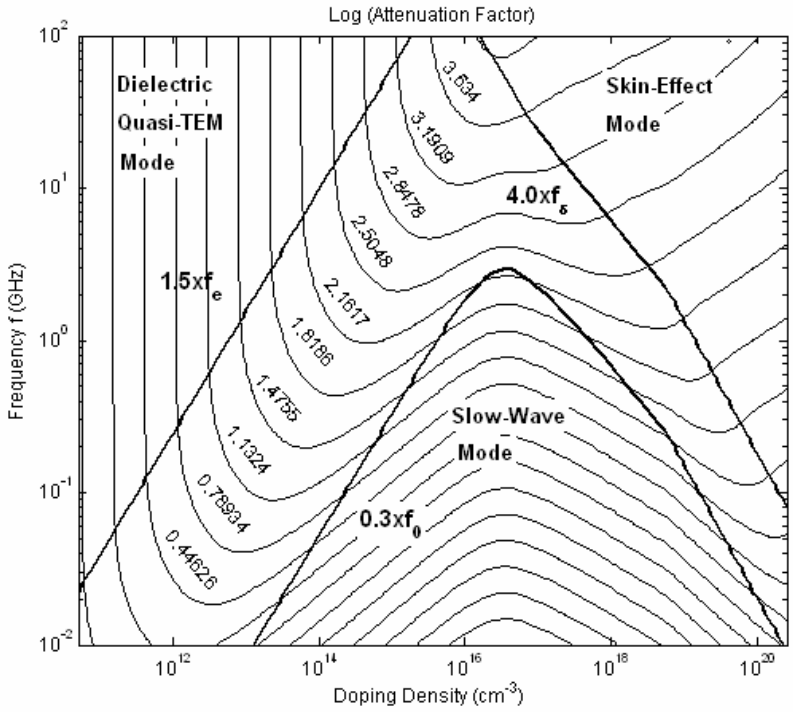

Figure 24 Contour of attenuation factor α (along propagation direction z) vs. substrate doping and wave frequency. MISM structure properties: b1=2μm, b2=200μm. The three bold lines divide the map into 3 regions of fundamental modes as marked.

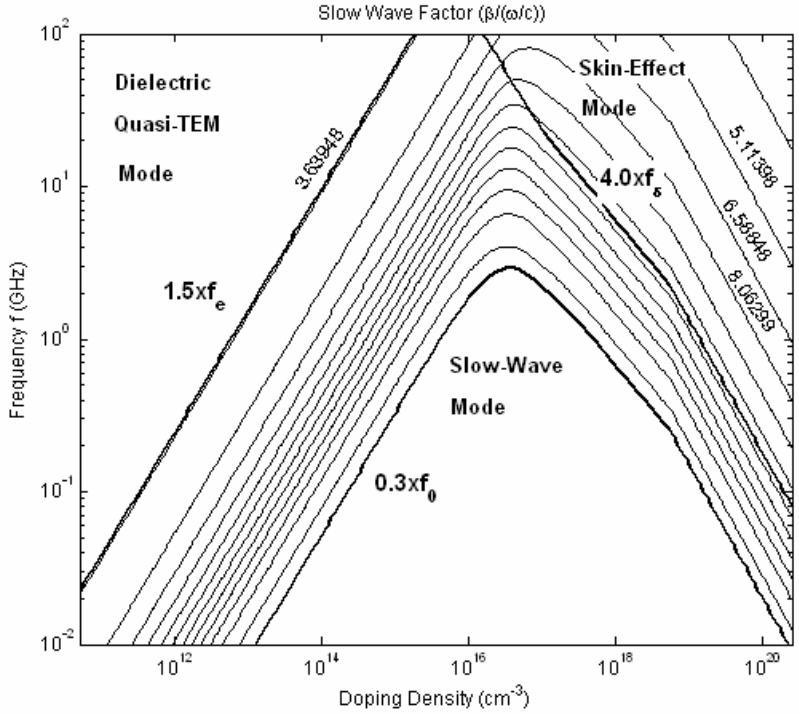

Figure 25 Contour of normalized phase constant β/(ω/c) (along propagation direction z) vs. substrate doping and wave frequency. MISM structure properties: b1=2μm, b2=200μm. The three bold lines divide the map into 3 regions of fundamental modes as marked.

The physical understandings of those three fundamental propagation modes are interpreted as follows [3]:

- **Dielectric quasi-TEM mode:**

When the product of the frequency and the resistivity (and thus the inverse of the doping density) of the Si-substrate is large to produce a small dielectric loss angle ($\tan\delta = \frac{\sigma}{\omega\varepsilon} = \frac{1}{2\pi f\rho\varepsilon}$), then the substrate performs like dielectric materials. The interconnect can be treated as a microstrip line lying on double layer dielectric materials (The Si-substrate layer and the Silicon-dioxide layer). At this region, the interconnects reach their dielectric limit. The fundamental mode would closely resemble to the TEM mode as long as the wavelength is much larger than the thickness of the double layer (This means the operation frequency is much less than the cutoff frequency of TM mode. Therefore, only TEM mode exists.). Both the transverse electric and the magnetic fields penetrate into the substrate and transmit at the velocity nearly equal to $\frac{c_0}{\sqrt{\varepsilon_{Si}}}$.

- **Skin-effect mode**

When the product of the frequency and the substrate conductivity (and thus the substrate doping-density) is large enough to yield a small penetration into the silicon ($\delta_{Si} = \sqrt{\frac{1}{\pi\sigma_{Si} f\mu}}$), the transmission line may be regarded as a microstrip line lying on an imperfect ground plane made of silicon. The substrate thus acts like a lossy conductor wall, and the interconnects reach their conductor limit.

- **Slow-wave mode**

When the frequency is not very high (comparable to the dielectric relaxation frequency f_e, $f << f_{dielectric-relaxation} \equiv \frac{\sigma_{Si}}{2\pi\varepsilon_{Si}\varepsilon_0}$), and when the depth of the quasi-static field penetrating into the substrate is smaller than the skin depth ($h << \delta_{Si} \equiv \frac{1}{\sqrt{\pi f \mu \sigma_{Si}}}$), another type of propagation exists. A slow-surface wave will propagate along the line. In this mode, there is visually no electric field in the substrate; the electric energy is stored in the SiO_2 layer, while magnetic energy penetrates to the Si substrate region. Almost all the active power is transmitted through the SiO_2 layer, but a large amount of reactive power is exchanged between two layers across the Si- SiO_2 interface with the charge movement at the interface. At this range the silicon substrate behaves neither like the dielectric nor the conductor, and it is called the slow-wave region [2][3], because at this region, due to Maxwell-Wagner mechanism, when $b_1 << b_2$, there is a strong interfacial polarization, and ε_{Si0} becomes very large, and the propagation speed of the wave becomes quite slower than in the free space according to $v = \frac{c}{\sqrt{\varepsilon_{Si0}}}$. The slowing down of the propagation velocity is the result of the energy transfer across the interface.

Between these three modes on the frequency-doping density map, there exists transition regions, where the performance of interconnects are more complicated. At early stage, the on-chip interconnects mostly operates in the slow-wave mode region. At present day, interconnects have the trend to operate in the transition region and in the skin-effect region.

Provided with the detailed insight of the different propagation types of interconnects, we will use the numerical technique to investigate the wave dispersion, distortion, and substrate loss in the different modes, especially in the transition region and in the skin-effect mode. First, we will provide the benchmark of our numeric simulation.

4.3 Validation of the Algorithm

We used the experimental measurements of the propagation constant of a MISM structure from [3] as the accurate results. The properties of the MISM structure is: width = 1600μm, b_1=1μm, b_2 = 250μm, and substrate resistivity ρ_2= 85Ω·cm. The wave is propagating from the transition region to the dielectric quasi-TEM mode in this structure when the frequency changes from hundreds of MHz to 4 GHz according to the measurement.

In order to obtain the frequency dependent effects (such as the dispersion) from the time-domain method, a popular method is to use a narrow pulse in the time domain as the excitation of the simulated problem, and then perform the Fourier's analysis on the simulated results. A narrow pulse has abundant frequency components. With one run of the simulation, the whole frequency spectrum may be obtained, and it is very efficient. However, this method should be done very carefully, because the frequency-domain parameter extraction using the Fourier's transform is very sensitive to the tail of the time-domain responses. A small deviation in the time-domain results may lead to a large error in the frequency domain results.

The ADI-FDTD application is performed on the physical model shown in Figure 22. In order to solve the problem in a finite region, proper boundary has to be

made to the simulation. The bottom plane is the metal ground plane in our structure. The ground plane is assumed to be lossless, so its conductivity is infinity. In our numerical simulation, the Perfect Electric Conductor (PEC) boundary condition is added on this ground plane. In a physical scenario, the metal line is excited at one end and propagating to the other end. We must eliminate the reflections at the end of the metal line, so that it is easy to extract the attenuation factor and the phase factor. This can be done by assuming the metal interconnect is long enough, so that during the interested observing time, the pulse did not reach the end of the metal line, and thus there's no physical reflections happening. On the other hand, we don't want the artificial reflections affect the accuracy of the simulation. This is obtained by putting the Mur's 1st absorbing boundary condition [35] on the plane at the other end of the metal line. This treats the metal line as infinite long, which is the same as if the metal line has a matched load at the end. In reality, the region above the MISM structure is the open air region. Again, we will use the Mur's 1st absorbing boundary condition to truncate the simulation domain, such that the exterior region (the region we truncated, and did not calculated in the simulation) and the interior region (the region we fully simulated) are matched. In this way, all the energy should go from the interior region to the exterior region freely without reflection.

We carefully performed our simulation by exciting the system by a Gaussian pulse in the ADI-FDTD simulation at one end

$$E_y = E_{y0} e^{-(t-3\tau)^2/\tau^2}. \tag{4-9}$$

E_{y0} is the amplitude of the magnetic field at the starting end of the interconnect. E_{y0} points to negative y direction in Figure 22, and E_y propagates along positive z direction as time goes by. We will use the normalized E_{y0} in our simulation ($E_{y0} = 1V/m$). The time constant τ is 100 ps, so the bandwidth is around 5GHz. The attenuation constant and the phase constant of the multilayered MIS structure is written into one variable $\gamma(\omega) = \alpha(\omega) + j\beta(\omega)$. This can be extracted from the ADI-FDTD results in the time domain by the Fourier transform

$$e^{-\gamma(\omega)l} = E(\omega, z = z_{ref} + l) / E(\omega, z = z_{ref}), \tag{4-10}$$

where $E(\omega, z)$ is the Fourier transform of the electric field in the substrate at position z along the metal line.

Figure 26 plots the attenuation constant and the phase constant (by showing the normalized wavelength). Generally good agreement is observed in the ADI-FDTD numerical calculation with the analytical analysis and the measurements. This result is more accurate compared to the one published in [26].

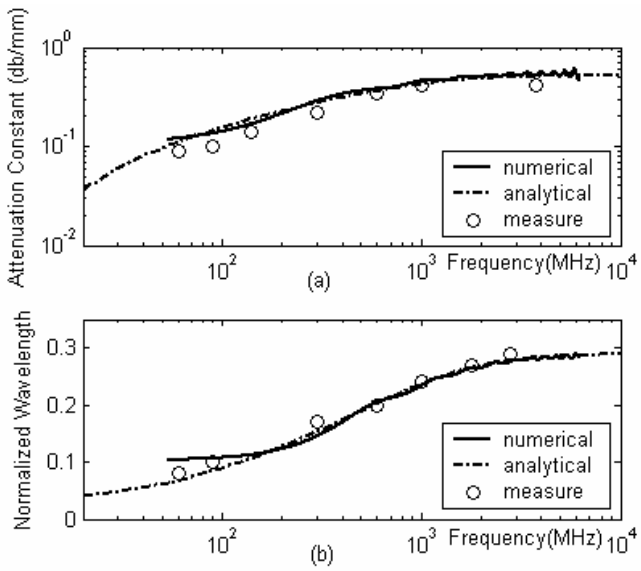

Figure 26 Comparison among the analytical solution, the ADI-FDTD solution, and the measurements, w=1600μm, b1=1μm, b2=250μm, ρ2=85Ω·cm.

(a) attenuation constant; (b) normalized wavelength.

4.4 Numerical Analysis: Extracting Propagation Modes and Constants

We next use our ADI-FDTD simulator to analyze the structure in Figure 22. In contrast with the quasi-analytical approach, here we account for the thickness of the metal interconnect. The metal line is excited at one end; Mur's 1st absorbing boundary condition [42] is applied on the open region, and the PEC boundary condition is added on the ground plane. We consider a MISM structure with h=1.8 μm, b_1=2 μm, b_2=200 μm, and the metal conductivity to be $\sigma_{Al}=3x10^7$ S/m. A sharp Gaussian pulse with time constant τ = 8.83 ps (bandwidth is about 50 GHz) is used as the excitation waveform. 82 uninformed grids are laid out along the y direction with the minimum grid size of 0.1 μm inside the oxide and the metal layers; 29 grid points

in the y direction are laid out in the upper free space region; 240 uniform grid points are laid out along the z direction with Δz=150 μm.

For the traditional FDTD, Δt_{FDTD} must be less than 3.3×10^{-16} s to satisfy the CFL stability limit. In our simulation, the time step is $\Delta t_{ADI\text{-}FDTD}=2 \times 10^{-13}$ s, which is an acceptable choice according to [44]. This helps to calculate the field distribution in the very thin silicon skin depth region in the skin-effect mode, and the field distribution in the metal layer in all three modes of propagation.

From the ADI-FDTD solution we extract the attenuation factor and the phase factor, as a function of frequency and semiconductor doping. This is achieved by applying the Gaussian pulse in the time domain as described above, and then taking the Fourier transform. The propagation constants extracted from ADI-FDTD electromagnetic field time domain solutions are shown in Figure 27 for a frequency range of 1 GHz to 50 GHz, and the substrate dopings of 8.9×10^{11} cm^{-3}, 8.9×10^{16} cm^{-3} and 6.9×10^{19} cm^{-3}. The curve corresponding to a doping of 6.9×10^{19} cm^{-3} represents operation in the skin-effect mode. The curve corresponding to a doping of 8.9×10^{11} cm^{-3} represents propagation in the dielectric quasi-TEM mode. The middle range curve, with doping of 8.9×10^{16} cm^{-3}, reflects propagation ranging from the slow-wave mode to the transition mode, and then to the skin-effect mode as the frequency increases. In the skin-effect mode, the loss is higher, and the phase velocity is relatively large, whereas in the dielectric quasi-TEM mode, they are both relatively small constant. The numerical results in each case also match the quasi-analytical calculations.

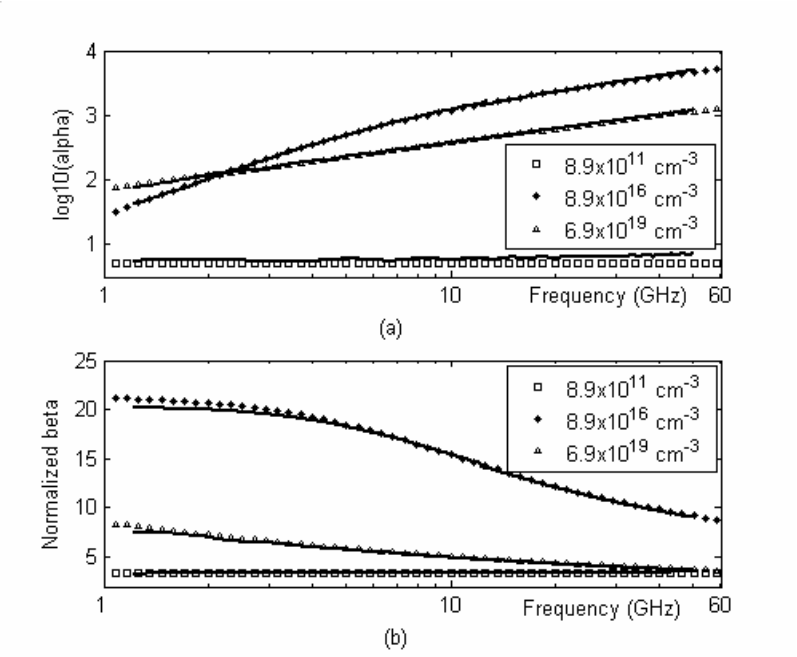

Figure 27 Propagation constant versus frequency and doping density for the quasi-analytical and ADI-FDTD numerical analysis. b1=2 μm, b2=200 μm. The lines with markers are the quasi-analytical results, and the solid lines are the numerical results

(a) attenuation constant; (b) normalized wavelength.

4.5 Numerical Analysis: Calculating Field Distributions in Mixed Dimensional Structures

To further understand the energy flow and distribution in each mode, a comparison of the field distributions obtained from the ADI-FDTD full-wave results is made. In Figure 28 (a)-(c), the sine wave with the frequency of 60 GHz is excited on the MISM with doping = 1.0 x10^{20} cm^{-3}, and the field is taken at t=40 ps. The skin-effect mode field distribution is observed as expected. In Figure 28 (d)-(f), a sine wave with frequency of 1 GHz is excited on the MISM structure with doping = 8.9x10^{16} cm^{-3}; the field is taken at t=1 ns, and the slow-wave mode field distribution is shown. In Figure 28 (g)-(i), a sine wave with frequency of 4 GHz is excited on the

MISM with doping = 1.8×10^{13} cm^{-3}; the field is taken at t=0.6 ns, and the dielectric quasi-TEM field distribution is shown. The field is normalized to the field in the oxide layer in each of the 3 cases. In the last two modes, in order to show at least one period of the wave pattern, we elongated the interconnects to 60 mm, which is larger than their actual on-chip length. In the skin-effect mode, the field in the Si substrate is concentrated close to the SiO_2-Si interface, with an equivalent skin-depth of 10 to 20 μm; whereas in the dielectric quasi-TEM mode, the field penetrates through the Si substrate. This also proved that since in the skin-depth mode, the electric energy penetration is 5 to 10 times of the thickness of the SiO_2 layer, the quasi-TEM approximation is not valid here. In the slow-wave mode, although the field extends all the way down to the substrate, its magnitude is orders less than the field in the SiO_2 layer. This implies that relatively little electric energy penetrates into the Si substrate. This verifies our first-insight to the energy transform in the slow-wave mode in our quasi-analytical analysis. The energy is propagating along the interface of the silicon-substrate layer and the oxide layer. In our numerical simulation, we show that in the skin-effect mode, the field in the metal layer is concentrated close to the Al-SiO_2 interface with a skin depth of less than one micrometer (for the case considered here). In the other two modes, the field is distributed more evenly in the metal layer. In the substrate, the skin depth is larger.

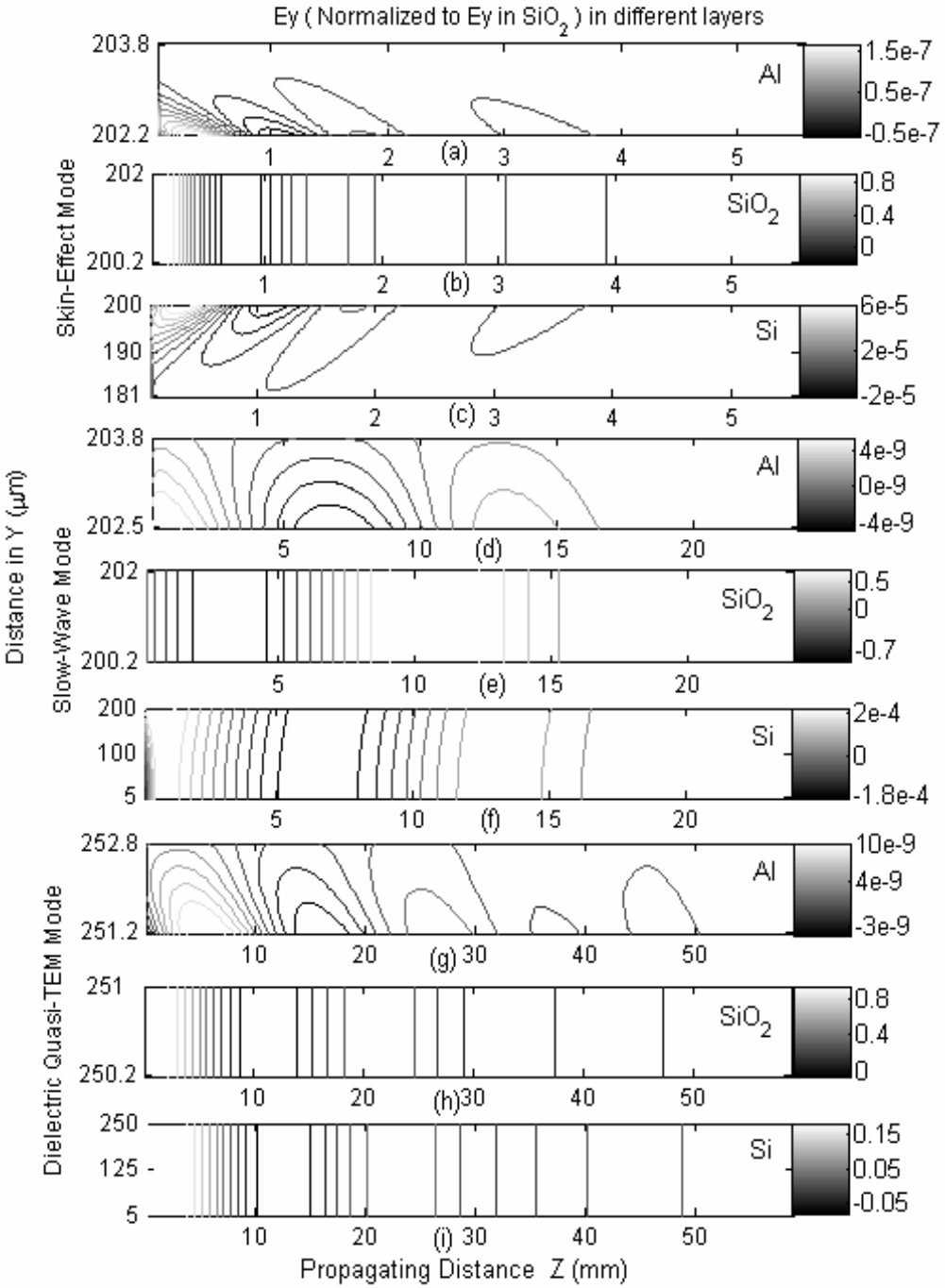

Figure 28 Ey distribution in different layers in 3-mode

(a)-(c) skin-effect mode, h=1.8 μm, b1=2 μm, b2=200 μm, doping density = $1x10^{20}$ cm^{-3}, t=40 ps, f=60 GHz;
(d)-(g) slow-wave mode, h=1.8 μm, b1=2 μm, b2=200 μm, doping density = $8.9x10^{16}$ cm^{-3}, t=1 ns, f=1 GHz;
(h)-(i) dielectric quasi-TEM mode, h=1.8 μm, b1=1 μm, b2=250 μm, doping density =$1.8x10^{13}$ cm^{-3}, t=0.6 ns, f=4 GHz.

4.6 Numerical discrepancies between the quasi 2-D analysis and the strict 3-D analysis of the MISM structure.

This analysis is inspired when we were digging the fundamental characteristics of the MISM on-chip structure in 2-D and 3-D analysis. As mentioned in [44], the 3-D ADI-FDTD has the intendance to have a larger error than its 2-D counterpart, or the implicit Crank-Nicholson FDTD or the conventional FDTD.

Let's consider the four layered MISM structure with doping density $n1=10^{18}/cm^3$, and $n2=10^{16}/cm^3$. The excitation is a digital pulse with the width of 10ps, and the rising and falling time of 2ps. Figure 29 is the transient voltage at different locations along the metal line calculated from the two-dimensional waveguide model, which ignored the fringing effect of the metal.

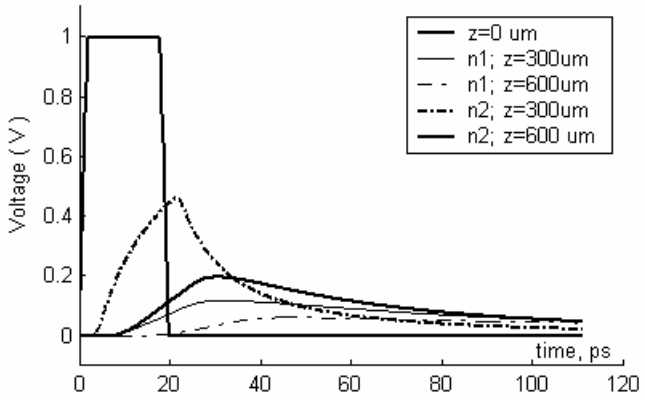

Figure 29 The transient digital signal propagating along the z direction. The result is from the two-dimensional waveguide model.
$n1=10^{18}/cm^3$, and $n2=10^{16}/cm^3$. b1=2 μm, and b2=200 μm. The metal height is 1.8 μm. The observation points are at z=300 μm, and 600 μm

From Figure 29 we found that the substrate with the doping density of $n2=10^{16}/cm^3$ has higher loss than the substrate doping density of $n1=10^{18}/cm^3$. The further away from the signal, the higher the loss is for both doping densities.

However, the magnitude of the voltage observed from the two-dimensional simulation appears to be smaller than the real case. A similar result is also found in [29]. This is due to the large dissipation of the two-dimensional parallel waveguide model. With finite width of the metal line, the field lines are confined under the metal line. Thus, the energy is mostly concentrated under the metal line, and less energy is dissipated to the other region. We can predict that with proper doping profiles in the silicon substrate, the electric field could be confined to a higher extend in the desired region, and thus less dispersion and energy loss would happen, and the wave might travel faster as well. This is part of the undergoing project in our on-chip interconnects analysis.

4.7 Summary

In Chapter 4, we used the quasi-analytical analysis method to review the three fundamental propagation modes in the MISM structure, and define them on the frequency-substrate doping map for the first time. Then, we used the ADI-FDTD method to extract the frequency dependent parameters of the MISM interconnect successfully, which is proven by the experimental results in the literature. With the help of the ADI-FDTD method, not only the frequency dependent parameters of the slow-wave mode and the quasi-TEM mode can be extracted efficiently, but also the characteristic parameters in the transition region and in the skin-depth mode region can be obtained in a reasonable amount of calculation. The field distribution at a transient time is analyzed in detail, the energy transformation and the power loss in the substrate is also investigated. The metal line width effect is discussed and the

possible optimization of low dissipation interconnects is proposed by some novel design of the substrate doping profile.

Chapter 5: Summary and Future Work

5.1 Summary

In this thesis, we reviewed physical and numerical models for the on-chip interconnect MISM structure. The FDTD algorithm is briefly introduced, numerical concerns, such as stability, numerical dispersion, boundary conditions are discussed as foundations of ADI-FDTD method.

ADI-FDTD method is a time domain numerical method, which has the advantages especially in electrically large problems. The algorithm is introduced in detail. Time-step, numerical dispersion, numerical stability and their physical meanings are discussed in detail.

Finally, we applied the ADI-FDTD method to the on-chip MISM interconnect problem. We are able to solve the field distribution in the thin metal layer, and show skin-effect mode, as well as slow wave mode, quasi-TEM mode over wide frequency and semiconductor doping density range efficiently. The field distribution at a transient time is analyzed in detail, the energy transformation and the power loss in the substrate is also investigated.

5.2 Future Work

5.2.1 ADI-FDTD Algorithm improvement

From the discussion in this thesis, we realized although the ADI-FDTD method has the great advantages of removing the Courant Stability condition, and thus greatly increases the computational efficiency; it has its potential accuracy

weakness. Also, applying different boundary conditions and excitations will profoundly impact the accuracy, the dispersion and the computation simplicity of the algorithm itself. Detailed discussions of the truncation errors, the dispersions referred to lossy, anisotropic materials are yet to be provided. All of these works are closely related to how well a physical problem could be simulated.

5.2.2 Complicated Integrated Physical Models

The real physical on-chip interconnects is far more complicated than a single MISM line, or some coupled MISM lines. The effect of the interaction mechanism between the electromagnetic field and the charged carriers in the semiconductor should also be taken into account in the analysis. [27] and [30] combine the semiconductor equations and Maxwell's equations together to perform the Metal-Insulator-Semiconductor Interconnects analysis on the device level. Research in [27] is performed with the equivalent circuit model. A full-wave analysis is still necessary to understand the detailed energy exchanges and field propagations. Also, on the real chip, there are signal lines, power lines, data lines, which make the accurate prediction of the coupling, crosstalk, power loss more difficult to obtain. The statistical model might be combined with the ADI-FDTD full wave solver as well to make reasonable system level analysis on these problems.

References

[1] A Deutsch, P. W. Coteus, G. V. Kopcsay, H. H. Smith, C. W. Surovic, B. L. Krauter, D. C. Edelstein, and P. J. Restle, "On-chip wiring design challenges for gigahertz operation," Proceedings of the IEEE. Vol,80, No.4, April, 2001.

[2] H. Guckel, P.A.Brennan, and I. Palocz, "A parallel-plate waveguide approach to microminiaturized, planar transmission lines for integrated circuits", IEEE Trans. Microwave Theory Tech, Vol. MTT-15, No. 8, pp.468-476, August 1967.

[3] H. Hasegawa, M. Rurukawa, and H. Yanai, "Properties of microstrip line on Si-SiO_2 system", IEEE Trans Microwave Theory Tech, Vol. MTT-19, No. 11, pp.869-881, August 1971.

[4] P.Kennis and L. Faucon, "Rigorous analysis of planar MIS transmission lines", Electron. Lett., Vol.17, No.13, pp.454-456, June 1981.

[5] M. Aubourg, J.P. Villotte, F. Godon, and Y.Garault, "Finite element analysis of lossy waveguides—application to microstrip lines on semiconductor substrate," IEEE Trans. Microwave Theory Tech., Vol. MTT-31, pp. 326-331, Apr. 1983

[6] R. Sorrentino, g. Leuzzi, and A. Silbermann, "Characteristics of metal insulator-semiconductor coplanar waveguides for monolithic microwave circuits," IEEE Trans. Microwave Theory Tech., vol. MTT-32, pp. 410-416, Apr. 1984

[7] T.-C, Mu, H. Ogawa, and T. Itoh, "Characteristics of multiconductor, asymmetric, slow-wave microstrip transmission lines," IEEE Trans Microwave Theory Tech., vol. MTT-34, pp. 1471-1477, Dec. 1986.

[8] T. Shibata and E. Sano, "Characterization of MIS structure coplanar transmission lines for investigation of signal propagation in integrated circuits," IEEE Trans. Microwave Theory Tech., vol. MTT-38, pp. 881-890, July 1990.

[9] F.L. Mesa, G. Cano, F. Median, R. Marques, and M. Horno, "On the quasi-TEM and full-wave approaches applied to coplanar multistrip on lossy dielectric layered media," IEEE Trans. Microwave Theory Tech., vol. MTT-40, pp. 524-531, Mar. 1992.

[10] W .R. Eisenstadt, Y. Eo, "S-parameter-based IC interconnect transmission line characterization," IEEE Trans Components, Hybrids, and Manufacturing Tech, Vol.15, No.4, pp.483-490, Aug, 1992.

[11] A. Weisshaar, H. Lan, A. Luoh, "Accurate closed-form expressions for the frequency-dependent line parameters of on-chip interconnects on lossy silicon substrate," IEEE Trans. Advanced Packaging, Vol.25, No.2, pp.288-296, May.2002.

[12] E. Groteluschen, L. S. Dutta, and S. Zaage, "Quasi-analytical analysis of the broadband properties of multiconductor transmission lines on semiconducting

substrates," IEEE Trans. Components, Packaging, Manufacturing Tech, part B. Vol. 17, No.3, pp. 376-382, Aug,1994.

[13] S. Dai, A.Z. Elsherbeni, and C. E. Smith, " The analysis and reduction of crosstalk on coupled microstrip lines using nonuniform FDTD formulation," International Microwave Symposium, San Francisco, CA, pp.307-310,1996

[14] J-T. Kuo, "Accurate quasi-TEM spectral domain analysis of single and multiple coupled microstrip lines of arbitrary metallization thickness," IEEE Trans. Microwave Theory Tech, Vol.43, No.8, pp.1881-1888, Aug, 1995.

[15] Y. Fukuoka, Y. Shih, and T. Itoh, "Analysis of slow-wave coplanar waveguide for monolithic integrated circuits," IEEE Trans. Microwave Theory Tech., vol. MTT-31, pp. 567-573, Jul 1983.

[16] J. P. K. Gilb, and C. A. Balanis, "MIS slow-wave structures over a wide range of parameters," IEEE Ttrans. Microwave Theory Tech, Vol. 40, No.12, pp.2148-2154, Dec,1992.

[17] I.M. Elfadel, A. Deutsch, H. H. Smith, B. J. Rubin, G. V. Kopcsay, "A multiconductor transmission line methodology for global on-chip interconnect modeling and analysis," IEEE Trans. Advanced Packaging, Vol.27, No.1, pp.71 – 78, Feb. 2004.

[18] P. Maffezzoni, and A. Brambilla, "A statistical approach to derive an electrical port model of capacitively coupled interconnects," IEEE Trans. Circuits and Systems, Vol.51, No.4, pp. 797-807, April,2004.

[19] http://www.wjrh.ece.uvic.ca/WJRH/tlm/

[20] T. Namiki, "A new FDTD algorithm based on alternating-direction implicit method," IEEE Trans. Microwave Theory Tech, Vol.47, No.10, pp.2003-2007, October 1999.

[21] G. Wang, "A Survey on Simulations of Metal-insulator-Semiconductor (MIS) Interconeects,"http://www.tcad.stanford.edu/~gaofeng/research/mis-review.htm

[22] J. D Meindl, R. Venkatesan, J. A. Davis, J. Joyner, A. Naeemi, P. Zarkesh-Ha, M. M. Bakir, T. Mule, P. A. Kohl, K. P. Martin, "Interconnecting device opportunities for gigascale integration (GSI)," International Electron Devices Meeting, 2001. IEDM Technical Digest., pp.23.1.1 - 23.1.4, Dec. 2001

[23] H. Hasegawa and S. Seki, "On-chip pulse transmission in very high speed LSI/VLSI," IEEE Microwave and Millimeter-Wave Monolithic Circuits Symp. Dig. (San Francisco), 1984, pp.29-33.

[24] K. Wu and R. Vahldieck, "Hybrid-mode analysis of homogeneously and inhomogeneously doped low-loss slow-wave coplanar transmission lines," IEEE Trans. Microwave Theory Tech., vol. MTT-39, pp. 1348-1360, Aug. 1991.

[25] S. Chen, R. Vahldieck, an dJ. Huang, "Rigorous analysis of mode propagation and field scattering in silicon-based coplanar MIS slow wave structures with

abrupt transitions to transmission lines on normal substrate," IEEE Trans. Microwave Theory Tech., vol. MTT-44, pp. 2487-2494, May 1996.

[26] M. V. K. Chari, S. J. Salon, "Numerical methods in electromagnetism," Academic Press, 2000.

[27] G. Wang, X. Qi, Z. Yu, R. W. Dutton, "Device level modeling of metal-insulator-semiconductor interconnects," IEEE Trans. on Electron Device, Vol.48, No.8, Aug, 2001, pp1672-1682.

[28] Y. R. Kwon, V. M. Hietala, and K. S. Champlin, "Quasi-TEM analysis of slow-wave mode propagation on coplanar microstructure MIS transmission lines," IEEE Trans. Microwave Theory Tech., vol. MTT-35, pp. 545-551, June 1987.

[29] K.W. Goossen and R. B. Hammond, "Modeling of picosecond pulse propagation in microstrip interconnections on integrated circuits," IEEE Trans. Microwave Theory Tech., vol. MTT-37, pp. 469-478, March 1989.

[30] K. Han and T.T.Y. Wong, "Space-charge wave considerations in MIS waveguide analysis," IEEE Trans. Microwave Theory Tech., vol. MTT-39, pp.1126-1132, July 1991.

[31] P.B. Johns, "The solution of inhomogeneous waveguide problems using a transmission-line matrix," IEEE Trans. Microwave Theory and Tech, Vol. 22, No. 3, pp.209-215, Mar 1974.

[32] K. S. Yee, "Numerical solution of initial boundary value problems involving Maxwell's equations in isotropic media," IEEE Trans. Antennas Propagation, Vol.AP-14, No.3, pp. 302-307, May,1966.

[33] W.L. Stutzman and G.A. Thiele, "Antenna theory and design," Second Edition, John Wiley & Sons, Inc, 1998.

[34] A. Taflove, "Computational electrodynamics, the finite-difference time-domain method," First Edition, Artech House, Inc, 1995.

[35] G. Mur, "Absorbing boundary conditions for the finite-difference approximation of the time-domain electromagnetic-field equations", IEEE Trans. Electromagnetic Compatibility, Vol, EMC-23, No. 4, pp. 377-382, Nov. 1981.

[36] S. Xiao et al., "An improved 2D-FDTD algorithm for hybrid mode analysis of quasi-planar transmission lines," IEEE MTT s. Digest, pp. 421-424, 1993.

[37] E. Tentzeris, M. Krumpholz, L. P. B. Katehi, "Application of MRTD to printed transmission lines," IEEE International Microwave Symposium Digest, 1996., MTT-S Vol.2, pp.573 – 576, Jun, 1996.

[38] Q. H. Liu, "The pseudo spectral time-domain (PSTD) method: A new algorithm for solution of Maxwell's equations," IEEE Antennas and Propagation Society Int. Symp, 1997., 1997 Digest Vol. 1, pp.122 – 125, Jul. 1997.

[39] F. Zheng, Z. Chen, and J. Zhang, "Toward the development of a three-dimensional unconditionally stable Finite-Difference Time-Domain method," IEEE Trans. Microwave Theory Tech, Vol.48, No.9, pp. 1550-1558, Sep, 2000.

[40] C C.-P. Chen, T-W Lee, N. M, S. C. Hagness, "Generalized FDTD-ADI: An unconditionally stable full-wave Maxwell's equations solver for VLSI interconnect modeling," ICCAD 2000, 3D.3, p.156

[41] S. G. Garcia, T-W Lee, S.C. Hagness, "On the accuracy of the ADI-FDTD method," IEEE Antennas and Wireless Propagation Letters, Vol.1, pp.31-34, 2002.

[42] C.Yuan, Z. Chen, "On the modeling of conducting media with the unconditionally stable ADI-FDTD method," IEEE Trans Microwave Theory Tech, Vol.51, No. 8, pp. 1929 – 1938, Aug. 2003.

[43] G. Sun, and C. W. Trueman, "Analysis and numerical experiments on the numerical dispersion of two-dimensional ADI-FDTD," IEEE Antennas and Wireless Propagation Letters. Vol.2, pp.78-81, 2003

[44] G. Sun, C. W. Trueman, "Some fundamental characteristics of the one-dimensional alternate-direction-implicit finite-difference time-domain method," IEEE Trans. Microwave Theory Tech., Vol.52, No.1, pp.46-52, Jan, 2004.

[45] G. Sun and C.W. Trueman, "Unconditionally stable Crank-Nicolson scheme for solving the two-dimensinal Maxwell's equations," Inst. Elect. Eng. Electron. Lett., vol.39, pp. 595-597, Apr. 2003.

[46] G. D. Smith, "Numerical solution of partial differential equations: finite difference methods," 3rd ed. Oxford, U.K.: Clarendon Press, 1985.

[47] F. Zheng and Z. Chen, "Numerical dispersion analysis of the unconditionally stable 3-D ADI-FDTD method," IEEE trans. Microwave Theory Tech., Vol. 49, pp. 1006-1009, May, 2001.

[48] J. Lee, B. Fornberg, "Some unconditionally stable time stepping methods for the 3-D Maxwell's equations," Preprint submitted to CAM, Sep, 2003.

[49] M. Darms, R. Schuhmann, H. Spachmann, and T. weiland, "Dispersion and asymmetry effects of ADI-FDTD," IEEE Microwave Wireless Components letters, Vol. 12, No.12, pp.491-493, Dec,2002.

[50] A. P. Zhao, "Analysis of the numerical dispersion of the 2-D alternating-direction implicit FDTD method," IEEE Trans, Microwave Theory Tech., vol. 50, pp. 1156-1164, Apr,2002.

[51] A.P. Zhao, "Consistency of the numerical dispersion relation expressed in different forms for the ADI-FDTD method," Microwave opt. Technol. Lett., vol.40, pp.12-13, 2004

[52] T. Namiki and K. Ito, "Investigation of numerical errors of the two-dimensional ADI-FDTD method for Maxwell's equations solution," IEEE Trans. Microwave Theory Tech., vol. 48, pp. 1950-1956, Nov. 2000

[53] A.P. Zhao, and R. Makinen, "An accurate and logically correct way to verify the numerical dispersion relations of FDTD and ADI-FDTD methods," Microwave Opt. Technol. Lett, vol. 40, pp. 427-431, Mar. 2004.

[54] W.R.Thurber, R.L. Mattis, and Y. M. Liu, National Bureau of Standards Special Publication 400-64,42, May 1981.

[55] X. Shao, "Electromagnetic modeling with a new 3D alternating-direction-implicit (ADI) Maxwell equation solver," master thesis, Dept of Electrical and Computer Engineering, University of Maryland, 2004.

[56] R.S. Muller, T. I. Kamins, M. Chan, "Device electronics for integrated circuits," John Wiley and Sons, 2002